Foaming Behavior of Aqueous Solutions Containing Hexadecyltrimethylammonium Bromide and Silica Nanoparticles: Analysis of Stability and Interfacial Properties

A thesis submitted

in partial fulfillment of the requirements

for the degree of

Doctor of Philosophy

by

Badri Vishal

Department of Chemical Engineering

Indian Institute of Technology Guwahati

July 2018

CERTIFICATE

It is certified that the work contained in the thesis entitled "**Foaming Behavior of Aqueous Solutions Containing Hexadecyltrimethylammonium Bromide and Silica Nanoparticles: Analysis of Stability and Interfacial Properties**", by **Badri Vishal**, has been carried out under my guidance and supervision. The work documented in this thesis has not been submitted to any other university or institute for the award of any degree or diploma.

Date:

IIT Guwahati

Signature of Thesis Supervisor

Dr. Pallab Ghosh

Professor,
Department of Chemical Engineering
Indian Institute of Technology Guwahati
Guwahati –781039, Assam, India

Acknowledgement

I would like to acknowledge all the people who contributed in some way to the work described in this thesis and supported me to complete my Ph.D.

First and foremost I offer my sincerest gratitude to my PhD supervisor, **Dr. Pallab Ghosh**, for giving me opportunity to work in a very fascinating area of research. I am very grateful to Dr. Pallab Ghosh for his continuous guidance, important advices, immense support, encouragement and most importantly allowing me the freedom to work in my own way. It was really an honor to work under him.

I would like to thank my doctoral committee members, **Dr. Subrata K. Majumdar** and **Dr. Chandan Das**, Department of Chemical Engineering, and **Dr. Kannan Pakshirajan**, Department of Biosciences and Bioengineering, for their valuable suggestions and constructive criticism during the annual progress seminars, which helped me to make necessary improvements in various stages of my research work.

I also thank **Dr. Bishnupada Mandal**, Head, Department of Chemical Engineering, for his administrative support. Furthermore, I would like to thank other faculty and staff members of Department of Chemical Engineering for their valuable support during my research.

I am grateful to all the technical staffs of my department, Mr. **Dipak Kumar Barman, Dr. Lukumoni Borah, Mr. Jayanta Kumar Mout, Mr. Ariful Hoque, Mr. Ritumoni Kalita, and Mr. Pankaj Kumar** for helping me in operating the equipments in the Analytical Laboratory. My sincere thanks to the technical officer, **Mr. Harsaraj**

Biswanath for allowing me to perform experiments during the weekends. I also thank **Mr. Bolledu Ravi** and **Dr. Nayanmani Das** for helping me in handling ellipsometry and Langmuir–Blodgett trough. I must thank office staffs **Mr. Sailen Das**, **Mr. Deep Jyoti Sinha,** and **Mr. Bhagya Boro** for helping me in official work.

I am also grateful to Central Instrument Facility, IITG for providing me the necessary support for analyzing morphology of my sample using Atomic Force Microscope (AFM) and Transmission Electron Microscope (TEM). I am particularly thankful to **Dr. G. Krishnamoorthy** (Head of the Central Instruments Facility) and **Mr. Madhurjya Borah** (Technical superintendent) who helped me in operating AFM and TEM. I deeply acknowledge my research group members **Mr. Shailesh R. Varade**, **Mr. Awadh Kishor Kumar, Mr. Jinesh Machale, Mr. J. Abdisa**, **Mr. M. K. Fahad**, **Ms. Rima Biswas**, **Dr. Snigdha Khuntia**, **Mr. Shashank Srinet**, **Ms. Ankita Jain**, **Ms. Ananya Basak**, **Mr. Vinay Babu,** and **Mr. Nipu Kumar Das** for providing a co-operative research environment.

I cannot forget to thank my friends **Mr. Kishant Kumar, Jitendra Singh Rawat, Dr. Anand Bharti, Mr. Binay Deogam, Mr. Arun Kumar, Mr. Abhishek Kumar, Mr. Ranjeet Kumar Mishra, Mr Proloy Das, Mr. Kulbhusan Samal, Mr. Debashis Kundu, Dr. Himadri Sahu, Mr. Bikashbindu Das** and many more for making my stay at IIT Guwahati memorable.

Above all, I would like to thank my family members for their love and support throughout for everything.

BADRI VISHAL

Abstract

Aqueous foams are considered as two-phase fluids in which the gas bubbles are dispersed in the aqueous phase. The bubbles are separated by interconnecting thin liquid films. The liquid content is sufficiently high in wet foams, whereas the same is usually small in dry foams. Aqueous foams belong to an important class of engineering materials due to their numerous applications in industry and daily life such as floatation, firefighting, water treatment, paints and coatings, textile finishing, enhanced oil recovery, cleaning agents, personal care products, food products, and pharmaceuticals. Foams are difficult to characterize because they are thermodynamically unstable (or metastable) systems. In many contexts and applications, it is of fundamental importance to understand the foaming behavior of kinetically-stable foams.

Use of surfactant for the stabilization of foams is a traditional method that has been used for a long time. Particles also act as a stabilizing agent when they are attached to the surfaces of the foam films. However, it is difficult to adsorb particles onto the surfaces because of their hydrophilicity. This can be altered by modifying the surface of the particles using a surfactant. The surfactant molecules adsorb on the surface of particles and thereby change their surface properties. This enables the particles to attach at the air–water interface. Particles adsorbed at the interface not only act as a surface-active agent, but they offer a distinct advantage of creating a more stable foam than their surfactant-stabilized counterparts.

In the present work, we have studied the effect of hexadecyltrimethylammonium bromide (HTAB) on the foaming behavior of dispersions containing silica nanoparticles. It was found that foams were more

stable at low surfactant concentrations, although the foamability was low. This was due to the formation of a strong viscoelastic film of surfactant-laden particles at the air–water interface. Below the CMC, the surfactant-laden particles were adsorbed at the air–water interface, aided by the induced motion of the surfactant molecules adsorbed on the particles. However, above the CMC, the interface was completely occupied by the surfactant molecules and hence, the surfactant-laden particles were accommodated near the sub-phase or in the bulk phase.

Smaller silica nanoparticles (i.e. diameter less than 10 nm) adsorbed at the air–water interface whereas the larger particles remained in the sub-phase or in the bulk liquid phase. Since the silica nanoparticles were hydrophilic, a major portion of these particles was oriented towards the aqueous phase, and hence a lesser portion was present in the air. It was found that these nanoparticles strongly influenced the foaming behavior at the low HTAB concentrations (i.e. below the CMC). A Langmuir-type monolayer was formed. The presence of the nanoparticles at the air–water interface provided mechanical strength to the foam films and prevented their rupture. This hindered coalescence of the bubbles, which resulted in a stable foam.

Rheology is an important tool for characterizing the soft complex materials, such as foams. The multiphasic composition of foams gives rise to complex rheological behavior under deformation. It is important to understand this behavior in many applications. Foam shows nonlinear rheological behavior at high deformations, which can be investigated by the large amplitude oscillatory shear (LAOS) experiment. We have performed a systematic LAOS

study of foam stabilized by 0.1 mol m^{-3} HTAB and 0.5 wt.% silica nanoparticles. The foam exhibited intracycle strain-hardening and shear-thinning at high deformation. Shear-thickening behavior was observed at moderate deformations. The foam films have two air–water interfaces and hence the foaming behavior strongly depends on the properties of these interfaces. We have investigated the interfacial properties by using interfacial shear rheology, which was studied in the linear and nonlinear deformation ranges.

Although extensive research has been performed on foams in the past few decades, a number of fundamental issues related to foams stabilized by particles have remained poorly understood. Some of these issues are, the role of nanoparticles in stabilizing the foam films and the air–water interface, the interaction between surfactant-laden particles in the liquid phase and at the interface, and the role of the charge of the surfactant and the nanoparticles in foaming. This thesis has investigated these issues in detail. The aim of this thesis is to understand the behavior of aqueous foams and air–water interface stabilized by a mixture of HTAB (a cationic surfactant) and silica nanoparticles (negatively charged particles).

Contents

List of Figures

computed by taking logarithm of the data in Figure 5.10a. The experiment was performed by applying an oscillatory shear at $\omega = 1$ rad s^{-1}.

Chapter 1

Introduction

1.1 Surfactants

When air is introduced into water, it forms spherical bubbles and they rise to the surface due to the buoyancy force. The bubbles eventually burst at the surface of water or coalesce when with other bubbles. To obtain stable air bubbles, one or more surfactants are used. The word "surfactant" stands for surface-active agent. It is an amphiphilic molecule having two parts: one part is hydrophilic (also called *head-group*) and the other part is hydrophobic (also called *tail*). Based on the charge on their head-group, surfactants can be classified as cationic (positively charged), anionic (negatively charged), nonionic (no charge), and zwitterionic (both positive and negative charges). Figure 1.1 shows the schematic representation of a surfactant molecule. Examples of different types of commonly-used surfactants are given in Table 1.1.

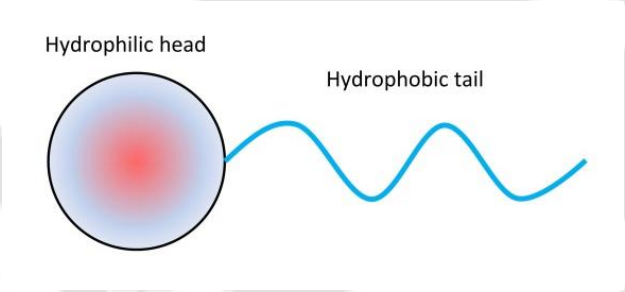

Figure 1.1 Schematic representation of a surfactant molecule.

A distinctive feature of the surfactant molecules is their ability to adsorb at the air–water interface. The hydrophilic head-group is oriented towards the aqueous phase (i.e. hydrophilic environment) and the hydrophobic tail group is oriented towards the air phase (i.e. hydrophobic environment). This forms a monolayer at the air–water interface, and reduces the surface free energy. When the surface is completely covered with the surfactant molecules, addition of more surfactant to the aqueous phase leads to the

Table 1.1 Examples of commonly-used surfactants of different types.

Surfactant	Type	Mol. wt.	Formula
Sodium dodecyl sulfate (SDS)	Anionic	288.38	$CH_3(CH_2)_{11}OSO_3Na$
Hexadecyltrimethylammonium bromide (HTAB)	Cationic	364.45	$CH_3(CH_2)_{15}N(Br)(CH_3)_3$
Triton X-100	Nonionic	647	$C_{14}H_{22}O(C_2H_4O)_n\ (n=9-10)$
Didodecyldimethylammonium bromide	Zwitterionic	462.64	$[CH_3(CH_2)_{11}]_2N(CH_3)_2(Br)$

formation of self-assembled structures known as *micelles*. The corresponding surfactant concentration is known as the *critical micelle concentration* (CMC). In the micelle, the hydrophobic tail groups minimize their contact with water and form a hydrophobic core. On the other hand, the hydrophilic head groups maximize their contact with water and form a surface layer of head-groups. Figure 1.2 shows the schematic representation of the surfactant molecules adsorbed at the air–water interface, and micelles formed in the bulk phase when the surfactant concentration is above the CMC. There is a dynamic equilibrium of the surfactant molecules between the micelles and the monolayer.[1,2] Reverse micelles can form when the surfactant molecules dissolve in oil and form aggregates inside the oil.[3] Below the CMC, the surfactant molecules continue to adsorb at the air–water interface, resulting in the formation of the monolayer. Upon increasing the surfactant concentration beyond the CMC, the surfactant molecules in the bulk aqueous phase form the micelles, and the number of micelles increases with increasing surfactant concentration. At a higher surfactant concentration, the shape of the micelles changes.

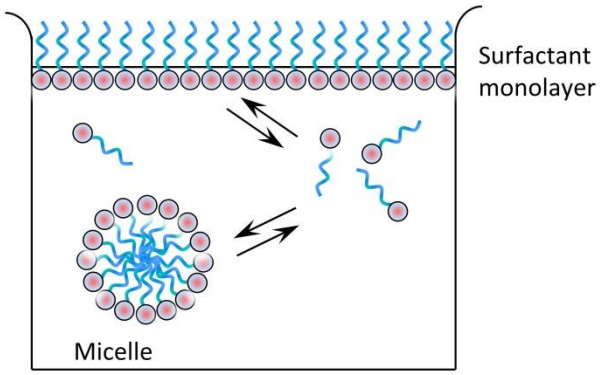

Figure 1.2 Schematic representation of the formation of monolayer at the air–water interface, and micelles formed in the bulk phase when surfactant concentration is above the CMC.

Often a transition from spherical to cylindrical micelles is observed. Some surfactants form worm like micelles and complex microstructures. The physical properties of the micellar solution change significantly as these changes take place.[4]

1.2 Formation of foams and their structure

Foams are usually formed by condensation, dispersion, or agitation processes. In the condensation process, the liquid is first saturated with the gas under high pressure, and thereafter the bubbles are released when the pressure is lowered. The foams in beer, champagne, and carbonated drink, which are saturated with carbon dioxide, are formed in this manner. In the dispersion process, the gas is injected into the liquid phase through a sparger. This process is widely used in industrial applications such as froth floatation and foam fractionation. In the mixing process, foam is generated by thorough mixing in a blender. The shape and size of the bubbles depend on the foam formation process.[5] For

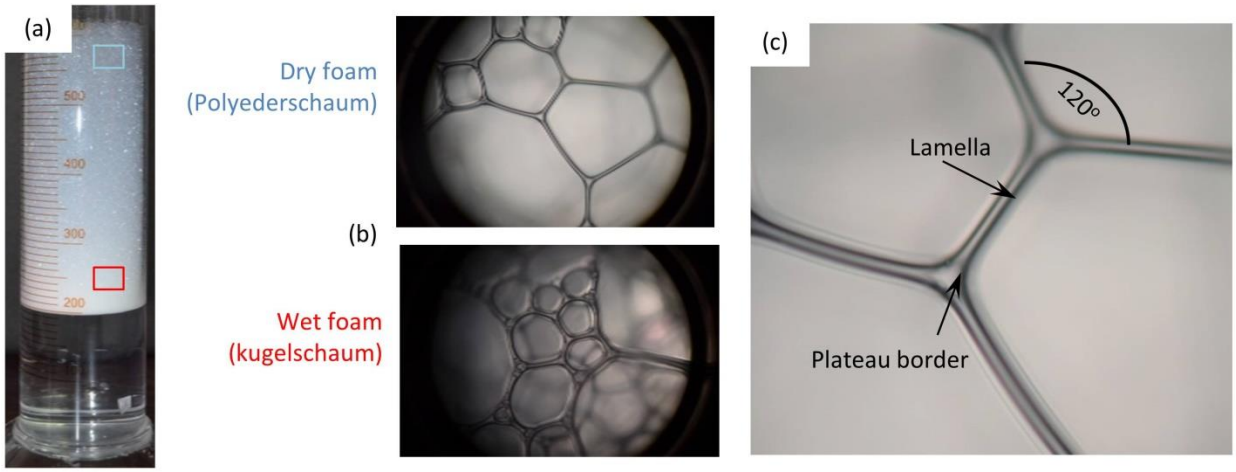

Figure 1.3 (a) Digital photograph of aqueous foam, (b) optical microscope images of foam structure stabilized by surfactant and particles. The polyhederal bubbles suggest a dry foam and the spherical bubbles suggest a wet foam. (c) The foam showing Plateau border and liquid lamella.

instance, when foam is generated by injecting air slowly into the liquid through an orifice, it is nearly monodisperse. The air-flow rate can change the geometry of the bubbles because it affects the liquid holdup in the foam.[6] Friedmann and Jensen[7] have found that the bubble size is inversely proportional to the injection velocity of air into the liquid phase.

Based on the shape of the bubbles, foam is divided into two classes, i.e. *kugelschaum* and *polyederschaum*. *Kugelschaums* have spherical bubbles, and their liquid content is high. Therefore, they are also called "wet" foams. On the other hand, *polyederschaums* have polyhedral bubbles, which are separated by flat thin liquid films. They have a less liquid content, and therefore, they are known as "dry" foams. In a foam column, the *kugelschaum* is usually found near the liquid surface and *polyederschaum* is

usually found near the top region of the column, as shown in Figure 1.3. The flat surfaces of polyhedral bubbles touch and form a thin liquid film, which is known as *lamella* [see Figure 1.3(c)]. Three (and only three) such lamellae meet at an angle of 120^o along an edge, known as the *Plateau border*, as shown in Figure 1.3(c). Four (and only four) of these Plateau borders always meet symmetrically at a point (known as *node*) at an angle of 109.47^o. These two conditions are known as *Plateau's rule*. This rule can be used to describe the structure of the foams. At equilibrium, foams have a minimal interfacial energy, which determines the dependence of their structure on liquid-content. When the liquid-content is higher than the close-packing fraction of the air phase in the foam, it results in a bubbly liquid. When both the fractions are same, bubbles are jammed and they form a wet foam. When the liquid content is lower than the close-packing fraction of the foam, a dry foam forms, which follows the Plateau's rules. The monodisperse dry foams crystalize into the body-centered cubic structure (i.e. Kelvin's structure), whereas the monodisperse wet foams crystalize into the face-centered cubic structure.[8]

Several authors[9-12] have correlated the structure of foam and foam film with their stability. There exists a pressure difference across a bubble surface which is a consequence of curvature and surface tension. The pressure inside a bubble (P_d) is always greater than that outside (P_l), which is given by the Young–Laplace equation given below.

$$\Delta P = P_d - P_l = \gamma\left(\frac{1}{R_1} + \frac{1}{R_2}\right) \tag{1.1}$$

where R_1 and R_2 are the principal radii of curvature, and γ is the surface tension. For a spherical bubble, $R_1 = R_2 = R$, and Equation 1.1 simplifies to

$$\Delta P = \frac{2\gamma}{R} \tag{1.2}$$

This equation relates the pressure difference across the bubble surface to the radius of the bubble. This pressure difference causes thinning of the foam film and thickening of the Plateau border. From Equation 1.2, we observe that the pressure difference across the bubble surface is inversely proportional to radius of the bubbles. In other words, the pressure inside a smaller bubble is higher than that in a larger bubble. The pressure difference between the two bubbles is given by

$$\Delta P = 2\gamma\left(\frac{1}{r} - \frac{1}{R}\right) \tag{1.3}$$

where r and R are the radii of the smaller and larger bubbles, respectively, when they touch each other.

1.3 Foamability and foam stability

Foams are thermodynamically unstable or metastable and they eventually disappear or break at some time after generation.[13,14] Therefore, researchers and manufacturers are interested on their kinetic stability. Surfactant is the most commonly used stabilizing agent for foams. Several researchers[11,15-17] have studied the mechanism of foaming and their stability in aqueous surfactant solutions. The use of particles as a foaming (and stabilizing) agent has been known for many years.[18] Particles at the bubble surface provide a strong viscoelastic film and reduce the film drainage.[19] Additionally, they create a steric barrier, which slows down film rupture.[20] When a mixture of surfactant

and particles is used, a synergistic effect can be observed, and consequently foams can be stable for a significantly longer period.[21-23] The stability of foams in the presence of particles depends on the hydrophilicity[24], size[25,26], shape[27-30], and concentration[31,32] of the particles.

The stability of foams is predominantly affected by three phenomena, i.e. drainage, coarsening (or Ostwald ripening), and coalescence. In foams, drainage and coarsening are the major causes responsible for their instability. Study of these phenomena is crucial to understand foam stability. When the liquid fraction in the foam is less than 0.05, the foams are polyhedral. The liquid in the foams is distributed in the films and Plateau borders. At the Plateau borders, the gas–liquid interface is quite curved. This generates a low pressure region in the Plateau area (as predicted by the Young–Laplace equation, i.e. Equation 1.1). Since the films are flat, a higher pressure exists there. This pressure difference forces the liquid to flow towards the Plateau borders, causing thinning of the films and thickening of the Plateau borders. A schematic diagram of flow through foam channels is shown in Figure 1.4. According to the Plateau's rule of foam structure, the Plateau borders form a network, through which the liquid flows due to gravity. In a column of foam, the bubble size increases with height. The foam towards the bottom of the column has a lower bubble size and it is wet [see Figure 1.3 (a)]. However, the foam in the upper part of the column has a larger bubble size and it is dry. Therefore, due to the difference in the bubble size, a capillary flow is induced. The result of the gravity and capillary effects gives rise to the net flow of liquid through the Plateau borders during the drainage.

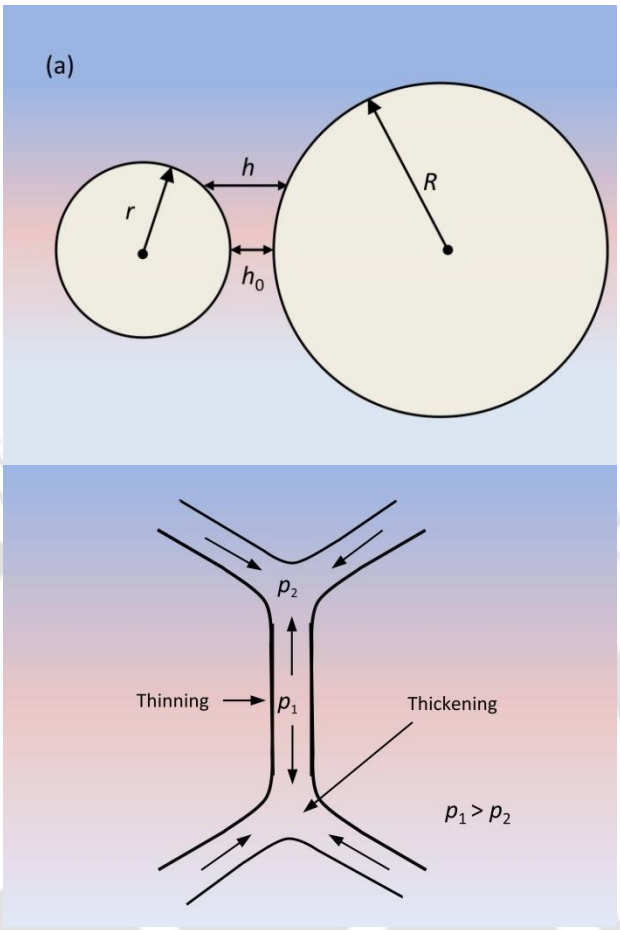

Figure 1.4 (a) A schematic representation of two approaching bubbles of radii *r* and *R*. (b) A schematic illustration of pressure difference across the curve surfaces in foam lamellae and flow of liquid towards the Plateau borders.

Several researchers[33-38] have studied drainage of liquid in foams. They have mainly focused on the velocity of liquid through the network of Plateau borders and determined the drainage time. However, very few researchers have studied the drainage in the presence of particles, although it has been known since a long time that particles play an important role in stabilizing foams. Recently, Narsimhan[39] has studied the

drainage of aqueous foam films containing particles. Kaptay[40] has studied foam films containing a single and a double layer of particles. They have derived expressions for maximum capillary pressure that is required to rupture the thin liquid film. Their derivation is based on the shape of the meniscus between two neighboring particles. The drainage in films containing multiple layers of the particles has been studied by Nikolov and Wasan.[41]

Despite the progress in the drainage theory of surfactant-stabilized aqueous foams, the drainage process is poorly understood when particles are present. The effects of unattached particles remaining in the liquid phase have been studied by some researchers.[42-44] The drainage theories have set benchmarks for investigating foam drainage in the presence of particles. To characterize foam drainage in the presence of particles, a *confinement parameter* (ϕ_c) is often used. It is defined as the ratio of the particle's mean diameter and the maximum diameter of the circle inscribed in the Plateau border cross-section. When $\phi_c > 1$, particles are trapped at the node, and they are freely transported if $\phi_c < 1$. The other parameter that is used to describe foam drainage in the presence of particles is the *volume fraction of particles* (ϕ_p) in the liquid phase. Particles reduce the drainage rate for high ϕ_p.

In a polydisperse foam, larger bubbles are often surrounded by smaller bubbles. Due to the pressure difference (Equation 1.3), the gas inside the smaller bubbles diffuse to the larger bubble, and consequently, the smaller bubbles disappear, and the average size of the bubbles increases. This phenomenon is called *coarsening*. Coarsening of

foams has been studied in detail elsewhere.[33,45-48] Modeling of coarsening of foam is easier in 2D than 3D. Therefore, coarsening is often modeled in 2D, and then extended to the 3D foams. von Neumann[49] has demonstrated that the evolution of 2D foam with time depends only on its topology (i.e. number of its edges), but not on its shape and size. The growth-rate of a foam bubble is given by

$$\frac{dA}{dt} = k\left(n_e - \langle n_e \rangle\right) \tag{1.4}$$

where A is surface area of a bubble with n_e sides in 2D and k is a diffusion constant. $\langle n_e \rangle$ represents the average number of edges. For a 2D foam, three bubble walls usually meet at each vertex. Therefore, $\langle n_e \rangle = 6$ (i.e. Plateau's rule). Thus, the above equation becomes

$$\frac{dA}{dt} = k\left(n_e - 6\right) \tag{1.5}$$

For hexagonal bubbles, $n_e = 6$ and A is constant. When $n_e < 6$, the bubbles have higher pressure, they start shrinking with time and eventually vanish. When $n_e > 6$, the bubbles expand and become more coarse. Glazier et al.[50], Sire,[51] and Stavans et al.[52] have studied the coarsening for the 2D foams.

In a 3D foam, the liquid films are polyhedral. To extend the 2D model of coarsening by van Neumann's law to the 3D foam, theoretical works and simulations have been performed. These works are based on the conservation of the average energy, which is proportional to the size of the bubbles. The bubble topology is described by the number of bubble faces (F), which is analogous to n_e in the 2D foam (i.e. Equation 1.4).

The growth-rate is expressed by the volume of a bubble (V) with F faces, which is the replacement of A. Time evolution of the 3D foam during coarsening is given by[53]

$$\frac{dV}{dt} = k\left(F - \langle F \rangle\right) \tag{1.6}$$

where $\langle F \rangle$ is the average number of faces in a bubble. This equation shows that the volume of a bubble depends linearly with time. However, works based on the Potts model[54] have shown that volume of a bubble varies with $t^{3/2}$, and the value of $\langle F \rangle$ was found to be 15.8. Hence, the following normalized law of coarsening was developed by analogy with Equation 1.5 .[55,56]

$$\left(\frac{1}{V}\right)^{1/3}\frac{dV}{dt} = k\left[F - (15.8 \pm 0.1)\right] \tag{1.7}$$

For well-separated droplets, the process of coarsening is called *Ostwald ripening*. Ostwald ripening refers to mass transfer between bubbles of different curvature through their surrounding continuous medium. The concentration of the dispersed phase material at the surface of a bubble is inversely related to the radius of curvature. Hence, a small bubble has a high surface concentration in comparison with a large bubble. Therefore, a concentration gradient of the dispersed phase material in the continuous phase is set up. Mass transfer occurs along the concentration gradient from the small bubbles towards the larger bubbles. Therefore, small bubbles shrink and ultimately disappear while the larger bubbles grow at their expense, leading to phase separation.[57]

Coalescence of bubbles is also a major cause of destabilization of foams. This happens when the thin liquid film between two bubbles gets ruptured, and thereafter they merge into a single bubble. With time, the foam films become thinner, and they rupture

eventually. However, when the particles are attached at the air–water interfaces across the foam film, the coalescence of the bubbles can be prevented. Because coalescence is an important factor behind the stabilization of foams, several authors[58-60] have studied it extensively during the last few decades.

1.4 Applications of aqueous foams

Aqueous foams belong to an important class of engineering materials due to their numerous domestic and industrial applications such as cleaning, personal care, food processing, pharmaceutical preparation, floatation, firefighting, water treatment, textile finishing, enhanced oil recovery, and development of paints and coatings. The foams are often utilized as intermediates or end products.[61,62] Because of their ability to adsorb various gases, liquids, and fine solid particles, foams can be used as a firefighting agent.[63,64] In the petroleum industry, the enhanced oil recovery is done by injecting gases, primary steam, and carbon dioxide into the oil reservoirs. The major problem with this method is the low viscosity of the injected gases, which causes poor sweep efficiency. This can be improved by adding foams because they not only increase the viscosity of injected gases, but also can withstand high capillary pressure.[65,66] In our everyday life, we use various home and personal care products such as shampoos, soaps and detergents, deodorants, facial moisturizer creams and lotions, hair-styling mousse and conditioners, and shaving creams.[67] Foaming behavior in these products is important, and it is often a critical acceptance criterion by the consumers. A major part of the foodstuffs is in the form of foams. Examples of foam-based food products are bread, beer, ice-cream, and soft drinks. They are rich sources of protein, carbohydrate, and fat, which provide a good supply of energy to our body. High nutritional and sensorial

characteristics have made foam-based foods more interesting.[31,68,69] In the textile industry, water can be replaced by foam during the processing of fabric. Foams easily spread over large surface areas that permit a lower wet pickup. In addition, it saves a considerable amount of water and the energy required to vaporize water from the treated fabrics.[70,71] The study of foam or foam films is important from the research viewpoint because it provides a prototype for the fundamental understanding of other soft complex materials and various physicochemical processes.

1.5 Foam rheology

Rheology is the science of flow and deformation of a material when it is subjected to a stress. Study of rheological behavior is important because it provides an understanding about the relation between the structure and flow properties, which can be applied to design and/or formulate the materials for certain applications. In addition to this, the material functions are derived from the relation between stress and deformation (or deformation rate), known as constitutive equations. These functions are used to characterize the material behaviors in the real situation such as during the process operation or application. From a rheological point of view, foams can be considered as a fluid that exhibits yield-stress. This is because foam behaves like a solid under low shear stress, and it flows like a liquid under high shear stress.[72-74] In other words, it does not flow unless a threshold shear stress (or yield stress) is imposed. To characterize such a fluid, Bingham[75] or Herschel–Bulkley[76] models can be used, which are given by

Bingham model: $$\sigma = \sigma_0 + K\dot{\gamma} \quad (1.8)$$

Harschel–Bulkley model: $$\sigma = \sigma_0 + K\dot{\gamma}^n \quad (1.9)$$

where σ is the shear stress, σ_0 is the yield stress, $\dot{\gamma}$ represents shear rate, *K* is the *consistency index*, and *n* is the *flow behavior index*. The Herschel–Bulkley model reduces to the Bingham model when $n=1$. Most of the research on foam reveal that $n<1$, indicating that foams are shear-thinning fluids.[77,78]

There are two ways to understand the rheological properties of foams. In one approach, a detailed structure of foam networks is elucidated, where local stress deforms the foam network. Pressure and interfacial forces are responsible for the build-up of the local stress. The other approach is the popular continuum description, where suitable rheological parameters are obtained by correlating shear stress with the corresponding deformation (or deformation rate).

For the foams undergoing steady flow, the local stress can be obtained by performing a temporal average over the pressure and interfacial tension forces acting on a surface element at a fixed position, and this is given by[79,80]

$$\sigma = -\frac{1}{N\langle V\rangle}\sum_{k'=1}^{N}\left(P_{k'}V_{k'}\right)\delta_{ij} + \frac{\gamma}{N\langle V\rangle}\iint\left(\delta_{ij} - n_i n_j\right)dS \tag{1.10}$$

where P_k is the gas pressure and V_k is the volume of the k^{th} bubble, *N* is the total number of bubbles in the foam sample, $\langle V\rangle$ is their average volume, γ is the interfacial tension, and **n** is a unit vector normal to the interface. The integration is carried out over all the interfaces so that the entire volume can be covered.

Local strain is developed by the coarsening of the foam. In coarsening, the larger bubbles grow at the expense of smaller ones. Consequently, the edges of the bubbles change. When the edge length is reduced to zero, an unstable configuration is obtained

and neighbor-switching rearrangements occur. Such sudden topological changes are known as *T1 processes*.[10] During this process, the local configurations remain stable and Plateau's rules are followed. Khan and Armstrong,[81] and Kraynik and Hansen[82] have illustrated this phenomenon in detail by using a 2D model, as shown in Figure 1.5. The figure shows the deformation for unstrained 2D foam (Figure 1.5a) in which each film has the same length, which are labeled as 1, 2, and 3. As the foam cells deform, the three liquid films continue to meet at the angle of $2\pi/3$. If the strin is further increased, side "3" shrinks while the sides "1" and "2" elongate. Consequently, a critical strain is reached when side "3" reduces to zero length (Figure 1.5c). After the T1 processes, foam cells reform by neighbor-switching rearrangement (Figure 1.5d). The T1 processes not only occur by coarsening, but may also be induced by imposing shear strain. Several researchers[83,84] have reported that the T1 processes in 3D are more complex. This is because the bubble vanishes when the entire gas is transferred to its neighbors. Such topological changes are called *T2 processes*. To deal with the rheology of foams in 3D, a continuum approach is used, where foams are considered at the macroscopic level. On the macroscopic scale, the deformation can be expressed in term of strain. Consider that a sample is placed between two parallel plates having a fixed separation. The bottom plate is fixed and the top plate is set under motion. The strain can be defined as the displacement of the top plate over its thickness. In other words, strain can be determined by comparing the previous ($\mathbf{x}$) and present ($\mathbf{x}'$) positions of the sample elements. When the strain is very small or rheology is studied in the linear regime, strain can be expressed more conveniently by the infinitesimal strain tensor ($\mathbf{e}$). On the other hand, to study the rheological behavior in the non-linear regime, the strain tensor can be expressed by the

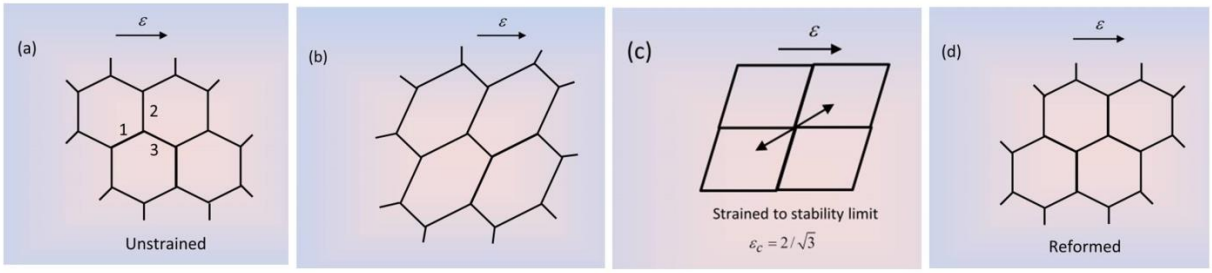

Figure 1.5 Graphical depiction of the deformation of two-dimensional hexagonal foam cells under imposed shear stress. The magnitude of strain is increased from the left to right [i.e. (a) to (d)].

deformation gradient tensor (**F**), the Finger strain tensor (**B**), or the Green (or Cauchy–Green) tensor (**C**).[85]

$$\mathbf{F}=\frac{\partial \mathbf{x}}{\partial \mathbf{x}'}; \qquad \mathbf{e}=\frac{1}{2}\left(\mathbf{F}+\mathbf{F}^{\mathbf{T}}\right)-\mathbf{I}; \qquad \mathbf{B}=\mathbf{F}\cdot\mathbf{F}^{\mathbf{T}}; \qquad \mathbf{C}=\mathbf{F}^{\mathbf{T}}\cdot\mathbf{F} \tag{1.11}$$

where **I** is the unit tensor. Strain (i.e. deformation) is usually used to characterize the solid-like behavior. However, to express the liquid-like behavior in steady state shear flow, deformation rate is the more suitable term, which is given by

$$2\mathbf{D}=\left(\nabla\mathbf{v}\right)^{\mathbf{T}}+\left(\nabla\mathbf{v}\right) \tag{1.12}$$

where $\left(\nabla\mathbf{v}\right)$ is the velocity gradient tensor.

The steady flow behavior of foam does not depict its evolution with time. However, it is a well known fact that the structure of foam changes with time via three mechanisms, i.e. film drainage, bubble coarsening, and bubble coalescence. The effect of time should be taken into account during the rheological study. For this purpose, transient flow of foam is to be induced by imposing oscillatory flow. Oscillatory shear is often

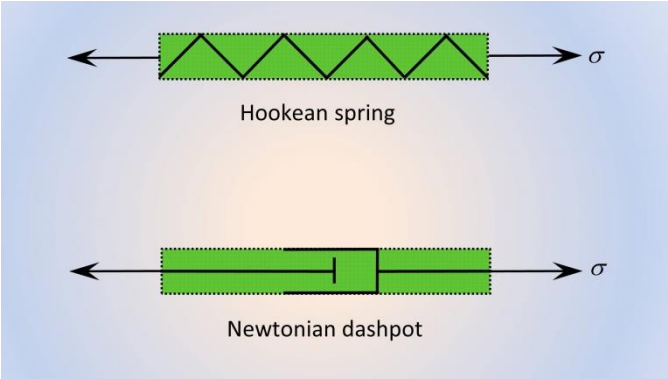

Figure 1.6 A schematic representation of two types of material response, i.e. a Hookean spring (for elastic solid) and a Newtonian dashpot (for viscous liquid).

used to characterize the viscoelastic behavior of a material.[86] From the energy point of view, a viscoelastic material has both viscous (i.e. liquid-like) as well as elastic (solid-like) properties. Most commonly, viscoelasticity is studied by imposing a sinusoidal strain or stress on the material, and the corresponding stress or strain is measured. A constitutive relation between the stress and strain is developed. This relation gives the material functions, which are used to describe their viscoelasticity. This approach measures the relative contributions of viscous and elastic response.

A convenient way of modeling viscoelasticity is by using the Hookean spring and the Newtonian dashpot. The Hookean spring is a representation of a perfect solid, which stores the energy when it is deformed. On the other hand when a perfect liquid is deformed, all the energy dissipates to maintain its flow behavior. This is represented by using a dashpot, as shown in Figure 1.6.

A perfect solid obeys Hooke's law and a perfect liquid obeys Newton's law, as given below

Hooke's law $$\sigma_1 = G\varepsilon_1 \tag{1.13}$$

Newton's law $$\sigma_2 = \eta\dot{\varepsilon}_2 \tag{1.14}$$

where G is the Young's modulus of elasticity and η is the viscosity. When these elements are combined in series, the resulting model is known as the *Maxwell model,*[87] as shown in Figure 1.7. In this model, when a shear stress (σ) is applied, the resulting deformation (ε) will be the summation of deformations caused by both the elements. The stress on both the elements will be the same and equal to the applied stress, given by

$$\varepsilon = \varepsilon_1 + \varepsilon_2 \tag{1.15}$$

$$\sigma = \sigma_1 = \sigma_2 \tag{1.16}$$

Using Eqs. (1.13) – (1.16), the Maxwell model is given by

$$\sigma + \lambda\frac{\partial\sigma}{\partial t} = \eta\dot{\varepsilon} \tag{1.17}$$

where $\lambda = \eta/G$ is the characteristic time of the material, known as the *relaxation time*. When a sinusoidal strain is imposed by applying a sinusoidal shear stress of frequency. ω, the elastic and viscous contributions can be observed by two material functions, i.e. storage modulus (G') and viscous modulus (G''), respectively, which are defined as follows:

$$G' = \frac{\eta\omega^2\lambda}{1+\omega^2\lambda^2}, \qquad G'' = \frac{\eta\omega}{1+\omega^2\lambda^2} \tag{1.18}$$

Similarly, when a Hookean spring and a Newtonian dashpot are connected in parallel, it results in the *Kelvin–Voight model,* where the total stress is the summation of the

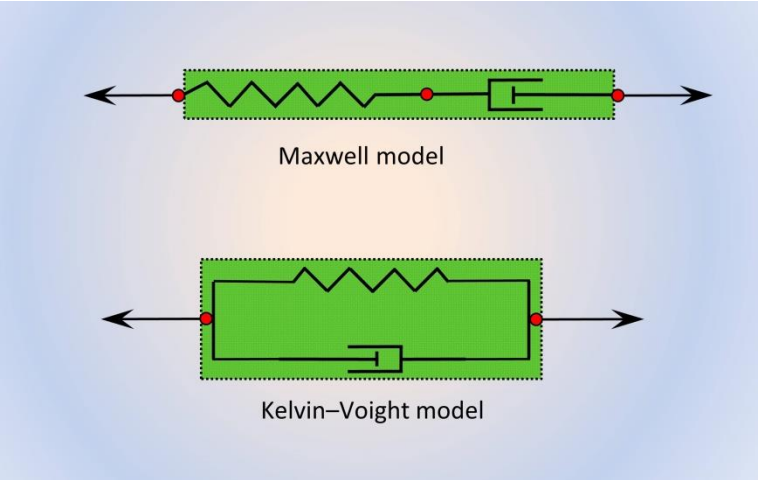

Figure 1.7 A mechanical representation of the Maxwell and the Kelvin–Voight models.

individual stresses. But, they have the same deformation. To understand the viscoelastic behavior, G' and G'' are measured in two ways, i.e. by amplitude sweep and frequency sweep experiments. In the amplitude sweep experiment, both the moduli are measured as a function of shear strain, where frequency is kept constant. On the other hand, in the frequency sweep experiment, they are measured as a function of frequency at a constant amplitude. The amplitude sweep experiment is used to find out the range of viscoelastic regime. At a low strain, the material shows linear viscoelastic behavior, and it shows nonlinear viscoelastic behavior at high strain. In the linear regime, no neighbor-switching rearrangement (i.e. T1 processes) occurs.[88]

Several researchers[89-91] have studied foam rheology of commercial products, such as the Gillette foam. The viscoelastic behaviors of foams are similar in many aspects to that of the other structured soft colloids such as concentrated emulsions[92-94] and soft pastes[95]. Although foam rheology has been studied by the standard methods of

rheometry,[85] a major drawback of this method is wall-slip during the measurement. Ideally, when foam flows between two smoothed parallel plates, its velocity near the plates is same as that of the plates. However, in many practical situations, the wall slip is very common in the multi-phase fluid flow.[96-100] When foam is allowed to flow by imposing a shear stress, the foam films near the bottom plate get penetrated. Thereafter, the liquid in the films creates a thin layer, which behaves like a lubricant. This is known as the "slipping layer", which produces a large velocity gradient. The lubricating effect causes the wall-slip. Consequently, the foam velocity mismatches with the plate velocity. Because of the wall-slip, the rheological measurements will vary when the size or gap of the geometry is changed. Let us consider a parallel plate geometry as shown in Figure 1.8, where the top plate is rotated with an angular velocity Ω, and the bottom plate is stationary. The deformation (ε) and deformation rate $(\dot{\varepsilon})$ for the gap, h_p, is given by

$$\varepsilon = \frac{\alpha s}{h_p}, \qquad \dot{\varepsilon} = \frac{\Omega s}{h_p} \tag{1.19}$$

where α is the angular displacement and s is the radial distance from the axis of rotation. These expressions show that ε or $\dot{\varepsilon}$ varies with the gap between the plates, and the shear stress is a function of ε and $\dot{\varepsilon}$, i.e. Hooke's and Newton's laws [Eqs. (1.13) and 1.14]. Consequently, the shear stress also varies with gap. Therefore, the rheological measurements show gap dependence.

For correct masurements of foam rheology, the wall-slip must be avoided. To prevent the wall-slip, several authors have recommended to use roughened surfaces.[101,102] The surfaces can be roughened by using a sandpaper or by sand blasting.

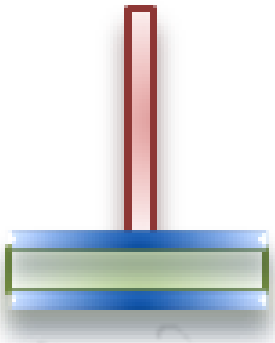

Figure 1.8 A schematic depiction of a parallel plate geometry.

Additionally, to avoid the wall-slip, the material between the parallel plates can be squeezed slightly by applying a normal force.[103] Yoshimura and Prud'homme[104] measured the rheological properties at different gaps and then took their average, which gave the true results. A detailed review on wall-slip is given by Cloitre and Bonnecaze.[105]

Due to the ease of varying the gap between the parallel plate geometry, it is widely used in the rheometry of multiphase systems, such as foams and emulsions. However, it shows a heterogeneous deformation because ε and $\dot{\varepsilon}$ vary linearly with radial distance, as can be observed from Equation 1.19. The heterogeneous deformation can also affect the flow behavior and deviation from true results can occur. Therefore, to avoid the heterogeneity in a steady shear flow, the stress needs to be corrected at the rim of the plate by using the Rabinowitsch[106] method, given by

$$\sigma_R = \frac{2M}{\pi R_p^{\,3}}\left(\frac{3}{4}+\frac{1}{4}\frac{d\ln M}{d\ln\left(\dot{\varepsilon}R_p\right)}\right) \tag{1.20}$$

where M is the torque and R_p is the radius of the parallel plates. For ideal materials, $d\ln M/d\ln\left(\dot{\varepsilon}R_p\right)=1$, and Equation 1.20 reduces to

$$\sigma_R = \frac{2M}{\pi {R_p}^3} \tag{1.21}$$

This equation is used in rheometry, which should be corrected according to Equation 1.20 by determining $d\ln M/d\ln\left(\dot{\varepsilon}R_p\right)$. For transient flow, Soskey and Winter[107] proposed a similar correction for shear stress to that given in Equation 1.20. For oscillatory flow, this correction is made on the basis of a suitable model such as the Giesekus[108] constitutive equation.[109-111]. Carvalho et al.[112] have proposed an alternative approach to calculate an approximate values for material functions by using a single-point correction technique. Yoshimura and Prud'homme[104] developed a method of obtaining true rheometry values by calculating the slip velocity at different gaps. Various researchers[113,114] have developed different approaches to deal with the true shear stress in parallel plate geometry when the deformation is large.

1.6 Two dimensional systems

1.6.1 Forces between surfaces

As per the IUPAC definition, colloid is a material which has at least one length scale between 1 nm and 1 μm. Foams are one of the most common colloid systems. As the size of these systems is reduced, the surface area to volume ratio increases. In the colloidal domain, the size is so small that this ratio becomes significantly large, and a high

percentage of molecules lie at the surface. Therefore, the surface forces significantly determine the stability and properties of foams.

In the initial stages after the formation of foam, the gravitational and capillary forces are responsible for the drainage of the films, which cause them to thin. Based on the studies on the thin liquid films, it has been found that when a film reaches a thickness of ~20 nm, apart from the gravity and capillary forces, surface forces begin to play a significant role. Surface forces have a molecular origin, and they are expressed in terms of the *disjoining pressure*.[115] In an equilibrium film, the disjoining pressure is balanced by the capillary pressure given by Equation 1.1.

1.6.1.1 Derjaguin approximation

To understand the interaction between two bubbles separated by a thin liquid film, the Derjaguin approximation[116] is usually used. It states that the energy of interaction, *E*, between two bodies across a film of uneven thickness is related to the interaction energy due to surface forces, $f(h)$, per unit area of a plane-parallel film. For two spheres of radii *r* and *R* (see Figure 1.4a), the relation between *E* and $f(h)$ is give by

$$E(h_0) = \left(\frac{2\pi rR}{r+R}\right)\int_{h_i}^{\infty} f(h)\,dh \tag{1.22}$$

The Derjaguin approximation is valid if the separation between the two surfaces is much smaller than the radii of curvature of the surfaces. Thus, the surface force between two surfaces separated at a distance h_0 across the thin liquid film can be related to the disjoining pressure as[117]

$$f(h_0) = \int_{h_0}^{\infty} \Pi(h)\,dh \tag{1.23}$$

1.6.1.2 van der Waals forces

All atoms in a liquid or gas attract each other due to the van der Waals forces. The electron clouds in these atoms fluctuate, and they create a dipole instantaneously. The dipole radiates an electromagnetic field that attracts other atoms around it. The atoms of a colloid polarize the atoms of another colloid in such a way that they attract each other. In fact, the van der Waals forces represent an average dipole–dipole interaction, which is a superposition of three terms: orientation interaction, induction interaction, and dispersion interaction. Orientation interaction is also called the *Keesom force*, which is the interaction between two permanent dipoles. Induction interaction is also known as the *Debye force*, which is the interaction between a permanent dipole and a induced dipole. The dispersion interaction is known as the *London dispersion force*, which is the interaction between two induced dipoles. The London dispersion force is the most import van der Waals force in most colloidal systems.

For two plane-parallel surfaces separated by a distance *h*, the disjoing pressure due to van der Waals force (Π_v) can be expressed as[118]

$$\Pi_v = -\frac{A_H}{6\pi h^3} \tag{1.24}$$

where A_H is known as *Hamaker constant*. The Hamaker constant is calculated for the surfaces whose gap must be larger than the molecular dimensions. The Hamaker theory[118] is a traditional approach to determine the Hamaker constant by considering the

interaction as pairwise additive. If the interaction between two surfaces, 1 and 2, is being considered, then the Hamaker constant is given by

$$A_H = \pi^2 n_1 n_2 A_L^{1,2} \tag{1.25}$$

where n_1 and n_2 are the number of molecules per unit volumes of the two bodies 1 and 2, respectively, and A_L is their London dispersion force constant. Because of the pairwise additive method, this approach is suitable if only the London dispersion force is present. The Keesom and Debye interactions are neglected since the range of their action is very small.[119]

The modern apparoach of computing the Hamaker constant is by using the Lifshitz theory.[120] This approach is based on the quantum field theory, where pairwise additivity is completely avoided. This theory is particularly suitable in calculating the Hamaker constant for two surfaces made of materials 1 and 2, interacting across a thin liquid film made of material 3. As per this theory, the Hamaker constant can be calculated from the following equation.[121]

$$A_H = \frac{3kT}{4}\left(\frac{\nu_1 - \nu_3}{\nu_1 + \nu_3}\right)\left(\frac{\nu_2 - \nu_3}{\nu_2 + \nu_3}\right) + \left(\frac{3h\nu_e}{8\sqrt{2}}\right)\left[\frac{\left(\mu_1^2 - \mu_3^2\right)\left(\mu_2^2 - \mu_3^2\right)}{\left\{\left(\mu_1^2 + \mu_3^2\right)\left(\mu_2^2 + \mu_3^2\right)\right\}^{1/2}\left\{\left(\mu_1^2 + \mu_3^2\right)^{1/2} + \left(\mu_2^2 + \mu_3^2\right)^{1/2}\right\}}\right] \tag{1.26}$$

where d_i (i = 1, 2, 3) are the dielectric constants, μ_i (i = 1, 2, 3) are the refractive indices, ν_e is the main electronic adsorption frequency in the ultraviolet region, T is the absolute temperature, and k and h are Boltzmann's and Planck's constants, respectively. The contribution of the Debye and Keesom interactions has been included in the first term of Equation 1.26. The second term represents the London dispersion interaction.

Therefore, for a thin liquid film, the Hamaker constant can be determined from the refractive index, dielectric constant, and adsorption frequencies of the materials.

1.6.1.3 Electrostatic double layer force

The air–water interfaces bear a fixed charge when dispersed in a polar liquid like water. Sometimes, ionic surface active agents provide surface charges. To maintain the electroneutrality of the interfaces, the same amount of oppositely charged counterions develops surrounding the interface. The counterions are organized in the two adjacent layers surrounding the interface (or particle) as shown in Figure 1.9. The first layer (close to the interface) consists of ions adsorbed onto the interface due to the Coulom attraction,

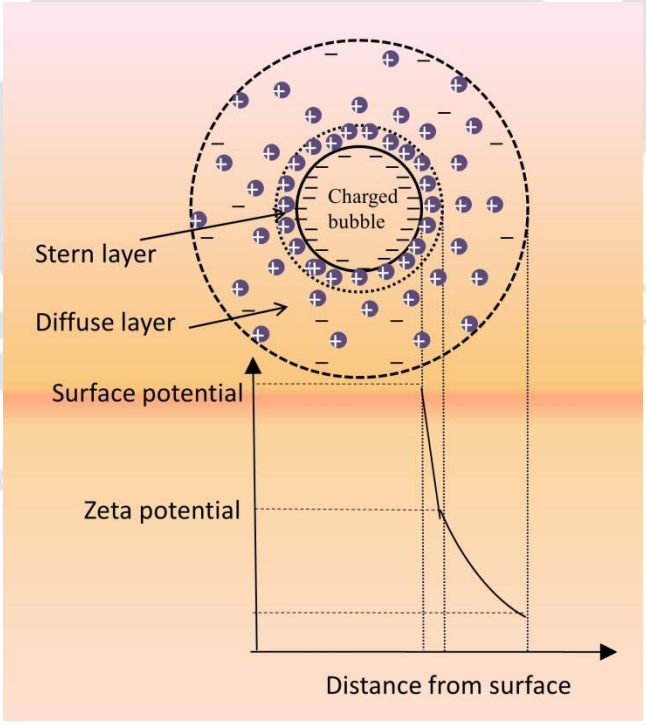

Figure 1.9 A schematic diagram of electrostatic double layer and variation of potential from the surface with distance.

which is known as *Stern layer*. In this layer, the counterions remain stationary and move with the interface. The second layer (beyond the Stern layer) of the counterions undergo thermal fluctuation, which is termed as *diffuse layer*. the arrangement of counterions in these two layers constitutes the electrostatic double layer. Unlike the Stern layer, the counterions are loosely associated in the diffuse layer. Hence, the charge density of the counterions close to the interface is relatively high, and it decreases with the distance from the interface. The electrostatic double layer was initially explained by Helmholtz with a simple capacitor model.[121] In this model, the counterions move as close as possible to the and form a sheet of counterions. Helmholtz's model predicts a linear potential drop across the double layer region resulting in a constant electrostatic field (i.e. the derivative of potential with distance). This model did not accurately represent a real system. Gouy and Chapman incorporated the thermal fluctuations in the Hemholtz's model. They derived an equation for the potential of the diffuse layer. However, this was not suitable at high potential or high ion concentration. Stern combined the ideas of Helmholtz, and Gouy and Chapman, and developed a double layer model including a fixed charge plane near the surface and a diffusion layer adjacent to the plane. The Helmholtz and the Gouy–Chapman theories are the two extreme cases of the Stern's model. In a system with low electrolyte concentration, the thickness of the diffuse layer is relatively large. Therefore, the influence of the Helmholtz layer is not significant. However, at high surface potential or high electrolyte concentration, the ions are more tightly compressed in the Stern layer. The Stern's model predicts the general features of ion distribution in real systems. The interaction between two charged bodies approaching each other is described by the Coulomb's law. This interaction becomes complicated

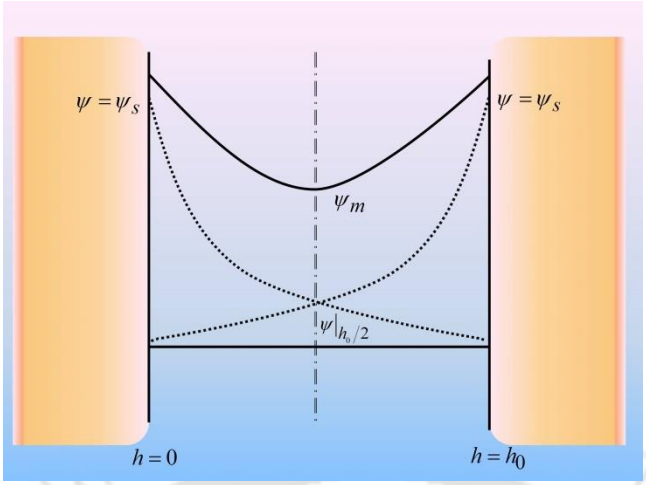

Figure 1.10 The potential profiles during the overlap of diffuse double layers of two charged flat surfaces approaching each other.

when the intervening medium (i.e. water) contains ions. When two charged surfaces approach each other in an aqueous medium, the electrostatic double layers on their surfaces overlap. This creates a repulsive force between the approaching surfaces. The potential profile (ψ) developed for two approaching charged surfaces is shown in Figure 1.10. The potential profiles in the individual double layers are shown by the dotted curves. The solid curve representing the potential profile (when the double layers overlap) indicates that the potential reaches its minimum value (ψ_m) at $h = h_0/2$ where $d\psi/dh = 0$. The disjoining pressure between two flat surfaces due to electrostatic double layer can be described by the following equation.[122]

$$\Pi_e = 64 R_s T c^{\infty} \tanh^2\left(\frac{ze\psi_s}{4kT}\right)\exp\left(-\kappa h_0\right) \tag{1.27}$$

where z is the valence of the electrolyte in the solution. It is evident that Π_e depends on c^{∞} (i.e. the concentration of electrolyte in the bulk solution). Gregory[123] has shown that ψ_m can be obtained by the linear superposition approximation, given by

$$\psi_m = \psi_1 + \psi_2 = 2\psi\big|_{x=h_0/2} \tag{1.28}$$

When the Derjaguin approximation is applied to Equation 1.27, the electrostatic double layer interaction between two spheres of radius r_s can be determined by using the following equation.[57]

$$\Pi_e = 64\pi r_s RTc^{\infty}\kappa^{-1}\tanh^2\left(\frac{ze\psi_s}{4kT}\right)\exp\left(-\kappa h_0\right) \tag{1.29}$$

where κ^{-1} is called the Debye–Hückel characteristic length.

It is difficult to determine the surface potential (ψ_s) experimentally. The zeta potential (ζ) gives an idea of the surface potential that can be measured from the electrokinetic phenomena (e.g. electrophoresis, electroosmosis, streaming potential, and sedimentation potential). The zeta potential is defined as the electrical potential at the plane of shear that separates the stationary counterions in the Stern layer and the mobile counterions in the diffuse layer.[124,125] When a particle moves in an electric field, the liquid layer immediately adjacent to the particle moves with the same velocity as the surface, i.e. the relative velocity between the particle and the fluid is zero at the surface. For a spherical colloid particle moving with velocity u in an electric field U in a dilute dispersion, the electrophoretic mobility is given by the Debye–Hückel equation[126]

$$\frac{u}{U} = \frac{2\nu\nu_0\zeta}{3\eta}, \qquad \kappa r_s < 0.1 \tag{1.30}$$

where ν is the dielectric constant of the medium and ν_0 is the permittivity of free space. For large values of κr_s, the relationship between the electrophoretic mobility and ζ-potential is given by Helmholtz–Smoluchowski equation

$$\frac{u}{U} = \frac{\nu\nu_0\zeta}{\eta}, \qquad \kappa r_s > 100 \tag{1.31}$$

1.6.2 The DLVO and non-DLVO theories

In a foam, the disjoining pressure balances the pressure difference across the bubbles.[115,127] The net disjoining pressure (Π) between two surfaces is given by the disjoining pressures due to the van der Waals (Π_v) and the electrostatic double layer forces (Π_e).[115,127-129]

$$\Pi(h) = \Pi_v + \Pi_e \tag{1.32}$$

Equation 1.32 is based on the Derjaguin–Landau–Verwey–Overbeek (DLVO) theory.[122,130,131] It takes into account the attractive and repulsive interactions between the two interfaces as shown in Figure 1.11. However, when the two surfaces approach closer than a few nanometers, the classical DLVO theory is often insufficient.[132] The failure of this theory is due to the fact that other non-DLVO forces start operating between the surfaces, which prevent the film from upture due to the primary minimum of the DLVO

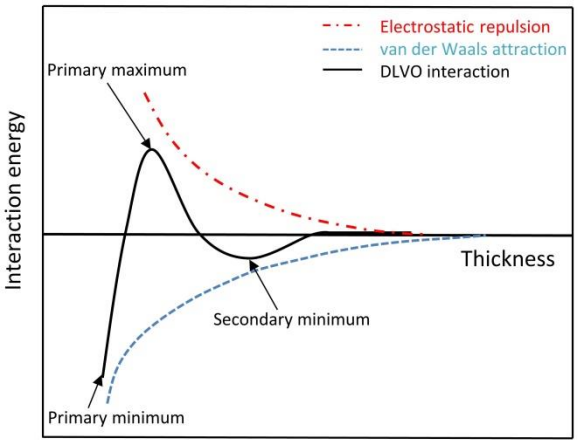

Figure 1.11 DLVO interaction enrgy profile.

interaction energy profile. Non-DLVO forces depend on the nature of surface and the type of surfactant present. The non-DLVO forces (e.g. hydration and structural forces) play significant roles when the surfactant head-groups are hydrated and the nanoparticles are present.[133,134] A third term incorporating the disjoining pressure due to the short-range repulsions (Π_s) may be included in Equation 1.32, given by

$$\Pi_s = C_1 \exp(-C_2 h) \tag{1.33}$$

where C_1 and C_2 are constants, which are chosen in such a way that the disjoining pressure curve has an almost infinite slope when the separation between the surfaces is less than 6 nm,[133] as shown in Figure 1.12.

In foams, the bubbles are separated by thin liquid films containing surfactant (and particles). When the particle concentration is sufficiently high, they have a strong tendency to form ordered layers in the film.[135] The overlap of these layers leads to a structural force, which is an additional stabilizing force in the thin liquid film.[136] During

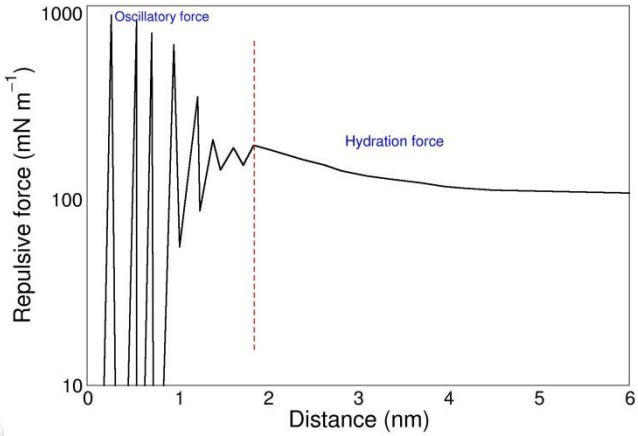

Figure 1.12 Short range non-DLVO forces.

the drainage, as the film thickness reduces to a few particle diameters, stepwise thinning of the film occurs, which is known as stratification.[137,138] Similar phenomena have been reported for micellar solutions.[135,139] The packing of particles influences the interaction between surfaces. The effect of particle packing on the stability of the thin liquid film is schematically shown in Figure 1.13. Structural force is important when colloidal particles are present in the thin liquid film. A positive disjoining pressure indicates that there is a repulsion between the surfaces, which occurs when the packing layers are ordered as shown by "b", "d", and "f" in Figure 1.13. A negative disjoining pressure represents an attraction between the surfaces that occurs when the packing layers of the particles in the liquid film are randomly ordered as shown by "c", "e", and "g" in Figure 1.13. When the film thickness just exceeds the particle diameter, there is a structural stabilization barrier (represented by "b"), whose height increases with the concentration of the particles. The presence of such a barrier has a significant implication on the stability of foams.[140] When particles are completely drained out of the liquid film, the film thickness reduces to

(a)

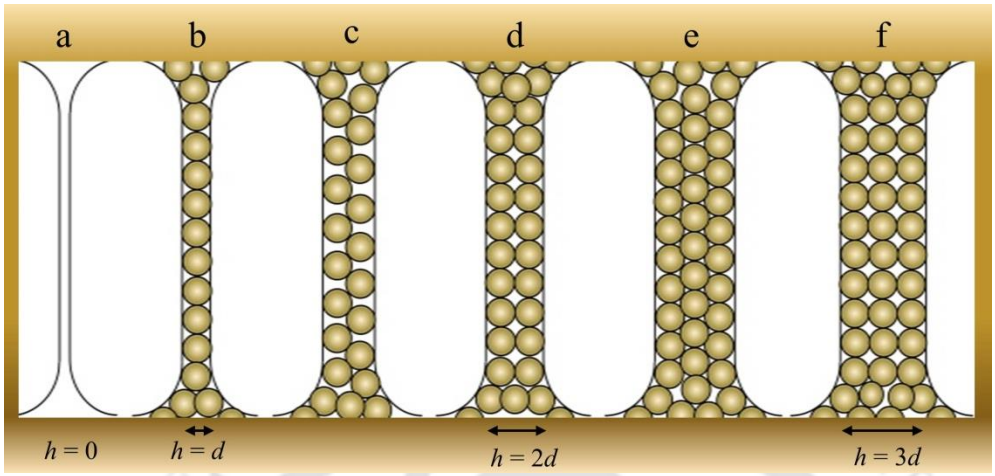

(b)

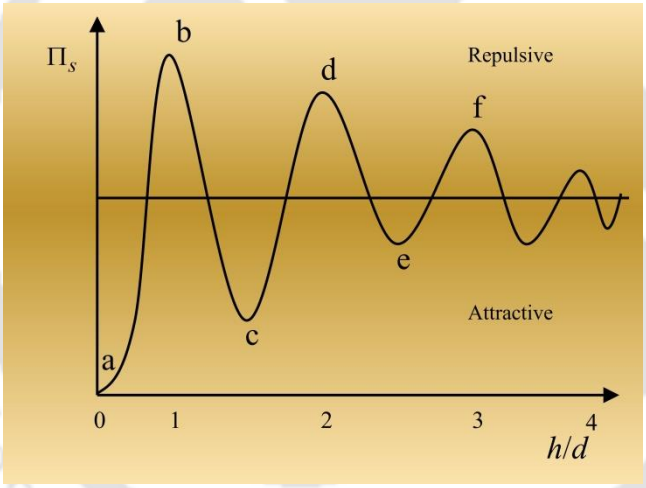

Figure 1.13 (a) Consecutive stages of thinning of a film containing spherical particles, and (b) the respective oscillatory structural disjoining pressure.

less than the particle diameter. In this case, the net attractive force is induced by the osmotic pressure difference between the liquid phase and the film (indicated by "a" in Figure 1.13).[141] Additionally, this is the range where the short range non-DLVO forces operate between the surfaces (Equation 1.33).

However, when particles are attached at the surfaces, i.e. complete drainage of particles does not occur, they are trapped between the surfaces as shown in Figure 1.14. In this case, the nanoparticles deplete the surfaces resulting in an attractive depletion force, which is also known as *Asakura–Oosawa depletion attraction*.[20] This force causes film rupture, which leads to bubble coalescence. According to another theory,[142] as the thickness continues to reduce below the particle diameter, the plane surfaces deform into meniscus. Consequently, the capillary pressure increases. The maximum capillary pressure $\left(P_c^{\max}\right)$ occurs at the onset of coalescence. It is given by[143,144]

$$P_c^{\max} = p\left(\frac{2\gamma}{R}\right)\cos\theta \tag{1.34}$$

where p is a packing parameter that depends on the concentration and orientation of the particles in the thin liquid film. This equation describes the case when the two menisci just touch each other (i.e. the film thickness reduces to zero).

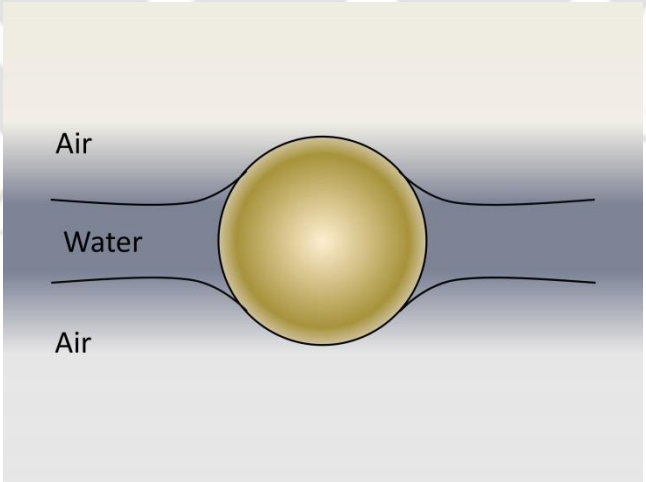

Figure 1.14 A schematic diagram of particle between the two surfaces in a thin liquid film.

1.6.3 Surfactant and particles at the interfaces

Like the surfactant molecules, particles can adsorb at the fluid–fluid interfaces. Therefore, they can act as a surface active agent. However, unlike the surfactant molecules, particles do not alter the surface tension when they adsorb at the interface.[145] Additionally, most of the particles are not amphiphilic except the Janus particles. These particles are surface active as well as amphiphilic, and the surface consists of two separate regions of different wettability.[146-148] Their potential as a stabilizing agent for foams was first realized by Ramsden[18] and Pickering[149] in the beginning of the last century.

In the case of surfactant-stabilized systems, the hydrophilic and hydrophobic tendencies of the surfactant molecules are quantified by the hydrophilic–lipophilic balance (HLB). The HLB value decides the dispersed and continuous phases.[150,151] For example, a surfactant of high HLB value is soluble in the aqueous phase, which becomes the continuous phase. Therefore, it is suitable for stabilizing foams, where water is the continuous phase. Similarly, in the case of particle-stabilized systems, the hydrophilic and hydrophobic tendencies are quantified by wettability, which can be represented by the contact angle (θ). This is a key parameter to express the adsorption mechanism of particles at the interface. It is measured through the aqueous phase. For hydrophilic particles, $\theta < 90^{o}$ and a larger fraction of the particle surface resides in the aqueous phase than in the air phase, as shown in Figure 1.15. Consequently, the interface bends towards the air or oil phase and forms the foams. For hydrophobic particles, θ is usually greater

than 90^o and the major portion of the particle surface resides towards the hydrophobic environment (i.e. air).

Surface properties of the particles are important for understanding their adsorption mechanism at the interfaces. Pure hydrophilic or hydrophobic particles do not adsorb by their own. They must be partially hydrophilic or hydrophobic, which enables them to adsorb at the interfaces. There are two ways of changing the surface properties of the particles, i.e. chemical modification and addition of a surfactant. Binks and Lumsdon[152,153] have studied the surface properties of hydrophilic silica particles in which the surface silanol (SiOH) groups were converted to more hydrophobic groups by reaction with silane reagents. Another way of changing the surface properties of particles is by adding a suitable surfactant.[23,154-157] For example, hydrophilic silica particles have

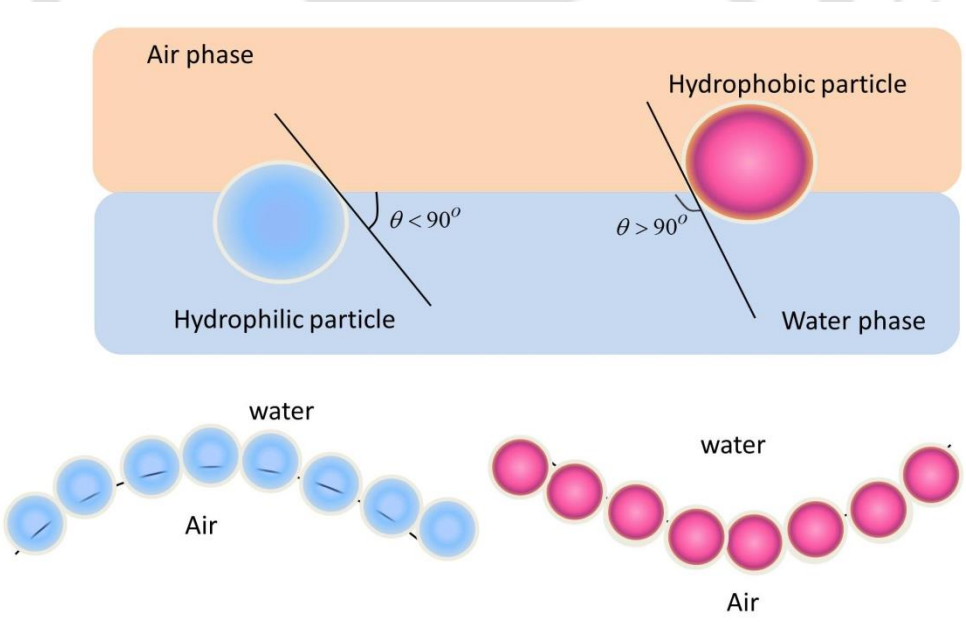

Figure 1.15 A schematic illustration of the position of a spherical particle at the air–water interface for $\theta < 90^o$ (top left) and $\theta > 90^o$ (top right). The corresponding (probable) positioning of the particles at a curved air–water interface.

negative charge at their surface. When a cationic surfactant (e.g. HTAB) is added to the solution, it adsorbs onto the surface of the particles due to electrostatic interaction between them. Consequently, the particles are surrounded by the hydrophobic tails of the surfactant molecules, which help to increase the hydrophobicity of the particles. Thereafter, particles of diameter between a few nanometers and a few micrometers can strongly attach to the interfaces.[158]

Unlike surfactant molecules, once the particles adsorb, they are strongly held at the interface. Particles deform the shape of the fluid–fluid interfaces, which gives rise to a capillary interaction between the particles and the interface. The capillary interaction determines the position of the particles at the interface. The stability of the particles at the air–water interface can be quantified by the minimum energy (ΔE) required to remove them from the interface, which is given by[159-161]

$$\Delta E = \pi r_s^2 \gamma (1 \pm \cos\theta)^2 \tag{1.35}$$

where ΔE depends on the radius of the particle (r_s), surface tension (γ), and contact angle (θ). In other words, the surface energy is reduced by ΔE when a particle adsorbs at the air–water interface. The removal of a hydrophilic particle from the air–water interface to the aqueous and air phases is signified by the negative and positive signs, respectively. ΔE is related not only to the contact angle, but also to the surface tension. The contact angle of a particle at the interface can be determined by *Young–Dupré equation*, given by

$$\gamma \cos\theta = \gamma_1 - \gamma_2 \tag{1.36}$$

where γ_1 and γ_2 are surface tension of phase 1 and 2, respectively. Particles are trapped at the interfaces by their lateral capillary energy, which is caused by the deformation of the interfaces. The capillary interaction increases with the extent of deformation.[162] Clint and Taylor[163] derived the following equation to determine the contact angle of particles at the interface from the surface pressure–area isotherm.

$$\cos\theta = \pm\left(\frac{2\sqrt{3}\Pi_c}{\pi\gamma} - 1\right)^{1/2} \tag{1.37}$$

Nevertheless, hydrophobic particles are sometimes used as antifoaming agents. When the size of the particles is larger than the film thickness, bridging of the film occurs, which penetrates the air–water interfaces. Due to the capillary force and large contact angle, the liquid then drains out from the foam films, which is known as *de-wetting*.[164]

1.6.4 Interfacial shear rheology

Colloidal systems, such as foams, have high specific surface area. Therefore, their dynamic behavior and stability can be affected significantly by varying the interfacial properties. Interfacial phenomena can be controlled by using surfactant, and sometimes by particles. Several researchers[165-168] have studied the rheology of the surfactant-covered air–water interfaces.[169-171] An approximate morphology of the interface can be determined by this method. Phenomena such as film drainage,[172] Ostwald-ripening,[173] and coalescence[174] can be understood from the interfacial rheological data.[58,175] Thus, it

can be an important tool for understanding the stability of foams.[176] It also illustrates the adsorption kinetics of surfactants and particles from the bulk phase.

There are two types film at the interface, i.e. a spread film and an adsorption film. When small surfactant molecules adsorb at the interface from the bulk phase, they form a Gibbs monolayer. On the other hand, macromolecules, such as long-chain polymers or proteins, high molecular weight fatty acids, and nanoparticles form Langmuir monolayers when their solutions are spread over the surface. To characterize a Langmuir monolayer, the Langmuir–Blodgett trough is often suitable, where the surface pressure is measured by compressing or/and expending the monolayer. Moreover, in many practical situations, the interface undergoes mechanical perturbations by changing its size and shape. The response of the interface to a change in its size at constant shape is studied by interfacial dilatational rheology, whereas interfacial shear rheology is the study of the response of the interface to a change in their shape while the area remains constant. In this thesis, the primarily focus is on the response of the interface against shear deformation. The interfacial shear rheology can be considered as a 2D analog of bulk rheology because it uses similar rheological concepts as that for the bulk materials.[58] However, this has a few notable restrictions. For instance, the shear deformation should not induce a radial flow at the interface. The bulk effect on the interfacial flow (i.e. the effect of coupling interfacial flow with the adjacent sub-phase liquid) should be avoided. This effect can be expressed by the Boussinesq number (Bo), which is the ratio of the surface to bulk viscous effects, defined by

$$\mathrm{Bo} = \frac{\eta_s}{(\eta_1 + \eta_2) L} \tag{1.38}$$

where η_s is the surface viscosity, η_1 and η_2 are the viscosities of the top and the bottom fluids, respectively, and L is a geometrical factor determined by the geometry used. Theoretically, if the value of Bo is larger than unity (i.e. for the Langmuir monolayer) the interface shows a dominating response against shear deformation, and the interfacial shear viscosity strongly influences the nature of bulk flow near or at the interface. Various geometries are available, which can be used for characterizing the interfacial shear rheology, such as double wall ring,[177] bicone disk,[178] and magnetic-needle.[179] To study interfacial shear rheology, the interface is allowed to flow by the rotational movement of the solid geometry within the interface. The interfacial stress response (σ_s) to the interface is directly proportional to the imposed interfacial strain (ε_s) or strain rate, given by

$$\sigma_s = G_s \varepsilon_s + \eta_s \frac{d\varepsilon_s}{dt} \tag{1.39}$$

where G_s and η_s are the shear modulus and viscosity of the interface, respectively. For an oscillatory shear flow in the linear viscoelastic regime, the stress response to the interface can be given by a complex interfacial shear modulus $\left(G_s^*\right)$. This is represented as shown below.

$$G_s^*(\omega) = G_s'(\omega) + iG_s''(\omega) \tag{1.40}$$

where ω is the frequency of oscillation, and G_S' and G_S'' are the real and imaginary parts of the complex modulus, which represent the elastic (i.e. storage modulus) and viscous (i.e. loss modulus) components of the interface, respectively.

Safouane et al.[180] have studied interfacial shear rheology at the air–water interfaces containing fumed silica particles. They have measured the oscillatory shear moduli (i.e. G_S' and G_S'') by varying particle hydrophilicity. For very highly hydrophilic particles, the oscillatory shear moduli were negligible, whereas for partially hydrophilic particles, G_S' was found to be greater than G_S''. They also observed a gel point where both the moduli were same. Cicuta et al.[181] have found that the interface formed by charged latex particles exhibited predominantly viscous behavior (i.e. $G_S' < G_S''$) when the surface coverage was high. They have also pointed out that the nature of the stress response to the interfacial deformation for hard and soft particles (i.e. protein molecule) was very similar, although they had very different interaction potentials. Most studies on interfacial shear rheology were at regimes where the shear stress and strain (or strain rate) were linearly dependent.[182-184]

The interfaces containing solid particles often show nonlinear viscoelastic behavior even at low deformations or deformation rates. In other words, the range of linear viscoelastic regime is very small because the microstructure at the interface changes easily by applying even a small shear stress. However, in many practical scenarios (e.g. during the formation and processing of foams), large and fast deformations are encountered. Therefore, to deal with real life phenomena pertaining to

the interfaces, the study of nonlinear rheological behavior of the interfaces is highly important.

There are several ways to study interfacial shear rheology at large deformations, e.g. by analyzing the storage (G_s') and loss moduli (G_s'') as a function of strain amplitude, which is commonly known as *amplitude sweep experiment*.[185] Recently, Lissajous–Bowditch curves have become very popular for characterizing nonlinear viscoelastic behavior, where the stress responses are plotted against the imposed strain (or strain rate).[186] These are termed as *elastic* (or *viscous*) *Lissajous–Bowditch curves*. This is a geometrical approach, in which the behavior of the air–water interface is characterized by analyzing the shape of the Lissajous–Bowditch curves. Because of the symmetry of the Lissajous–Bowditch curves, Cho et al.[187] suggested a method of decomposing the stress response into their elastic and viscous counterparts at large deformation, which was further improved by Yu et al.[188] Due to the involvement of higher harmonic terms, the detailed explanation of the Lissajous–Bowditch curves is not yet fully understood. Only a few works have been reported on the nonlinear viscoelastic behavior of the air–water interfaces using the Lissajous–Bowditch curves.[189-192] However, many works have been conducted on the nonlinear viscoelastic behavior of bulk materials.[193] Such information may be useful for analyzing the air–water interface. Despite the detailed study of the rheology of the interfaces containing surfactant-laden particles, it still poses some challenges, and the current knowledge is far from complete enough for practical applications.

1.7 Outline of the thesis

Each chapter of this thesis deals with a specific parameter, which is important in foam stability. The literature relevant to these aspects is reviewed separately in the corresponding chapter. The structure of the thesis is described below.

Chapter 1 **(Introduction)**: This chapter gives a general background, review of literature, and discussion on various topics, such as surfactants, nanoparticles, foam formation and the structure of foams, foamability and foam stability, application of aqueous foams, foam rheology, DLVO and non-DLVO theories, and interfacial rheology. The objectives of the research are presented.

Chapter 2 **(Materials and Experimental Methods)**: In this chapter, the details of materials used in this work are given. The methods of sample preparation are explained. The detailed information about the equipment used in this work is given. The procedure for conducting the experiments is described.

Chapter 3 **(Foaming in Aqueous Solutions of Hexadecyltrimethylammonium Bromide and Silica Nanoparticles: Measurement and Analysis of Rheological and Interfacial Properties)**: In this chapter, we have reported the properties of aqueous foams stabilized by a mixture of negatively-charged silica nanoparticles and the cationic surfactant, HTAB. The effects of HTAB on the stability of foams in the presence of the nanoparticles are reported. The rheological behavior of foams as well as that of the air–water interface is explained. The interaction between the nanoparticles and the surfactant molecules in the bulk phase is studied

by zeta potential and size measurement of the particles. The interaction at the interface is studied by means of interfacial shear rheology, surface pressure measurement, and atomic force microscopy. Finally, a suitable mechanism is proposed to elucidate the adsorption of surfactant-laden particles from the aqueous phase to the air–water interface.

Chapter 4 **(Effect of Silica Nanoparticles on the Stability of Aqueous Foams):** In this chapter, the effect of silica nanoparticles on the stability of foams in the presence of different concentrations of HTAB is discussed. The foams are characterized by measuring their foamability and stability. Rheological behavior of the foams is also reported. Furthermore, rheology of the air–water interface is studied in the linear and nonlinear deformation range. The nonlinear viscoelastic behavior is analyzed by using the Lissajous–Bowditch curves. The thickness and the microstructure of the monolayer at the air–water interface are measured by ellipsometry and BAM. The actual size of the silica nanoparticles at the air–water interface is measured by TEM. Based on these measurements, the interaction between the monolayers across the foam film containing HTAB and nanoparticles is explained.

Chapter 5 **(Nonlinear Viscoelastic Behavior of Aqueous Foam under Large Amplitude Oscillatory Shear Flow)**: In this chapter, the LAOS behavior of foam stabilized by a mixture of HTAB and silica nanoparticles is presented. The LAOS behavior of foam is described by analyzing the stress-response waveforms and the Lissajous–Bowditch curves obtained by shearing the foam at different amplitudes of oscillation. These curves are fitted by using Fourier transform rheology and Chebyshev

polynomials to understand the contribution of the higher harmonic terms in the LAOS flow. Finally, the intracycle LAOS behavior of foam is interpreted by a sequence of physical processes.

Chapter 6 **(Summary and Scope for Future Work)**: This chapter summarizes the important findings from this work and suggests ideas for future research.

Nomenclature

Symbols

A	surface area of bubble, m^2
A_H	Hamaker constant, J
A_L	London dispersion force constant, J m^6
B	finger strain tensor
Bo	Boussinesq number
c^{∞}	concentration of ions in the bulk solutions, mol m^{-3}
C	Cauchy–Green tensor
D	diffusion constant, m^2 s^{-1}
e	infinitesimal strain tensor
E	interaction free energy, Pa m
f	surface force, Pa m
F	number of faces of a bubble
F	deformation gradient tensor
$\langle F \rangle$	average number of faces

G	Young's modulus, Pa
G'	storage modulus, Pa
G''	loss modulus, Pa m
G_s	interfacial shear modulus, Pa m
G_s'	real part of interfacial complex modulus, Pa m
G_s''	imaginary part of interfacial complex modulus, Pa m
G_s^*	interfacial complex shear modulus, Pa m
h	separation between two bubble surfaces, m
h_p	gap between parallel plates, m
$\mathbf{I}$	unit tensor
k	Boltzmann's constant, m^2 kg s^{-2} K^{-1}
K	consistency index, Pa s
L	geometrical factor
M	torque, N m
n	flow behavior index
$\mathbf{n}$	unit vector normal to the interface
n_1	number of molecules per unit volume of body 1, m^{-3}
n_2	number of molecules per unit volume of body 2, m^{-3}
n_e	number of edges of bubble in 2D
$\langle n_e \rangle$	average number of edges
N	total number of bubbles
P_d	pressure inside bubble, Pa

P_k	gas pressure of k^{th} bubble, Pa
P_l	pressure outside bubble, Pa
r	radius of smaller bubble, m
r_s	radius of solid particle, m
R	radius of larger bubble, m
R_p	radius of parallel plates, m
R_1, R_2	principal radii of curvature, m
s	radial distance from axis of rotation, m
t	time, s
u	electrophoretic velocity of the particle in electric field, m s^{-1}
T	temperature, K
U	electric field, V m^{-1}
V	volume of bubble, m^3
V_k	volume of k^{th} bubble, m^3
$\langle V \rangle$	average volume, m^3
$\mathbf{x}$	present position vector
$\mathbf{x}'$	past position vector
z	valence

Greek letters

α	angular displacement, rad
γ	surface tension, N m^{-1}

γ_1	surface tension of phase 1, N m^{-1}
γ_2	surface tension of phase 2, N m^{-1}
$\dot{\gamma}$	shear rate, s^{-1}
$\dot{\gamma}_{R_p}$	strain rate at edge of parallel plates, s^{-1}
Δ	phase difference
ΔE	minimum energy, J
ΔP	pressure difference across the bubble surface, Pa
$\nabla \mathbf{v}$	velocity gradient tensor
ε	strain
$\dot{\varepsilon}$	strain rate, s^{-1}
ε_c	critical strain
ε_0	strain amplitude
ζ	zeta potential, V
η	viscosity, Pa s
η_s	interfacial shear viscosity, Pa s m
θ	contact angle, rad
κ	Debye–Hückel parameter, m^{-1}
λ	relaxation time, s
μ_i	refrective index
ν	dielectric constant of the medium
ν_0	permittivity of free space, C^2 J^{-1} m^{-1}

Π	disjoining pressure, Pa
Π_c	critical surface pressure, N m^{-1}
Π_e	disjoining pressure due to electrostatic double layer repulsion, Pa
Π_s	disjoining pressure due to short-range repulsion, Pa
Π_v	disjoining pressure due to van der Waals attraction, Pa
σ	shear stress, Pa
σ_1	shear stress in Hooke's law, Pa
σ_2	shear stress in Newton's law, Pa
σ_0	yield stress, Pa
σ_R	shear stress at periphery of parallel plates, Pa
σ_s	interfacial shear stress, Pa m
ϕ_c	confinement parameter of particles
ϕ_l	volume fraction of liquid in foam (or liquid content)
ϕ_p	volume fraction of particles
ψ	potential, V
ψ_m	potential at the half-separation between the surface, V
ψ_s	surface potential, V
ω	angular frequency, rad s^{-1}
Ω	angular velocity, rad s^{-1}

Abbreviations

AFM	atomic force microscope
CMC	critical micelle concentration
DLS	dynamic light scattering
HLB	hydrophilic–lipophilic balance
HTAB	hexadecyltrymethylammonium bromide
LAOS	large amplitude oscillatory shear
TEM	transmission electron microscope

References

(1) Manglik, R. M.; Wasekar, V. M.; Zhang, J. T. Dynamic and Equilibrium Surface Tension of Aqueous Surfactant and Polymeric Solutions. *Exp. Therm. Fluid Sci.* **2001,** *25*, 55–64.

(2) Hua, X. Y.; Rosen, M. J. Dynamic Surface Tension of Aqueou Surfactant Solution: 1. Basic Parameters. *J. Colloid Interface Sci.* **1988,** *124*, 652–659.

(3) Pileni, M. P. Reverse Micelles as Microreactors. *J. Phys. Chem.* **1993,** *97*, 6961–6973.

(4) Shiloach, A.; Blankschtein, D. Predicting Micellar Solution Properties of Binary Surfactant Mixtures. *Langmuir* **1998,** *14*, 1618–1636.

(5) Gauglitz, P. A.; Friedmann, F.; Kam, S. I.; Rossen, W. R. Foam Generation in Homogeneous Porous Media. *Chem. Eng. Sci.* **2002,** *57*, 4037–4052.

(6) Deshpande, N. S.; Barigou, M. The Flow of Gas–Liquid Foams in Vertical Pipes. *Chem. Eng. Sci.* **2000,** *55*, 4297–4309.

(7) Friedmann, F.; Jensen, J. In *Some Parameters Influencing the Formation and Propagation of Foams in Porous Media*, SPE California Regional Meeting, Society of Petroleum Engineers: 1986.

(8) Cohen-Addad, S.; Höhler, R.; Pitois, O. Flow in Foams and Flowing Foams. *Annu. Rev. Fluid Mech.* **2013,** *45*.

(9) Weaire, D. Kelvin's Foam Structure: A Commentary. *Philos. Mag. Lett.* **2008,** *88*, 91–102.

(10) Weaire, D. L.; Hutzler, S. *The Physics of Foams*; Oxford University Press: Oxford, 2001.

(11) Prud'homme, R. K.; Khan, S. A. *Foams Theory, Measurements, and Appications*; Vol. 57.

(12) Falls, A.; Hirasaki, G.; Patzek, T. e. a.; Gauglitz, D.; Miller, D.; Ratulowski, T. Development of a Mechanistic Foam Simulator: The Population Balance and Generation by Snap-off. *SPE Reservoir Eng.* **1988,** *3*, 884–892.

(13) Ruckenstein, E. The Origin of Thermodynamic Stability of Microemulsions. *Chem. Phys. Lett.* **1978,** *57*, 517–521.

(14) Gonzenbach, U. T.; Studart, A. R.; Tervoort, E.; Gauckler, L. J. Stabilization of Foams with Inorganic Colloidal Particles. *Langmuir* **2006,** *22,* 10983–10988.

(15) Pugh, R. J. Foaming, Foam Films, Antifoaming and Defoaming. *Adv. Colloid Interface Sci.* **1996,** *64,* 67–142.

(16) Drenckhan, W.; Saint-Jalmes, A. The Science of Foaming. *Adv. Colloid Interface Sci.* **2015,** *222,* 228–259.

(17) Karakashev, S. I.; Grozdanova, M. V. Foams and Antifoams. *Adv. Colloid Interface Sci.* **2012,** *176,* 1–17.

(18) Ramsden, W. Separation of Solids in the Surface-layers of Solutions and Suspensions (Observations on Surface-membranes, Bubbles, Emulsions, and Mechanical Coagulation)–Preliminary Account. *Proc. R. Soc. London* **1903,** *72,* 156–164.

(19) Hunter, T. N.; Pugh, R. J.; Franks, G. V.; Jameson, G. J. The Role of Particles in Stabilising Foams and Emulsions. *Adv. Colloid Interface Sci.* **2008,** *137,* 57–81.

(20) Dickinson, E. Structuring of Colloidal Particles at Interfaces and the Relationship to Food Emulsion and Foam Stability. *J. Colloid Interface Sci.* **2015,** *449,* 38–45.

(21) Binks, B. P. Particles as Surfactants–Similarities and Differences. *Curr. Opin. Colloid Interface Sci.* **2002,** *7,* 21–41.

(22) Carl, A.; Bannuscher, A.; von Klitzing, R. Particle Stabilized Aqueous Foams at Different Length Scales: Synergy between Silica Particles and Alkylamines. *Langmuir* **2015,** *31,* 1615–1622.

(23) Arriaga, L. R.; Drenckhan, W.; Salonen, A.; Rodrigues, J. A.; Iniguez-Palomares, R.; Rio, E.; Langevin, D. On the Long-term Stability of Foams Stabilised by Mixtures of Nano-particles and Oppositely Charged Short Chain Surfactants. *Soft Matter* **2012,** *8,* 11085–11097.

(24) Binks, B. P.; Murakami, R. Phase Inversion of Particle-stabilized Materials from Foams to Dry Water. *Nat. Mater.* **2006,** *5,* 865–869.

(25) Trahar, W. J. A Rational Interpretation of the Role of Particle-size in Flotation. *Int. J. Miner. Process.* **1981,** *8,* 289–327.

(26) Dickinson, E.; Ettelaie, R.; Kostakis, T.; Murray, B. S. Factors Controlling the Formation and Stability of Air Bubbles Stabilized by Partially Hydrophobic Silica Nanoparticles. *Langmuir* **2004,** *20,* 8517–8525.

(27) Stamou, D.; Duschl, C.; Johannsmann, D. Long-range Attraction between Colloidal Spheres at the Air–Water Interface: The Consequence of an Irregular Meniscus. *Phys. Rev. E.* **2000,** *62,* 5263–5272.

(28) Anjali, T. G.; Basavaraj, M. G. Shape-induced Deformation, Capillary Bridging, and Self-assembly of Cuboids at the Fluid–Fluid Interface. *Langmuir* **2017,** *33,* 791–801.

(29) Coertjens, S.; De Dier, R.; Moldenaers, P.; Isa, L.; Vermant, J. Adsorption of Ellipsoidal Particles at Liquid–Liquid Interfaces. *Langmuir* **2017,** *33,* 2689–2697.

(30) Denkov, N. D.; Ivanov, I. B.; Kralchevsky, P. A.; Wasan, D. T. A Possible Mechanism of Stabilization of Emulsions by Solid Particles. *J. Colloid Interface Sci.* **1992,** *150,* 589–593.

(31) Dickinson, E. Food Emulsions and Foams: Stabilization by Particles. *Curr. Opin. Colloid Interface Sci.* **2010,** *15,* 40–49.

(32) Zhang, Y.; Chang, Z.; Luo, W.; Gu, S.; Li, W.; An, J. Effect of Starch Particles on Foam Stability and Dilational Viscoelasticity of Aqueous Foam. *Chin. J. Chem. Eng.* **2015,** *23,* 276–280.

(33) Saint-Jalmes, A. Physical Chemistry in Foam Drainage and Coarsening. *Soft Matter* **2006,** *2,* 836–849.

(34) Saint-Jalmes, A.; Langevin, D. Time Evolution of Aqueous Foams: Drainage and Coarsening. *J. Phys.: Condens. Matter* **2002,** *14,* 9397–9412.

(35) Weaire, D.; Hutzler, S.; Verbist, G.; Peters, E. A Review of Foam Drainage. *Adv. Chem. Phys.* **1997,** *102,* 315–374.

(36) Koehler, S. A.; Hilgenfeldt, S.; Stone, H. A. A Generalized View of Foam Drainage: Experiment and Theory. *Langmuir* **2000,** *16,* 6327–6341.

(37) Stevenson, P. On the Forced Drainage of Foam. *Colloids Surf., A* **2007,** *305,* 1–9.

(38) Wang, J.; Nguyen, A. V. Foam Drainage in the Presence of Solid Particles. *Soft Matter* **2016,** *12,* 3004–3012.

(39) Narsimhan, G. Drainage of Particle Stabilized Foam Film. *Colloids Surf., A* **2016,** *495,* 20–29.

(40) Kaptay, G. On the Equation of the Maximum Capillary Pressure Induced by Solid Particles to Stabilize Emulsions and Foams and on the Emulsion Stability Diagrams. *colloids Surf., A* **2006,** *282,* 387–401.

(41) Nikolov, A. D.; Wasan, D. T. Dispersion Stability due to Structural Contributions to the Particle Interaction as Probed by Thin Liquid–Film Dynamics. *Langmuir* **1992,** *8,* 2985–2994.

(42) Rouyer, F.; Haffner, B.; Louvet, N.; Khidas, Y.; Pitois, O. Foam Clogging. *Soft Matter* **2014,** *10,* 6990–6998.

(43) Haffner, B.; Khidas, Y.; Pitois, O. The Drainage of Foamy Granular Suspensions. *J. Colloid Interface Sci.* **2015,** *458,* 200–208.

(44) Carn, F.; Colin, A.; Pitois, O.; Vignes-Adler, M. l.; Backov, R. Foam Drainage in the Presence of Nanoparticle−Surfactant Mixtures. *Langmuir* **2009,** *25,* 7847–7856.

(45) Gonatas, C. P.; Leigh, J. S.; Yodh, A. G.; Glazier, J. A.; Prause, B. Magnetic Resonance Images of Coarsening inside a Foam. *Phys. Rev. Lett.* **1995,** *75,* 573.

(46) Durian, D.; Weitz, D.; Pine, D. Dynamics and Coarsening in Three-dimensional Foams. *J. Phys.: Condens. Matter* **1990,** *2,* SA433.

(47) Maestro, A.; Rio, E.; Drenckhan, W.; Langevin, D.; Salonen, A. Foams Stabilised by Mixtures of Nanoparticles and Oppositely Charged Surfactants: Relationship between Bubble Shrinkage and Foam Coarsening. *Soft Matter* **2014,** *10,* 6975–6983.

(48) Stavans, J. The Evolution of Cellular Structures. *Rep. Prog. Phys.* **1993,** *56,* 733–789.

(49) Von Neumann, J. *Metal Interfaces*; American Society for Metals: Cleveland, 1952.

(50) Glazier, J. A.; Gross, S. P.; Stavans, J. Dynamics of Two-dimensional Soap Froths. *Phys. Rev. A* **1987,** *36,* 306.

(51) Sire, C. Growth Laws for 3d Soap Bubbles. *Phys. Rev. Lett.* **1994,** *72,* 420.

(52) Stavans, J.; Glazier, J. A. Soap Froth Revisited: Dynamic Scaling in the Two-Dimensional Froth. *Phys. Rev. Lett.* **1989,** *62,* 1318.

(53) MacPherson, R. D.; Srolovitz, D. J. The Von Neumann Relation Generalized to Coarsening of Three-dimensional Microstructures. *Nature* **2007,** *446,* 1053.

(54) Wu, F.-Y. The Potts Model. *Rev. Mod. Phys.* **1982,** *54,* 235–268.

(55) Glazier, J. A. Grain Growth in Three Dimensions Depends on Grain Topology. *Phys. Rev. Lett.* **1993,** *70,* 2170.

(56) Mullins, W. W. The Statistical Self-Similarity Hypothesis in Grain Growth and Particle Coarsening. *J. Appl. Phys.* **1986,** *59,* 1341–1349.

(57) Ghosh, P. *Colloid and Interface Science*; PHI Learning: 2009; Vol. Delhi.

(58) Edwards, D. A.; Brenner, H.; Wasan, D. T. *Interfacial Transport Processes and Rheology*; Butterworth–Heinemann: Stonheam, MA, 1991.

(59) Samanta, S.; Ghosh, P. Coalescence of Bubbles and Stability of Foams in Aqueous Solutions of Tween Surfactants. *Chem. Eng. Res. Des.* **2011,** *89,* 2344–2355.

(60) Mitra, T.; Ghosh, P. Binary Coalescence of Water Drops in Organic Media in Presence of Ionic Surfactants and Salts. *J. Dispersion Sci. Technol.* **2007,** *28,* 785–792.

(61) Blanco, E.; Lam, S.; Smoukov, S. K.; Velikov, K. P.; Khan, S. A.; Velev, O. D. Stability and Viscoelasticity of Magneto-pickering Foams. *Langmuir* **2013,** *29,* 10019–10027.

(62) Vijayaraghavan, K.; Nikolov, A.; Wasan, D.; Henderson, D. Foamability of Liquid Particle Suspensions: A Modeling Study. *Ind. Eng. Chem. Res.* **2009,** *48,* 8180–8185.

(63) Briggs, A. A. Foams for Firefighting. *Foams: Theory, Measurements and Applications* **1995,** *57,* 465–509.

(64) Moody, C. A.; Martin, J. W.; Kwan, W. C.; Muir, D. C.; Mabury, S. A. Monitoring Perfluorinated Surfactants in Biota and Surface Water Samples Following an Accidental Release of Fire-fighting Foam into Etobicoke Creek. *Environ. Sci. Technol.* **2002,** *36,* 545–551.

(65) Farajzadeh, R.; Andrianov, A.; Krastev, R.; Hirasaki, G.; Rossen, W. R. Foam–Oil Interaction in Porous Media: Implications for Foam Assisted Enhanced Oil Recovery. *Adv. Colloid Interface Sci.* **2012,** *183,* 1–13.

(66) Rossen, W. R. Foams in Enhanced Oil Recovery. *Surfactant Sci. Ser.* **1996,** 413–464.

(67) Biesterbos, J. W.; Dudzina, T.; Delmaar, C. J.; Bakker, M. I.; Russel, F. G.; von Goetz, N.; Scheepers, P. T.; Roeleveld, N. Usage Patterns of Personal Care Products: Important Factors for Exposure Assessment. *Food Chem. Toxicol.* **2013,** *55,* 8–17.

(68) Green, A. J.; Littlejohn, K. A.; Hooley, P.; Cox, P. W. Formation and Stability of Food Foams and Aerated Emulsions: Hydrophobins as Novel Functional Ingredients. *Curr. Opin. Colloid Interface Sci.* **2013,** *18,* 292–301.

(69) Dickinson, E. Structuring of Colloidal Particles at Interfaces and the Relationship to Food Emulsion and Foam Stability. *J. Colloid Interface Sci.* **2015,** *449,* 38-45.

(70) Cooke, T. F.; Hirt, D. E., Foam Wet Processing in the Textile Industry. In *Foams: Theory, Measurements and Applications*, 1995; Vol. 57, pp 339–380.

(71) Cooke, T. F. Formaldehyde Release from Durable Press Fabrics. *Text. Chem. Color.* **1983,** *15,* 13–34.

(72) Marze, S.; Guillermic, R. M.; Saint-Jalmes, A. Oscillatory Rheology of Aqueous Foams: Surfactant, Liquid Fraction, Experimental Protocol and Aging Effects. *Soft Matter* **2009,** *5,* 1937–1946.

(73) Cox, S.; Weaire, D.; Glazier, J. A. The Rheology of Two-dimensional Foams. *Rheol. Acta* **2004,** *43,* 442–448.

(74) Khan, S. A.; Schnepper, C. A.; Armstrong, R. C. Foam Rheology: Iii. Measurement of Shear Flow Properties. *J. Rheol.* **1988,** *32,* 69–92.

(75) Bingham, E. An Investigation of the Laws of Plastic Flow. **1916,** *13,* 309–353.

(76) Herschel, W. H.; Bulkley, R. Konsistenzmessungen Von Gummi-Benzollösungen. *Colloid Polym. Sci.* **1926,** *39,* 291–300.

(77) Ovarlez, G.; Rodts, S.; Ragouilliaux, A.; Coussot, P.; Goyon, J.; Colin, A. Wide-gap Couette Flows of Dense Emulsions: Local Concentration Measurements, and Comparison between Macroscopic and Local Constitutive Law Measurements through Magnetic Resonance Imaging. *Phys. Rev. E.* **2008,** *78,* 036307.

(78) Cohen-Addad, S.; Höhler, R. Rheology of Foams and Highly Concentrated Emulsions. *Curr. Opin. Colloid Interface Sci.* **2014,** *19,* 536–548.

(79) Batchelor, G. K. The Stress System in a Suspension of Force-free Particles. *J. Fluid Mech.* **1970,** *41,* 545–570.

(80) Höhler, R.; Cohen-Addad, S. Rheology of Liquid Foam. *J. Phys.: Condens. Matter* **2005,** *17,* 1041–1069.

(81) Khan, S. A.; Armstrong, R. C. Rheology of Foams: 1. Theory for Dry Foams. *J. Non-Newtonian Fluid Mech.* **1986,** *22,* 1–22.

(82) Kraynik, A. M.; Hansen, M. G. Foam Rheology: A Model of Viscous Phenomena. *J. Rheol.* **1987,** *31,* 175–205.

(83) Reinelt, D. A.; Kraynik, A. M. Simple Shearing Flow of Dry Soap Foams with Tetrahedrally Close-packed Structure. *J. Rheol.* **2000,** *44,* 453–471.

(84) Kraynik, A. M. Foam Flows. *Annu. Rev. Fluid Mech.* **1988,** *20,* 325–357.

(85) Macosko, C. W. *Rheology: Principles, Measurements, and Applications*; Wiley-VCH: New York, 1994.

(86) Bird, R. B.; Armstrong, R. C.; Hassager, O. *Dynamics of Polymeric Liquids: Volume 1 Fluid Mechanics*; Wiley: New York, 1987.

(87) Maxwell, J. C. On the Dynamical Theory of Gases. *Philos. Trans. R. Soc. London* **1867,** *157,* 49–88.

(88) Höhler, R.; Cohen-Addad, S.; Hoballah, H. Periodic Nonlinear Bubble Motion in Aqueous Foam under Oscillating Shear Strain. *Phys. Rev. Lett.* **1997,** *79,* 1154.

(89) Gopal, A. D.; Durian, D. J. Relaxing in Foam. *Phys. Rev. Lett.* **2003,** *91,* 188303.

(90) Cohen-Addad, S.; Höhler, R.; Khidas, Y. Origin of the Slow Linear Viscoelastic Response of Aqueous Foams. *Phys. Rev. Lett.* **2004,** *93,* 028302.

(91) Lounis, M.; Bekkour, K. Rheological Characterization of SDS/Peo based Foams. *J. Mater. Sci. Lett.* **2002,** *21,* 1573–1575.

(92) Stamenovic, D. A Model of Foam Elasticity based upon the Laws of Plateau. *J. Colloid Interface Sci.* **1991,** *145,* 255–259.

(93) Mason, T. G.; Bibette, J.; Weitz, D. A. Yielding and Flow of Monodisperse Emulsions. *J. Colloid Interface Sci.* **1996,** *179,* 439–448.

(94) Hebraud, P.; Lequeux, F.; Palierne, J. F. Role of Permeation in the Linear Viscoelastic Response of Concentrated Emulsions. *Langmuir* **2000,** *16,* 8296–8299.

(95) Derec, C.; Ducouret, G.; Ajdari, A.; Lequeux, F. Aging and Nonlinear Rheology in Suspensions of Polyethylene Oxide–Protected Silica Particles. *Phys. Rev. E.* **2003,** *67,* 061403.

(96) Barnes, H. A. A Review of the Slip (Wall Depletion) of Polymer Solutions, Emulsions and Particle Suspensions in Viscometers: Its Cause, Character, and Cure. *J. Non-Newtonian Fluid Mech.* **1995,** *56,* 221–251.

(97) Ballesta, P.; Petekidis, G.; Isa, L.; Poon, W.; Besseling, R. Wall Slip and Flow of Concentrated Hard-sphere Colloidal Suspensions. *J. Rheol.* **2012,** *56,* 1005–1037.

(98) Denkov, N. D.; Subramanian, V.; Gurovich, D.; Lips, A. Wall Slip and Viscous Dissipation in Sheared Foams: Effect of Surface Mobility. *Colloids Surf., A* **2005,** *263,* 129–145.

(99) Mooney, M. Explicit Formulas for Slip and Fluidity. *J. Rheol.* **1931,** *210,* 210–222.

(100) Habibi, M.; Dinkgreve, M.; Paredes, J.; Denn, M. M.; Bonn, D. Normal Stress Measurement in Foams and Emulsions in the Presence of Slip. *J. Non-Newtonian Fluid Mech.* **2016,** *238,* 33–43.

(101) Herzhaft, B. Rheology of Aqueous Foams: A Literature Review of Some Experimental Works. *Oil Gas Sci. Technol.* **1999,** *54,* 587–596.

(102) Barnes, H. A. Measuring the Viscosity of Large-particle (and Flocculated) Suspensions – a Note on the Necessary Gap Size of Rotational Viscometers. *J. Non-Newtonian Fluid Mech.* **2000,** *94,* 213–217.

(103) Tan, K.; Cheng, S.; Jugé, L.; Bilston, L. E. Characterising Soft Tissues under Large Amplitude Oscillatory Shear and Combined Loading. *J. Biomech.* **2013,** *46,* 1060–1066.

(104) Yoshimura, A.; Prud'homme, R. K. Wall Slip Corrections for Couette and Parallel Disk Viscometers. *J. Rheol.* **1988,** *32,* 53–67.

(105) Cloitre, M.; Bonnecaze, R. T. A Review on Wall Slip in High Solid Dispersions. *Rheol. Acta* **2017,** *56,* 283–305.

(106) Rabinowitsch, B. Über Die Viskosität Und Elastizität Von Solen. *Zeitschrift für physikalische Chemie* **1929,** *145,* 1–26.

(107) Soskey, P. R.; Winter, H. H. Large Step Shear Strain Experiments with Parallel-Disk Rotational Rheometers. *J. Rheol.* **1984,** *28,* 625–645.

(108) Giesekus, H. A Simple Contitutive Equation for Polymer Fluids based on the Concept of Deformation-dependent Tensorial Mobility. *J. Non-Newtonian Fluid Mech.* **1982,** *11,* 69–109.

(109) Gurnon, A. K.; Wagner, N. J. Large Amplitude Oscillatory Shear (LAOS) Measurements to Obtain Constitutive Equation Model Parameters: Giesekus Model of Banding and Nonbanding Wormlike Micelles. *J. Rheol.* **2012,** *56,* 333–351.

(110) Khair, A. S. Large Amplitude Oscillatory Shear of the Giesekus Model. *J. Rheol.* **2016,** *60*, 257–266.

(111) Jacob, A. R.; Deshpande, A. P.; Bouteiller, L. Large Amplitude Oscillatory Shear of Supramolecular Materials. *J. Non-Newtonian Fluid Mech.* **2014,** *206*, 40–56.

(112) Carvalho, M.; Padmanabhan, M.; Macosko, C. Single-Point Correction for Parallel Disks Rheometry. *J. Rheol.* **1994,** *38*, 1925–1936.

(113) Fahimi, Z.; Broedersz, C. P.; van Kempen, T. H.; Florea, D.; Peters, G. W.; Wyss, H. M. A New Approach for Calculating the True Stress Response from Large Amplitude Oscillatory Shear (LAOS) Measurements using Parallel Plates. *Rheol. Acta* **2014,** *53*, 75–83.

(114) Giacomin, A. J.; Gilbert, P. H.; Merger, D.; Wilhelm, M. Large Amplitude Oscillatory Shear: Comparing Parallel-disk with Cone-plate Flow. *Rheol. Acta* **2015,** *54*, 263–285.

(115) Derjaguin, B. V.; Churaev, N. V. Structure Component of Disjoining Pressure. *J. Colloid Interface Sci.* **1974,** *49*, 249–255.

(116) Derjaguin, B. V. Friction and Adhesion: Iv. The Theory of Adhesion of Small Particles. *Kolloid Zeit.* **1934,** *69*, 155–164.

(117) Derjaguin, B. On the Repulsive Forces between Charged Colloid Particles and on the Theory of Slow Coagulation and Stability of Lyophobe Sols *Trans. Faraday Soc.* **1940,** *35*.

(118) Hamaker, H. C. The London–Van Der Waals Attraction between Spherical Particles. *Physica* **1937,** *4*, 1058–1072.

(119) London, F. The General Theory of Molecular Forces. *Trans. Faraday Soc.* **1937,** *33*, 8–26.

(120) Lifshitz, E. M. The Theory of Molecular Attractive Forces between Solids. *Sov. Phys. JEPT* **1956,** *2*, 73–83.

(121) Israelachvili, J. N. *Intermolecular and Surface Forces*; Academic press: New York, 2011.

(122) Verwey, E. J. W.; Overbeek, J. Th. G. *Theory of Stability of Lyophobic Colloids*; Elsevier: Amsterdam, 1948.

(123) Gregory, J. Interaction of Unequal Double Layers at Constant Charge. *J. Colloid Interface Sci.* **1975,** *51,* 44–51.

(124) Manciu, M.; Ruckenstein, E. Ions near the Air/Water Interface. Ii: Is the Water/Air Interface Acidic or Basic? Predictions of a Simple Model. *Colloids Surf., A* **2012,** *404,* 93–100.

(125) Sainath, K.; Ghosh, P. Stabilization of Silicone Oil-in-water Emulsions by Ionic Surfactant and Electrolytes: The Role of Adsorption and Electric Charge at the Interface. *Ind. Eng. Chem. Res.* **2013,** *52,* 15808–15816.

(126) Hiemenz, P. C.; Rajagopalan, R. *Principles of Colloid and Surface Chemistry*; Marcel Dekker: New York, 1997.

(127) Bergeron, V.; Radke, C. J. Equilibrium Measurements of Oscillatory Disjoining Pressures in Aqueous Foam Films. *Langmuir* **1992,** *8,* 3020–3026.

(128) Stubenrauch, C.; von Klitzing, R. Disjoining Pressure in Thin Liquid Foam and Emulsion Films – New Concepts and Perspectives. *J. Phys.: Condens. Matter* **2003,** *15,* R1197–R1232.

(129) Danov, K. D.; Ivanov, I. B.; Ananthapadmanabhan, K. P.; Lips, A. Disjoining Pressure of Thin Films Stabilized by Nonionic Surfactants. *Adv. Colloid Interface Sci.* **2006,** *128,* 185–215.

(130) Derjaguin, B. V. *Theory of Stability of Colloids and Thin Liquid Films*; Plenum Press: New York, 1989.

(131) Bergeron, V. Forces and Structure in Thin Liquid Soap Films. *J. Phys.: Condens. Matter* **1999,** *11,* R215–R238.

(132) Ninham, B. W.; Pashley, R. M.; Nostro, P. L. Surface Forces: Changing Concepts and Complexity with Dissolved Gas, Bubbles, Salt and Heat. *Curr. Opin. Colloid Interface Sci.* **2017,** *27,* 25–32.

(133) Joye, J.-L.; Miller, C. A.; Hirasaki, G. J. Dimple Formation and Behavior During Axisymmetrical Foam Film Drainage. *Langmuir* **1992,** *8,* 3083–3092.

(134) Clunie, J. S.; Goodman, J. F.; Symons, P. C. Solvation Forces in Soap Films. *Nature* **1967,** *216,* 1203–1204.

(135) Nikolov, A. D.; Wasan, D. T. Ordered Micelle Structuring in Thin Films Formed from Anionic Surfactant Solutions: I. Experimental. *J. Colloid Interface Sci.* **1989,** *133,* 1–12.

(136) Chu, X. L.; Nikolov, A. D.; Wasan, D. T. Thin Liquid Film Structure and Stability: The Role of Depletion and Surface-Induced Structural Forces. *J. Chem. Phys.* **1995,** *103,* 6653–6661.

(137) Chu, X.; Nikolov, A.; Wasan, D. Effects of Particle Size and Polydispersity on the Depletion and Structural Forces in Colloidal Dispersions. *Langmuir* **1996,** *12,* 5004–5010.

(138) Sethumadhavan, G. N.; Nikolov, A.; Wasan, D. Film Stratification in the Presence of Colloidal Particles. *Langmuir* **2001,** *17,* 2059–2062.

(139) Manev, E. D.; Sazdanova, S. V.; Wasan, D. T. Stratification in Emulsion Films. *J. Dispersion Sci. Technol.* **1984,** *5,* 111–117.

(140) Wasan, D. T.; Nikolov, A. D.; Aimetti, F. Texture and Stability of Emulsions and Suspensions: Role of Oscillatory Structural Forces. *Adv. Colloid Interface Sci.* **2004,** *108,* 187–195.

(141) Asakura, S.; Oosawa, F. On Interaction between Two Bodies Immersed in a Solution of Macromolecules. *J. Chem. Phys.* **1954,** *22,* 1255–1256.

(142) Kralchevsky, P. A.; Nagayama, K. Capillary Interactions between Particles Bound to Interfaces, Liquid Films and Biomembranes. *Adv. Colloid Interface Sci.* **2000,** *85,* 145–192.

(143) Kaptay, G. On the Equation of the Maximum Capillary Pressure Induced by Solid Particles to Stabilize Emulsions and Foams and on the Emulsion Stability Diagrams. *Colloids Surf. A* **2006,** *282,* 387–401.

(144) Ali, S. A.; Gauglitz, P. A.; Rossen, W. R. Stability of Solids-coated Liquid Layers between Bubbles. *Ind. Eng. Chem. Res.* **2000,** *39,* 2742–2745.

(145) Vignati, E.; Piazza, R.; Lockhart, T. P. Pickering Emulsions: Interfacial Tension, Colloidal Layer Morphology, and Trapped-particle Motion. *Langmuir* **2003,** *19,* 6650–6656.

(146) Fernandez-Rodriguez, M. A.; Rodriguez-Valverde, M. A.; Cabrerizo-Vilchez, M. A.; Hidalgo-Alvarez, R. Surface Activity of Janus Particles Adsorbed at Fluid–Fluid

Interfaces: Theoretical and Experimental Aspects. *Adv. Colloid Interface Sci.* **2016,** *233*, 240–254.

(147) Jiang, S.; Chen, Q.; Tripathy, M.; Luijten, E.; Schweizer, K. S.; Granick, S. Janus Particle Synthesis and Assembly. *Adv. Mater.* **2010,** *22*, 1060–1071.

(148) Walther, A.; Müller, A. H. Janus Particles: Synthesis, Self-assembly, Physical Properties, and Applications. *Chem. Rev.* **2013,** *113*, 5194–5261.

(149) Pickering, S. U. Cxcvi.—Emulsions. *J. chem. Soc. Trans.* **1907,** *91*, 2001–2021.

(150) Heuman, D. M. Quantitative Estimation of the Hydrophilic–Hydrophobic Balance of Mixed Bile Salt Solutions. *J. Lipid Res.* **1989,** *30*, 719–730.

(151) Schott, H. Hydrophilic–Lipophilic Balance, Solubility Parameter, and Oil–Water Partition Coefficient as Universal Parameters of Nonionic Surfactants. *J. Pharm. Sci.* **1995,** *84*, 1215–1222.

(152) Binks, B. P.; Lumsdon, S. O. Influence of Particle Wettability on the Type and Stability of Surfactant-free Emulsions. *Langmuir* **2000,** *16*, 8622–8631.

(153) Binks, B. P.; Lumsdon, S. O. Catastrophic Phase Inversion of Water-in-oil Emulsions Stabilized by Hydrophobic Silica. *Langmuir* **2000,** *16*, 2539–2547.

(154) Zhang, S. Y.; Lan, Q.; Liu, Q.; Xu, H.; Sun, D. J. Aqueous Foams Stabilized by Laponite and CTAB. *Colloids Surf., A* **2008,** *317*, 406–413.

(155) Gonzenbach, U. T.; Studart, A. R.; Tervoort, E.; Gauckler, L. J. Ultrastable Particle-Stabilized Foams. *Angew. Chem. Int. Ed.* **2006,** *45*, 3526–3530.

(156) Binks, B. P.; Kirkland, M.; Rodrigues, J. A. Origin of Stabilisation of Aqueous Foams in Nanoparticle–Surfactant Mixtures. *Soft Matter* **2008,** *4*, 2373–2382.

(157) Zhu, Y.; Pei, X.; Jiang, J.; Cui, Z.; Binks, B. P. Responsive Aqueous Foams Stabilized by Silica Nanoparticles Hydrophobized in Situ with a Conventional Surfactant. *Langmuir* **2015,** *31*, 12937–12943.

(158) Binks, B. P.; Horozov, T. S. *Colloidal Particles at Liquid Interfaces*; Cambridge University Press: Cambridge, 2006.

(159) Kaptay, G. Interfacial Criteria for Stabilization of Liquid Foams by Solid Particles. *Colloids Surf. A* **2004,** *230*, 67–80.

(160) Abdel-Fattah, A. I.; El-Genk, M. S. On Colloidal Particle Sorption onto a Stagnant Air–Water Interface. *Adv. Colloid Interface Sci.* **1998,** *78*, 237–266.

(161) Bournival, G.; Ata, S.; Wanless, E. J. The Roles of Particles in Multiphase Processes: Particles on Bubble Surfaces. *Adv. Colloid Interface Sci.* **2015,** *225,* 114–133.

(162) Aveyard, R.; Binks, B. P.; Clint, J. H. Emulsions Stabilised Solely by Colloidal Particles. *Adv. Colloid Interface Sci.* **2003,** *100,* 503–546.

(163) Clint, J. H.; Taylor, S. E. Particle Size and Interparticle Forces of Overbased Detergents: A Langmuir Trough Study. *Colloids Surf.* **1992,** *65,* 61–67.

(164) Frye, G. C.; Berg, J. C. Antifoam Action by Solid Particles. *J. Colloid Interface Sci.* **1989,** *127,* 222–238.

(165) Karbaschi, M.; Lotfi, M.; Krägel, J.; Javadi, A.; Bastani, D.; Miller, R. Rheology of Interfacial Layers. *Curr. Opin. Colloid Interface Sci.* **2014,** *19,* 514–519.

(166) Pradilla, D.; Simon, S.; Sjöblom, J.; Samaniuk, J.; Skrzypiec, M.; Vermant, J. Sorption and Interfacial Rheology Study of Model Asphaltene Compounds. *Langmuir* **2016,** *32,* 2900–2911.

(167) Miller, R.; Ferri, J. K.; Javadi, A.; Krägel, J.; Mucic, N.; Wüstneck, R. Rheology of Interfacial Layers. *Colloid Polym. Sci.* **2010,** *288,* 937–950.

(168) Madivala, B.; Fransaer, J.; Vermant, J. Self-assembly and Rheology of Ellipsoidal Particles at Interfaces. *Langmuir* **2009,** *25,* 2718–2728.

(169) Krägel, J.; Derkatch, S. R. Interfacial Shear Rheology. *Curr. Opin. Colloid Interface Sci.* **2010,** *15,* 246–255.

(170) Fuller, G. G.; Vermant, J. Complex Fluid–Fluid Interfaces: Rheology and Structure. *Annu. Rev. Chem. Biomol. Eng.* **2012,** *3,* 519–543.

(171) Mendoza, A. J.; Guzman, E.; Martinez-Pedrero, F.; Ritacco, H.; Rubio, R. G.; Ortega, F.; Starov, V. M.; Miller, R. Particle Laden Fluid Interfaces: Dynamics and Interfacial Rheology. *Adv Colloid Interface Sci* **2014,** *206,* 303–319.

(172) Stocco, A.; Rio, E.; Binks, B. P.; Langevin, D. Aqueous Foams Stabilized Solely by Particles. *Soft Matter* **2011,** *7,* 1260–1267.

(173) Meinders, M. B.; van Vliet, T. The Role of Interfacial Rheological Properties on Ostwald Ripening in Emulsions. *Adv. Colloid Interface Sci.* **2004,** *108,* 119–126.

(174) Gupta, M.; Van Hooghten, R.; Fischer, P.; Gunes, D. Z.; Vermant, J. Limiting Coalescence by Interfacial Rheology: Over-compressed Polyglycerol Ester Layers. *Rheol. Acta* **2016,** *55*, 537–546.

(175) Slattery, J. C. *Interfacial Transport Phenomena*; Springer-Verlag: New York, 1990.

(176) Langevin, D. Influence of Interfacial Rheology on Foam and Emulsion Properties. *Adv. Colloid Interface Sci.* **2000,** *88*, 209–222.

(177) Vandebril, S.; Franck, A.; Fuller, G. G.; Moldenaers, P.; Vermant, J. A Double Wall-ring Geometry for Interfacial Shear Rheometry. *Rheol. Acta* **2010,** *49*, 131–144.

(178) Erni, P.; Fischer, P.; Windhab, E. J.; Kusnezov, V.; Stettin, H.; Laüger, J. Stress- and Strain-controlled Measurements of Interfacial Shear Viscosity and Viscoelasticity at Liquid/Liquid and Gas/Liquid Interfaces. *Rev. Sci. Instrum.* **2003,** *74*, 4916–4924.

(179) Brooks, C. F.; Fuller, G. G.; Frank, C. W.; Robertson, C. R. An Interfacial Stress Rheometer to Study Rheological Transitions in Monolayers at the Air–Water Interface. *Langmuir* **1999,** *15*, 2450–2459.

(180) Safouane, M.; Langevin, D.; Binks, B. P. Effect of Particle Hydrophobicity on the Properties of Silica Particle Layers at the Air−Water Interface. *Langmuir* **2007,** *23*, 11546–11553.

(181) Cicuta, P.; Stancik, E. J.; Fuller, G. G. Shearing or Compressing a Soft Glass in 2D: Time-concentration Superposition. *Phys. Rev. Lett.* **2003,** *90*, 236101.

(182) Lexis, M.; Willenbacher, N. Yield Stress and Elasticity of Aqueous Foams from Protein and Surfactant Solutions – the Role of Continuous Phase Viscosity and Interfacial Properties. *Colloids Surf., A* **2014,** *459*, 177–185.

(183) Zang, D. Y.; Rio, E.; Langevin, D.; Wei, B.; Binks, B. P. Viscoelastic Properties of Silica Nanoparticle Monolayers at the Air–Water Interface. *Eur. Phys. J. E* **2010,** *31*, 125–134.

(184) Sharma, V.; Jaishankar, A.; Wang, Y.-C.; McKinley, G. H. Rheology of Globular Proteins: Apparent Yield Stress, High Shear Rate Viscosity and Interfacial

Viscoelasticity of Bovine Serum Albumin Solutions. *Soft Matter* **2011,** *7*, 5150–5160.

(185) Hyun, K.; Kim, S. H.; Ahn, K. H.; Lee, S. J. Large Amplitude Oscillatory Shear as a Way to Classify the Complex Fluids. *J. Non-Newtonian Fluid Mech.* **2002,** *107*, 51–65.

(186) Ewoldt, R. H.; Hosoi, A. E.; McKinley, G. H. New Measures for Characterizing Nonlinear Viscoelasticity in Large Amplitude Oscillatory Shear. *J. Rheol.* **2008,** *52*, 1427–1458.

(187) Cho, K. S.; Hyun, K.; Ahn, K. H.; Lee, S. J. A Geometrical Interpretation of Large Amplitude Oscillatory Shear Response. *J. Rheol.* **2005,** *49*, 747–758.

(188) Yu, W.; Wang, P.; Zhou, C. General Stress Decomposition in Nonlinear Oscillatory Shear Flow. *J. Rheol.* **2009,** *53*, 215–238.

(189) Birbaum, F. C.; Haavisto, S.; Koponen, A.; Windhab, E. J.; Fischer, P. Shear Localisation in Interfacial Particle Layers and Its Influence on Lissajous-plots. *Rheol. Acta* **2016,** *55*, 267–278.

(190) Sagis, L. M. C.; Fischer, P. Nonlinear Rheology of Complex Fluid–Fluid Interfaces. *Curr. Opin. Colloid Interface Sci.* **2014,** *19*, 520–529.

(191) Erni, P.; Parker, A. Nonlinear Viscoelasticity and Shear Localization at Complex Fluid Interfaces. *Langmuir* **2012,** *28*, 7757–7767.

(192) Rühs, P. A.; Affolter, C.; Windhab, E. J.; Fischer, P. Shear and Dilatational Linear and Nonlinear Subphase Controlled Interfacial Rheology of Beta-lactoglobulin Fibrils and their Derivatives. *J. Rheol.* **2013,** *57*, 1003–1022.

(193) Hyun, K.; Wilhelm, M.; Klein, C. O.; Cho, K. S.; Nam, J. G.; Ahn, K. H.; Lee, S. J.; Ewoldt, R. H.; McKinley, G. H. A Review of Nonlinear Oscillatory Shear Tests: Analysis and Application of Large Amplitude Oscillatory Shear (LAOS). *Prog. Polym. Sci.* **2011,** *36*, 1697–1753.

Chapter 2

Materials and Experimental Methods

2.1 Materials

The cationic surfactant (i.e. HTAB) used in the study was purchased from Merck [Hohenbrunn (Germany), 97% assay]. Negatively-charged silicon dioxide nanoparticles were purchased from Plasmachem [Berlin (Germany), 92.7% assay]. The mean diameter of these particles was ~185 nm. All samples were prepared using water, purified by a Millipore system [manufacturer: Molshein (France), model: Elix plus Milli-Q]. Its resistivity and surface tension were 18.2 MΩ cm and 72.5 mN m^{-1}, respectively.

2.2 Sample preparation

Due to their large size and the surface wetting properties, the silica nanoparticles do not adsorb at the air–water interfaces. Their surface properties can be altered by adding HTAB. To study the effect of HTAB on foam, three samples of different concentrations of HTAB were prepared. The first sample was below the CMC (i.e. 0.1 mol m^{-3}), the second sample was near the CMC (i.e. 1 mol m^{-3}), and the third sample was above the CMC (i.e. 10 mol m^{-3}). The required amount of HTAB was added to the dispersion of the nanoparticles, followed by a thorough mixing using a magnetic stirrer [manufacturer: Tarsons (India), model: MC 02] for 15 min at 250 rpm. All samples contained a fixed amount of silica nanoparticles (i.e. 0.5 wt%).

To study the large amplitude oscillatory shear (LAOS) behavior of foam, an aqueous dispersion containing 0.1 mol m^{-3} HTAB and 0.5% (by weight) silica

nanoparticles was prepared by mixing them using the magnetic stirrer. Higher concentrations of HTAB were not taken because the foams were less stable in the presence of the nanoparticles when the concentration of HTAB was above the CMC.[1] The aqueous dispersion (200 cm^3) was poured into the jar of the blender, and the dispersion was mixed at a speed of 15000 rpm for 30 s. The foam prepared in this manner was used for the rheological studies under LAOS.

To study the effect of nanoparticles on the foam, three sets of surfactant solutions were prepared. In these solutions, the HTAB concentrations were 0.1, 1, and 10 mol m^{-3}, as mentioned earlier. The experiments were performed at each surfactant concentration by varying the particle concentration. The particle concentration was varied from 0 to 0.5 wt%. These dispersions were used to study the effect of particle concentration on the air–water interface in the presence of HTAB. Foams were generated with these dispersions. No significant effect was observed above 0.5 wt% particle concentration. Therefore, particle concentrations above 0.5 wt% were not studied further.

2.3 Particle size distribution and zeta potential measurements

The particle size distribution and the zeta potential at the particle–solution interface were measured by using a particle size analyzer and a zeta potentiometer, respectively. Both systems were integrated in the same equipment [manufacturer: Beckman Coulter (Switzerland), model: Delsa Nano C]. Measurement of these quantities enabled us to understand the interaction between the particles in the presence of surfactant. The zeta potential was measured from the electrophoretic mobility of the particles.[2] Each measurement was repeated five times, and their average value is reported. The particle

size was measured by dynamic light scattering (DLS), and the size distribution is reported.[3]

2.4 Foam stability and foamability

To generate the foam, the aqueous dispersion (200 cm^3) was poured into the jar of a blender [manufacturer: Morphy Richards (India), model: Divo Essentials] and the dispersion was mixed at a speed of 15000 rpm for 30 s, which resulted in the formation of the foam. Thereafter, the foam was placed in a graduated 500 cm^3 glass cylinder. The solutions and resulted foams were analyzed. The change in the height of the foams with time was recorded. The photographs of the foam were taken at different time intervals by using a digital camera [manufacturer: Nikon (India), model: D5100].

2.5 Rheology of foams

The rheological behavior of the foams was studied by using a rheometer [manufacturer: Anton Paar (Germany), model: Physica MCR 301] with a parallel-plate geometry (diameter of plate = 50 mm). The foam was placed between the two plates, and the gap between the plates was fixed at 1 mm during the measurements. The upper plate was moved with the motor connected to the rheometer, and the lower plate remained stationary. The yield stress and elasticity are the two important parameters, which give an idea about the strength associated with the foam.[4] The yield stress was measured in the rotation mode, and the elasticity (or viscoelasticity) was measured in the oscillation mode. Before starting the experiments, the slip condition was checked by measuring the

shear stress as a function of apparent shear rate at different gaps between the parallel plates. Additionally, dynamic stability was checked by measuring the shear stress with time at a fixed shear rate. No change in shear stress was observed up to 15 min, which confirmed the stability of the foam during the rheological measurements (as all of our experiments were completed before this time).

Figure 2.1 Photograph of the rheometer [manufacturer: Anton Paar (Germany), model: Physica MCR 301].

The LAOS behavior of the foam was studied in the same rheometer with a parallel-plate geometry (diameter of plate = 25 mm). Both the plates were roughened by sand blasting to avoid any slip during the experiments. Despite the heterogeneous deformation, the parallel-plate geometry was selected because the gap between the plates could be adjusted easily. The temperature was set to 298 K, and it was controlled within ±0.1 K using a standard Peltier device. The LAOS tests were performed at four oscillation frequencies (ω), i.e. 0.1, 1, 10, and 15 rad s^{-1}, and nine strain amplitudes (γ_0), i.e. 1, 6.31, 10, 15.9, 25.1, 39.8, 63.1, 100, and 159%. For each ω and γ_0, the stress was measured as a function of input oscillatory strain (or strain rate) in a complete cycle

to produce the Lissajous–Bowditch curves. These curves were shown in a three dimensional coordinate system, where strain, strain rate, and stress were the orthogonal coordinate axes. The projections of this curve onto the stress vs. strain and stress vs. strain-rate planes are known as *elastic* and *viscous Lissajous–Bowditch curve*, respectively.[5] These curves were shown in the *Pipkin space*, which is a compact representation of the Lissajous–Bowditch curves in an experimental test space that may be adjusted by two input parameters, i.e. ω and γ_0.[6] Each measurement was repeated three times to verify the repeatability. The slip condition was checked by measuring the shear stress as a function of shear rate at different gaps between the parallel plates (Figure 2.2).[7-9] It was observed that the data points almost superposed for all gaps, which confirmed the absence of slip. We have also compared our experimental results with the oscillatory stress response derived for the cone-and-plate geometry,[10] where homogeneous deformation can be achieved.

A Fourier series was used to fit the distorted stress response, obtained from the LAOS experiment. From the stress data points, the Fourier coefficients were computed. These coefficients are the in- and out-of-phase stress components of the shear deformation. The relative intensity of the third and the fifth harmonics was determined with respect to the first harmonic terms. To study the contribution of the higher harmonic terms to LAOS, the time domain of Fourier series was converted into the frequency domain. Additionally, Chebyshev polynomials were used to fit the Lissajous–Bowditch curves obtained under LAOS.

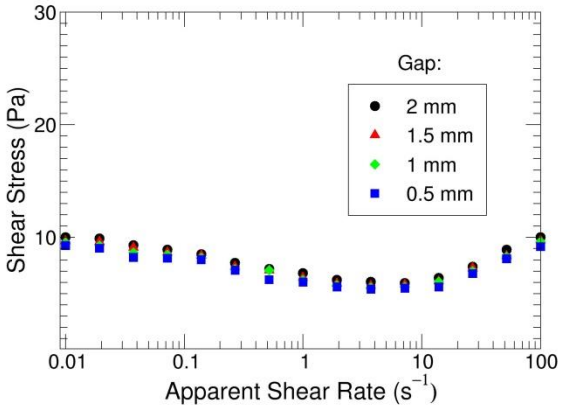

Figure 2.2 Measurement of shear stress as a function of apparent shear rate at different gaps in the parallel-plate geometry. The measurement was done to check whether the slip condition was negligible during the LAOS test.

2.6 Interfacial shear rheology

The rheometer, which was used for the rheological studies on foams, was also used for the interfacial shear rheological measurements. An interfacial rheology system was attached to the rheometer. This system consisted of a biconical disc (diameter = 68.28 mm, cone angle = 5°) and a measuring cell (diameter = 80 mm, height = 90 mm).[11] During all measurements, the temperature was kept constant at 298 K by using a Peltier device. First, the measuring cell was half-filled with the dispersion of the silica nanoparticles in the aqueous HTAB solution, and then left for 15 min to ensure that the surfactant-laden particles formed a film at the air–water interface. Next, the biconical disc was slowly lowered up to its positioned height, which was calculated from the point of contact and the geometry of bicone. Complete contact of the tip of the bicone with the interface was ensured by measuring the normal force. Thereafter, interfacial shear

viscosity (η_s) was measured as a function of shear rate, which was varied from 0.01 to 10 s^{-1}. At low shear rates, it was assumed that the interfacial flow is decoupled from the bulk phase flow. This is because of the high Boussinesq number (Bo), which is defined as the ratio of surface viscosity and sub-phase viscosity. At a higher shear rate, however, the Bo becomes less than 1, and hence, the bulk flow influences the interfacial flow. Therefore, we did not perform experiments above 10 s^{-1} shear rate. Interfacial shear viscosity and interfacial shear viscoelasticity were measured in the rotation and oscillation modes, respectively. To understand the viscoelastic behavior of the interface, amplitude sweep and frequency sweep experiments were performed. In the amplitude sweep, interfacial dynamic moduli (i.e. storage modulus, G_S' and loss modulus, G_S'') were measured as a function of strain, which was varied from 0.01 to 100% at the constant frequency of 1 rad s^{-1}. In the frequency sweep, G_S' and G_S'' were measured by varying the angular frequency from 0.01 to 100 rad s^{-1}, keeping the amplitude constant at 0.5%. The viscoelastic measurements were performed in the linear range, which can be checked from the amplitude sweep experiment, and therefore it was ensured that the microstructure of the film was not destroyed. However, at high frequency, the data points were less clear due to the effect of perturbation in the sub-phase. Therefore, the frequency sweep at the air–water interface was performed at a low frequency (i.e. 1 rad s^{-1}).

In addition to the linear viscoelastic behavior at the air–water interface, its nonlinear viscoelastic behavior was also studied by depicting the elastic and viscous Lissajous–Bowditch curves at five strain amplitudes (i.e. 1, 6.4, 10, 21, and 45%) and two angular frequencies (i.e. 0.1 and 1 rad s^{-1}). A low value of interfacial shear stress and deformation was achieved by using an electronically-commutated motor in a direct strain

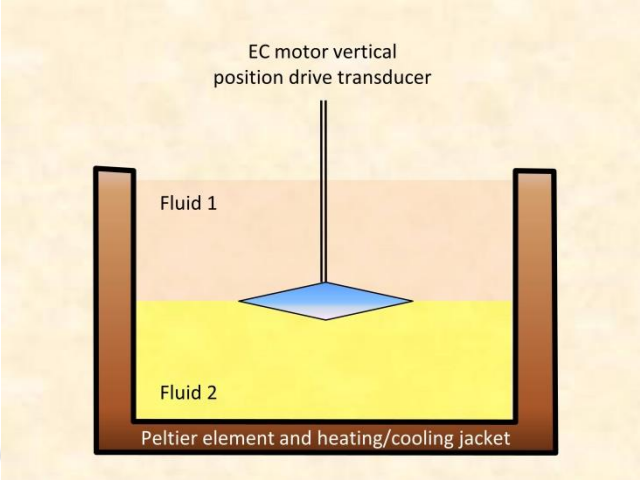

Figure 2.3 Schematic representation of the bicone geometry for interfacial rheology measurement.

oscillation mode.[12] The rheometer had a sensitivity of detecting 0.02 μN m torque with 0.001 μN m resolution. The moment of inertia of the disc was 0.02379 mN m s^{-2}. The smallest measurable surface viscosity was ~10^{-5} Pa s m.

2.7 Thickness and microstructure analysis at interfaces

The thickness of the film formed by surfactant-laden particles at the air–water interface was measured by an ellipsometer [manufacturer: Accurion (Germany), model: Nanofilm]. The microstructure of the film was visualized by using a Brewster angle microscope (BAM), which was equipped with the ellipsometer. This consisted of a laser, a polarizer, a compensator, an analyzer, and a detector (Figure 2.4), which were mounted on an accurate rotatable goniometer. A beam of unpolarized light was allowed to pass through the polarizer followed by the compensator. The azimuthal angle of the polarizer and the compensator was set in such a way that after reflecting from the interface, a linearly polarized light could be obtained, which passed through the analyzer. The laser

produced a monochromatic light of 658 nm wavelength. This light was allowed to fall on the air–water interface with an angle of incidence of 53.1°. The ellipsometer measured the change in polarization due to the reflection from the interface. The difference in polarization was measured by the ellipticity (ρ), which is the ratio of the Fresnel reflection coefficients for the p-polarized and the s-polarized lights. The basic equation of ellipsometry is

$$\rho = \tan\psi e^{i\Delta} \tag{2.1}$$

where ψ (amplitude ratio) is the ratio of amplitudes of reflection coefficients for p- and s-polarized light, and Δ (phase difference) is the corresponding phase difference. By measuring ψ and Δ, the refractive index and the thickness of the interface can be determined.[13] The BAM images were recorded with an objective of 10× magnification, and their dimension was 352 µm × 452 µm. To analyze the air–water interface, 50 cm^3

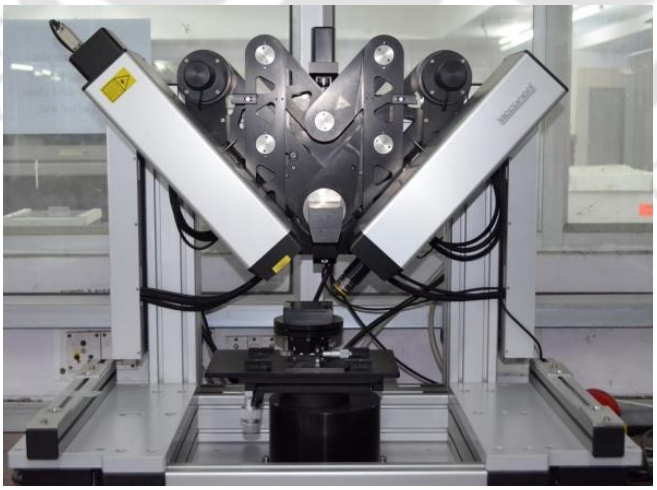

Figure 2.4 Photograph of the ellipsometer.

dispersion was poured into a circular Teflon trough. The trough had a surface area 63 cm^2 and its depth was 2 mm.

Although the ellipsometer is a sophisticated equipment for quantitative characterization of the film at the air–water interface, the measurement of film thickness by this method is complicated. This is because the film (or the monolayer) is transparent, its thickness is small (usually less than 10 nm), and the sub-phase liquid has a low refractive index.[14] Additionally, capillary waves make the film texture essentially rough.[15] Therefore, only changes in Δ are observed, and ψ remains approximately constant. ψ is a sensitive parameter to the optical properties of the film at the air–water interface. Hence, Δ alone is not sufficient to measure the thickness accurately.[16] Several approaches have been described to accurately measure the film thickness at the air–water interface.[17-19] In one approach (known as the *Drude approximation*), the adequate value of the refractive index is assumed to be fixed and the thickness is determined.[20] In another approach, the measurement is performed at the Brewster angle (θ_B). For air–water interface, θ_B is 0.927 rad. It is the angle of incidence at which the reflectance of the p-polarized light is very low and the image contrast is at its maximum. Therefore, at this angle, morphology of the film at the air–water interface can be observed.[21] The interfaces were also analyzed by measuring the surface pressure. The solution was poured into a Langmuir–Blodgett trough [manufacturer: Biolin Scientific (Finland), model: KSV NIMA] made of Teflon. It had two barriers and a platinum–iridium Wilhelmy plate. The barriers were used to compress the monolayer with a speed of 10 mm min^{-1}. The surface

(a)

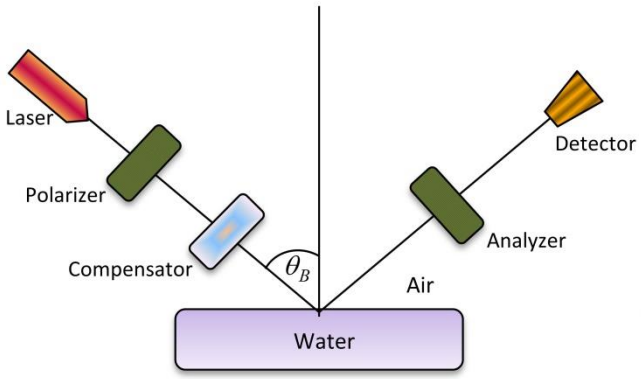

(b)

Figure 2.5 (a) Schematic of ellipsometry and (b) a dispersion containing surfactant-laden particles, which is used to capture the microstructure at the air–water interfaces by BAM.

pressure–area isotherm was measured by using the Wilhelmy plate. Ensuring that the monolayer was formed, and there was no turbulence on the surface, the measurements were made 30 min after pouring the sample. The monolayer was composed of surfactant and surfactant-laden nanoparticles, which moved to the air–water interface from the solution phase. This monolayer was further deposited on a glass substrate by using the Langmuir–Blodgett technique. In this technique, the substrate was dipped across the film

at 90^{o} with a speed 10 mm min^{-1}, and then it was taken out with the same speed. The substrate was dried at the room temperature. Thereafter, the substrate was used to capture the microstructure at the air–water interface by using atomic force microscope (AFM) [manufacturer: Agilent (USA), model: 5500] and transmission electron microscope (TEM) [manufacturer: JEOL (Japan), model: JEM 2100].

Nomenclature

Bo	Boussinesq number
G_S'	interfacial shear storage modulus, Pa m
G_S''	interfacial shear loss modulus, Pa m

Greek letters

γ_0	strain amplitude
Δ	phase difference, rad
η_s	interfacial shear viscosity, Pa s m
θ_B	Brewster angle, rad
ρ	ellipticity
ψ	amplitude ratio
ω	angular frequency, rad s^{-1}

Abbreviations

AFM	atomic force microscope
BAM	Brewster angle microscope
CMC	critical micelle concentration

DLS	dynamic light scattering
HTAB	hexadecyltrymethylammonium bromide
LAOS	large amplitude oscillatory shear
TEM	transmission electron microscope

References

(1) Vishal, B.; Ghosh, P. Foaming in Aqueous Solutions of Hexadecyltrimethylammonium Bromide and Silica Nanoparticles: Measurement and Analysis of Rheological and Interfacial Properties. *J. Dispersion Sci. Technol.* **2018,** *39*, 62–70.

(2) Dimov, N. K.; Kolev, V. L.; Kralchevsky, P. A.; Lyutov, L. G.; Broze, G.; Mehreteab, A. Adsorption of Ionic Surfactants on Solid Particles Determined by Zeta-potential Measurements: Competitive Binding of Counterions. *J. Colloid Interface Sci.* **2002,** *256*, 23–32.

(3) Ghosh, P.; Banik, M. Effects of Salts Containing Mono-, Di-, and Trivalent Ions on Electrical and Rheological Properties of Oil-water Interface in Presence of Cationic Surfactant: Importance in the Stability of Oil-in-water Emulsions. *J. Dispersion Sci. Technol.* **2014,** *35*, 471–481.

(4) Lexis, M.; Willenbacher, N. Yield Stress and Elasticity of Aqueous Foams from Protein and Surfactant Solutions – the Role of Continuous Phase Viscosity and Interfacial Properties. *Colloids Surf., A* **2014,** *459*, 177–185.

(5) Ewoldt, R. H.; McKinley, G. H. On Secondary Loops in Laos Via Self-intersection of Lissajous-Bowditch Curves. *Rheol. Acta* **2010,** *49*, 213–219.

(6) Pipkin, A. C. *Lectures on Viscoelasticity Theory*; Springer: New York, 1972.

(7) Mooney, M. Explicit Formulas for Slip and Fluidity. *J. Rheol.* **1931,** *210*, 210–222.

(8) Habibi, M.; Dinkgreve, M.; Paredes, J.; Denn, M. M.; Bonn, D. Normal Stress Measurement in Foams and Emulsions in the Presence of Slip. *J. Non-Newtonian Fluid Mech.* **2016,** *238,* 33–43.

(9) Graham, M. D. Wall Slip and the Nonlinear Dynamics of Large Amplitude Oscillatory Shear Flows. *J. Rheol*. **1995,** *39,* 697–712.

(10) Giacomin, A. J.; Gilbert, P. H.; Merger, D.; Wilhelm, M. Large Amplitude Oscillatory Shear: Comparing Parallel-disk with Cone-plate Flow. *Rheol. Acta* **2015,** *54,* 263–285.

(11) Erni, P.; Fischer, P.; Windhab, E. J.; Kusnezov, V.; Stettin, H.; Laüger, J. Stress- and Strain-controlled Measurements of Interfacial Shear Viscosity and Viscoelasticity at Liquid/Liquid and Gas/Liquid Interfaces. *Rev. Sci. Instrum.* **2003,** *74,* 4916–4924.

(12) Laüger, J.; Wollny, K.; Huck, S. Direct Strain Oscillation: A New Oscillatory Method Enabling Measurements at Very Small Shear Stresses and Strains. *Rheol. Acta* **2002,** *41,* 356–361.

(13) Azzam, R. M. A.; Bashara, N. M. *Ellipsometry and Polarized Light*; Elsevier: Amsterdam, 1987.

(14) Muth, M.; Schmid, R. P.; Schnitzlein, K. Ellipsometric Study of Molecular Orientations of Thermomyces Lanuginosus Lipase at the Air–Water Interface by Simultaneous Determination of Refractive Index and Thickness. *Colloids Surf., B* **2016,** *140,* 60–66.

(15) de Mul, M. N. G.; Mann, J. A. Determination of the Thickness and Optical Properties of a Langmuir Film from the Domain Morphology by Brewster Angle Microscopy. *Langmuir* **1998,** *14,* 2455–2466.

(16) McCrackin, F. L.; Passaglia, E.; Stromberg, R. R.; Steinberg, H. L. Measurement of the Thickness and Refractive Index of Very Thin Films and the Optical Properties of Surfaces by Ellipsometry. *J. Res. Natl. Bur. Stand. A* **2001,** *106,* 589–603.

(17) Stocco, A.; Carriere, D.; Cottat, M.; Langevin, D. Interfacial Behavior of Catanionic Surfactants. *Langmuir* **2010,** *26,* 10663–10669.

(18) Arteta, M. Y.; Campbell, R. A.; Watkins, E. B.; Obiols-Rabasa, M.; Schillen, K.; Nylander, T. Interactions of Small Dendrimers with Sodium Dodecyl Sulfate at the Air–Water Interface. *J. Phys. Chem. B* **2014,** *118,* 11835–11848.

(19) Kawaguchi, M.; Tohyama, M.; Takahashi, A. Ellipsometric Study of Polymer Monolyers Spread at the Air–Water Interface 2. Adsorbed Amount of Polymers. *Langmuir* **1988,** *4*, 411–413.

(20) Ducharme, D.; Tessier, A.; Russev, S. C. Simultaneous Thickness and Refractive Index Determination of Monolayers Deposited on an Aqueous Subphase by Null Ellipsometry. *Langmuir* **2001,** *17,* 7529–7534.

(21) Honig, D.; Mobius, D. Direct Visualization of Monolayers at the Air–Water Interface by Brewster Angle Microscopy. *J. Phys. Chem.* **1991,** *95,* 4590–4592.

Chapter 3

Foaming in Aqueous Solutions of Hexadecyltrimethylammonium Bromide and Silica Nanoparticles: Measurement and Analysis of Rheological and Interfacial Properties

3.1 Introduction

Aqueous foams are composed of gas bubbles dispersed in water. They are considered as soft complex fluids and amorphous materials.[1] Foams are widely used in cosmetic items, food products, cleaning agents, and pharmaceuticals. Foams are also extensively encountered in flotation, water treatment, and enhanced oil recovery.[2] Foams are thermodynamically unstable, and therefore their kinetic stability is of interest.[3] Generally, foam stability is enhanced by using surfactants and particles. Surfactant molecules adsorb at the air–water interface and lower the surface tension. They also suppress film rupture, thereby preventing the coalescence of bubbles. In addition, they reduce gas diffusion between the bubbles, which reduces coarsening.[4,5] On the other hand, particles at the bubble surface provide a strong viscoelastic film and reduce the film drainage.[6] Additionally, they create a steric barrier, which slows down the film rupture.[7] When a mixture of surfactant and particles is used, a synergetic effect can be observed, and consequently foams are stable for a significantly longer time.[8-10] The synergetic effect arises due to the modification of the surface of the particles by the adsorption of oppositely-charged surfactant molecules.[11,12] The study of foams stabilized by surfactant-laden particles is important in industrial products. It also provides a prototype for the fundamental understanding of soft complex materials.

Foam stability can be characterized by studying coalescence, coarsening, and drainage.[13] The size and morphology of bubbles and the liquid fraction play important roles in foam stability. The concentrations of surfactants, particles, and

other ingredients have a tremendous effect on foam stability.[14] In addition to these mechanisms, macroscopic properties of foams are also important.

Foam rheology deals with the study of macroscopic properties associated with the foam. Foams sometimes show viscoelastic behavior and possess yield stress.[15] At low deformation, foam behaves like an elastic solid, whereas at high shear rate, it shows viscous behavior.[16,17] Therefore, a wide variety of rheological behavior can be observed in foams.

The presence of particles at the air–water interface can be characterized by hydrophilicity (or wettability) of the particles. The wettability of the particles can be altered by adsorption of oppositely-charged surfactant molecules onto the particle surface. Santini et al.[18] have studied the interaction of silica nanoparticles with a cationic surfactant (CTAB). They have shown that positively-charged surfactant molecules adsorbed onto the surface of the negatively-charged particles due to electrostatic attraction. The hydrophilicity of the particles decreased with increasing surfactant concentration. This promoted irreversible transfer of surfactant-laden particles to the air–water interface from the bulk phase.

Recently, many studies have been performed on the interaction of surfactant-laden particles at the air–water interface.[19,20] The surfactant molecules control the adsorption of surfactant-modified particles at the interface. Arriaga et al.[10] have shown the contact angle (or wettability) of surfactant-coated particles at the air–water interface by applying an approach suggested by Clint and Taylor.[21]

The electrostatic and hydrophobic interactions play a significant role in the adsorption of surfactant-laden particles at the air–water interface.[22]

Rheology at the air–water interface gives an idea about the morphology of the particles at the interface. A detailed review of interfacial shear rheology is presented elsewhere.[23,24] Recently, interfacial shear rheology at the air–water interface has been studied extensively.[25-28] Zang et al.[29] have studied shear viscoelastic behavior at the air–water interface. They found that the viscoelastic moduli depend on the hydrophilicity of the particles. However, no such behavior has been found in the corresponding pure system.[30] Application of shear on the interface can shed light on the interaction between the adsorbed molecules. In addition, mechanical behavior of the air–water interface helps to analyze foams containing a large interfacial area. Subsequently, a correlation can be attempted between interfacial shear rheology and foam rheology.[31]

In the present work, we have studied the rheological and morphological properties of hexadecyltrimethylammonium bromide (HTAB) and silica nanoparticles at the air–water interface and in the bulk phase. It was found that a viscoelastic monolayer formed at the air–water interface. We have studied the effect of HTAB on the stability of foams in the presence of the nanoparticles. The rheological behavior of the foams was analyzed. The interaction between the nanoparticles and surfactant at the air–water interface was investigated. The size distribution and the charge of the particles were measured. From these experiments, our key finding is that the nanoparticles were found at the air–water

interface when the concentration of surfactant was below the critical micelle concentration (CMC), and consequently, the foams were more stable under this condition. Finally, a mechanism has been proposed to elucidate the adsorption of surfactant-laden particles from the aqueous phase to the air–water interface.

3.2 Results and discussion

3.2.1 Foam stability

Foams could not be formed with the nanoparticles alone. However, foams were readily formed and stabilized in the presence of HTAB and the nanoparticles. The silica nanoparticles were hydrophilic in nature. Their hydrophilicity was altered by HTAB, which enabled them to act as a foam stabilizer. Foam stability was expressed in terms of foam volume. The variation of foam volume with time is shown in Figure 3.1. This figure shows the stability of foam samples at three different concentrations (i.e., 0.1, 1, and 10 mol m^{-3}) of HTAB at different times. In all samples, the concentration of silica particles was fixed (i.e., 0.5 wt %). The concentration of HTAB had a significant effect on foam stability. Foams were more stable at the low concentrations of HTAB. However, the foamability was moderate (i.e., ~300 cm^3). With increasing HTAB concentration, foam stability decreased. For example, at 1 mol m^{-3} HTAB concentration, the foam was stable for more than 24 h, whereas, the foam was stable only for about 5 h at 10 mol m^{-3} HTAB. This is due to the drainage and coarsening of the bubbles with time.[32] This may also be due to the spherical shape of the bubbles (i.e., *kugelschaum*) at

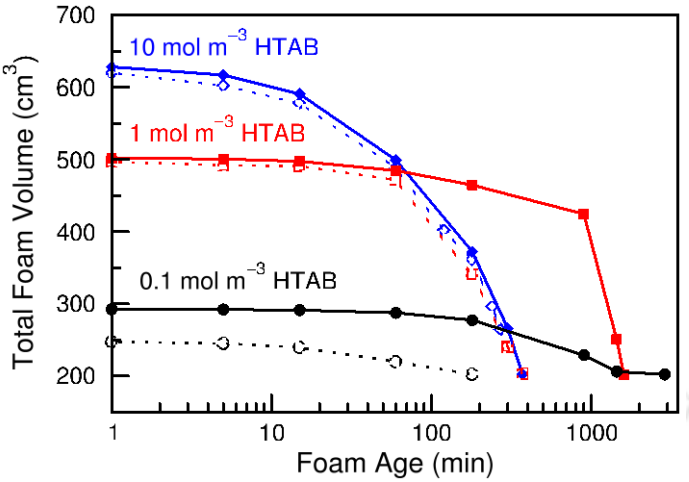

Figure 3.1 Foam stability in the presence of silica nanoparticles (0.5 wt %) and HTAB: variation of foam volume with time and the effect of silica nanoparticles on the stability of foam. Filled symbols represent the foam with particles, and the empty symbols represent the foam without particles. Circles: 0.1 mol m^{-3}, squares: 1 mol m^{-3}, and diamonds: 10 mol m^{-3}.

low surfactant concentration, as shown in Figure 3.2a. Some amount of water was entrapped in the wet foam. In other words, complete drainage of the foam did not occur. However, this kind of behavior was not observed in foams having high HTAB concentrations. This is because of the polygonal cells present in these foams (i.e., *polyederscahum*), as shown in Figure 3.2b,c. These foams were well-drained and dry. The precipitate of the particles can be observed at the bottom after a sufficiently long time. This was noticed when the concentration of surfactant was low. However, at high surfactant concentration, surfactant-laden particles formed a more stable dispersion, which is corroborated by the zeta potential and size

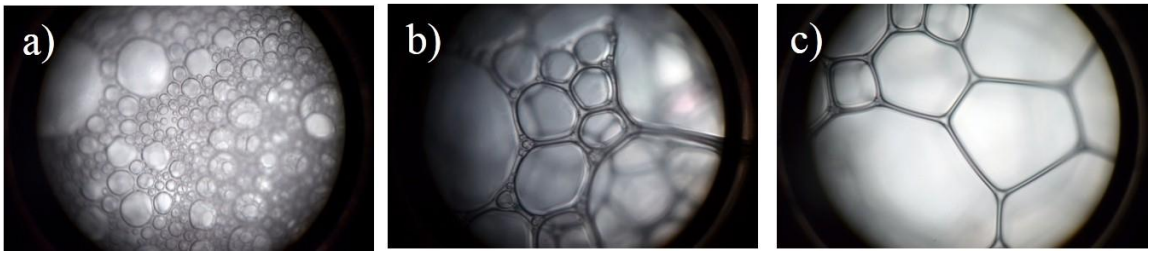

Figure 3.2 Optical micrographs of foams stabilized by silica nanoparticles (0.5 wt %) and HTAB. Images were taken 10 min after the preparation of foam. HTAB concentrations: (a) 0.1 mol m^{-3}, (b) 1 mol m^{-3}, and (c) 10 mol m^{-3}.

distribution measurements. Therefore, no precipitate was observed at 10 mol m^{-3} HTAB concentration.

The silica nanoparticles were capable of changing the life-span of the foams, as shown in Figure 3.1 (dashed line). It was observed that these particles had a strong effect on foam aging, especially when the concentration of HTAB was below the CMC (e.g., 0.1 mol m^{-3}). Not only the life time, but also the volume of foam was enhanced. Foam was stable for less than 3 h without the particles. However, after adding the particles, the age of the foam was enhanced to a few days. This indicates that the silica nanoparticles adsorbed in the foam lamella at low HTAB concentration, and this created a stable film, which increased the stability of foam (see Section 3.3). However, at high HTAB concentration, the particles remained in the Plateau border, and they could not form a stable film.

3.2.2 Foam rheology

Rheological measurement is an important technique for characterizing foam stability at the macroscopic level. In Figure 3.3a, viscosity of foams is shown as a

function of shear rate at three HTAB concentrations, keeping the concentration of the silica nanoparticles fixed. It is clearly observed that the viscosity decreased with increasing HTAB concentration. A sharp fall in viscosity was observed at the lower shear rate when the concentration of HTAB was low. The drastic fall in viscosity at the low shear rate is an indirect indication of the presence of yield stress associated with the foam.[33] However, this kind of behavior was not noticed at the high HTAB concentration (i.e., 10 mol m^{-3}). Foams made of low HTAB concentrations did not flow at the low shear stress, as shown in Figure 3.3b. However, at high shear stress it flowed. The shear stress at which foam starts to flow is called *yield stress*. Figure 3.3b indicates that the yield stress decreased with increasing HTAB concentration. Foam made of 10 mol m^{-3} HTAB did not show a significant yield stress. On the other hand, foam made of 0.1 mol m^{-3} HTAB showed a significant yield stress (~27 Pa), which indicates an elastic behavior. This elastic behavior was studied by measuring the shear strain as a function of time, as shown in Figure 3.3c. Constant shear stresses below the yield stress (i.e., 5, 10, and 20 Pa) were applied to the foam for a certain time period (i.e., 300 s). The corresponding deformations in terms of shear strain were measured as a function of time. At 300 s, until the creep time expired, the shear stresses discontinued to zero. This is known as *creep–recovery* test. From Figure 3.3c, it is clear that the deformation is proportional to shear stress. Consequently, it is apparent that the foam made of silica nanoparticles in the presence of 0.1 mol m^{-3} HTAB possessed elastic behavior.

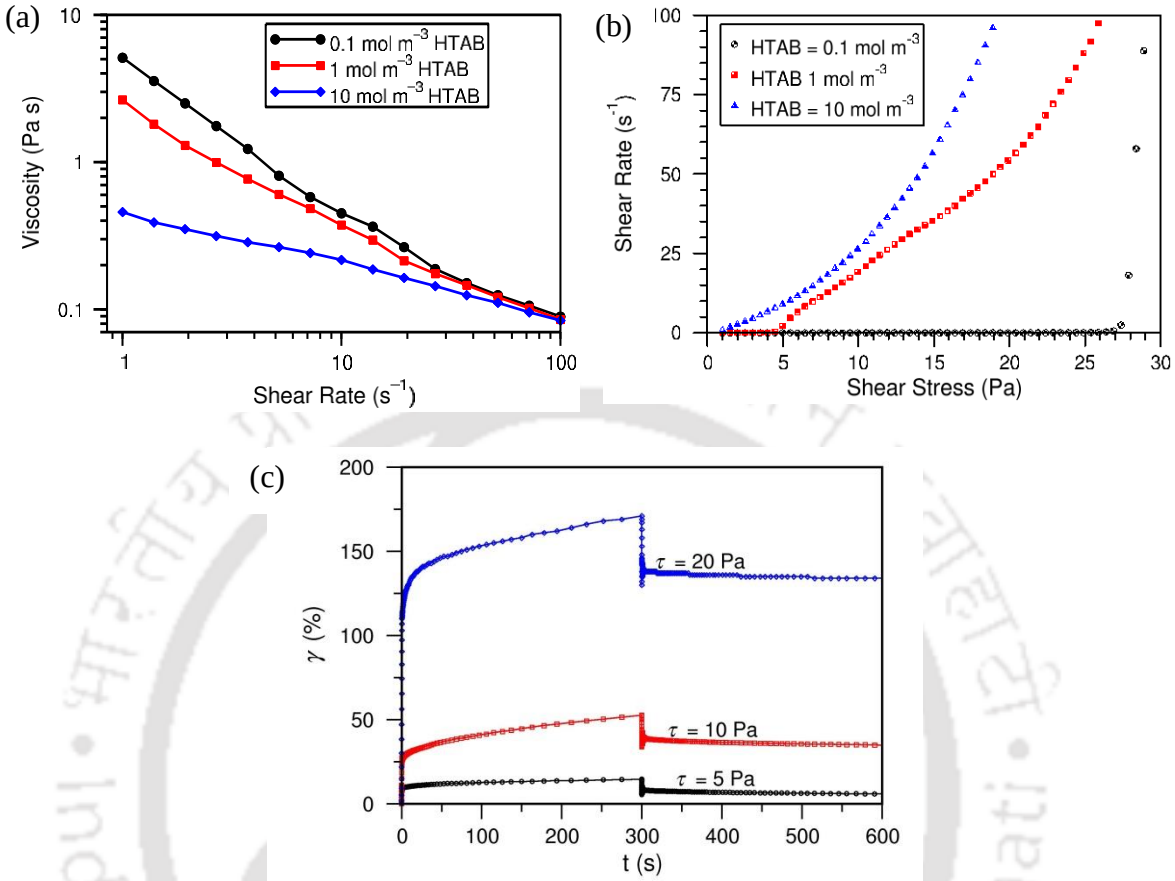

Figure 3.3 Variation of (a) viscosity of foams with shear rate, (b) shear rate with shear stress applied to the foams, and (c) shear strain applied to the foams with time. The foams were subjected to a constant shear stress for 300 s, and then the applied stress was set to zero for another 300 s. The experiments were done at three HTAB concentrations at a fixed concentration (i.e., 0.5 wt %) of silica nanoparticles.

The viscoelastic behavior of the foams was measured by amplitude and frequency sweep experiments. These results are shown in Figure 3.4. It is observed that both G' and G'' strongly depend on the HTAB concentration. In particular, a high value of G' was observed at 0.1 mol m^{-3} HTAB, where the foam displayed a highly elastic behavior. It is also seen from Figures 3.4a,b that G' decreased and

G'' increased at strains higher than 1%, which indicates the nonlinear viscoelastic response of the foam. In this work, we have restricted our study to the linear viscoelastic behavior. This behavior was achieved by small amplitude oscillatory shear experiments,[34] as shown in Figures 3.4c,d. At low HTAB concentration (i.e., 0.1 mol m^{-3}), G' was independent of frequency (Figure 3.4c), and G'' initially remained constant but then changed with increasing frequency (Figure 3.4d). In addition, G' was roughly one order of magnitude higher than G''. These characteristics typically reflect the gel-like behavior of foam.[35] On the other hand, both G' and G'' decreased with increasing HTAB concentration, which indicates a reduction in their viscoelastic behavior. At high HTAB concentration (i.e., 10 mol m^{-3}), G' was larger than G'' at low frequency, which shows that the elastic behavior of foam was dominant. A crossover of G' and G'' was observed at a certain frequency. Beyond this frequency, the foam predominantly showed viscous behavior. However, the crossover frequency was not observed for foams prepared at low HTAB concentrations, due to their gel-like behavior. Foams made of particles and 0.1 mol m^{-3} HTAB showed $G' > G''$ for the entire range of strain and frequency, indicating mainly elastic behavior. Additionally, the rheological characteristics of foam depend on the bubble size as well as the liquid fraction. The less stable foams had bigger bubbles (Figure 3.2b), and thus they showed less values of G' and G''.

In spite of being composed of fluids only, aqueous foams can display elastic behavior. Dry foam can be viewed as a structure of polygonal bubbles, in the

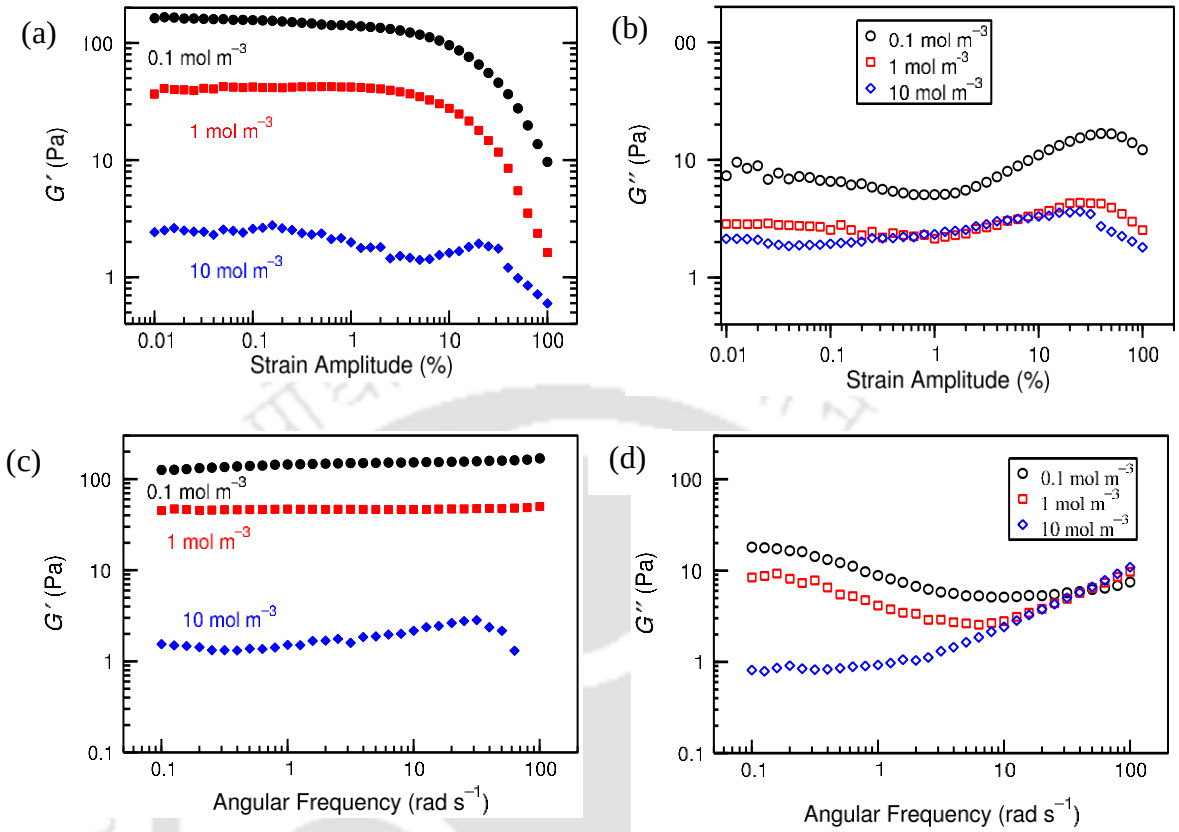

Figure 3.4 Amplitude sweep experiments on foams at the constant frequency of 1 rad s^{-1}: (a) storage modulus (G') and (b) loss modulus (G''). Frequency sweep experiments on foams at the constant strain amplitude of 0.5%: (c) storage modulus (G') and (d) loss modulus (G'').

absence of stress.[36] When a small stress is applied to such foams, their surface energy increases, resulting from their geometrical change. The additional surface energy is stored in the interfaces, which results into the elastic behavior of the foams. At a particular stress (i.e., the yield stress), the length of a few Plateau borders shrinks to zero, and consequently, violates Plateau's rule. With further increase in shear stress, a topological rearrangement is induced, and a new

equilibrium structure is created.[37] Before the yield stress, foam predominantly shows solid-like behavior, whereas, liquid-like behavior dominates beyond the yield stress.

The rheological behavior of wet foams is similar to that of the concentrated emulsions.[38,39] A high stress is required to deform the wet foams stabilized by surfactant-laden particles. This is due to the presence of highly elastic interfaces. When a small deformation is made to the spherical bubble, its surface energy increases. It elastically regains its initial configuration if the stress is relaxed to zero. The energy scale that controls the deformation is given by the Young–Laplace equation.[40] However, at higher deformations, spherical bubbles might be broken into smaller ones under the influence of a high shear stress, and they were aligned in the direction of flow. Therefore, at high strain, wet foams showed liquid-like behavior.

3.2.3 Interfacial shear rheology

The variation of interfacial shear viscosity (η_s) of the adsorbed film at the air–water interface with shear rate is shown in Figure 3.5a. It is observed that η_s significantly decreased with increasing HTAB concentration from 0.1 to 10 mol m^{-3}. This indicates that a strong film was formed by the adsorption of the surfactant-laden particles at the air–water interface at low HTAB concentrations. Moreover, the interface showed a shear-thinning behavior as η_s decreased with increasing shear rate. The shear-thinning behavior was due to the gradual

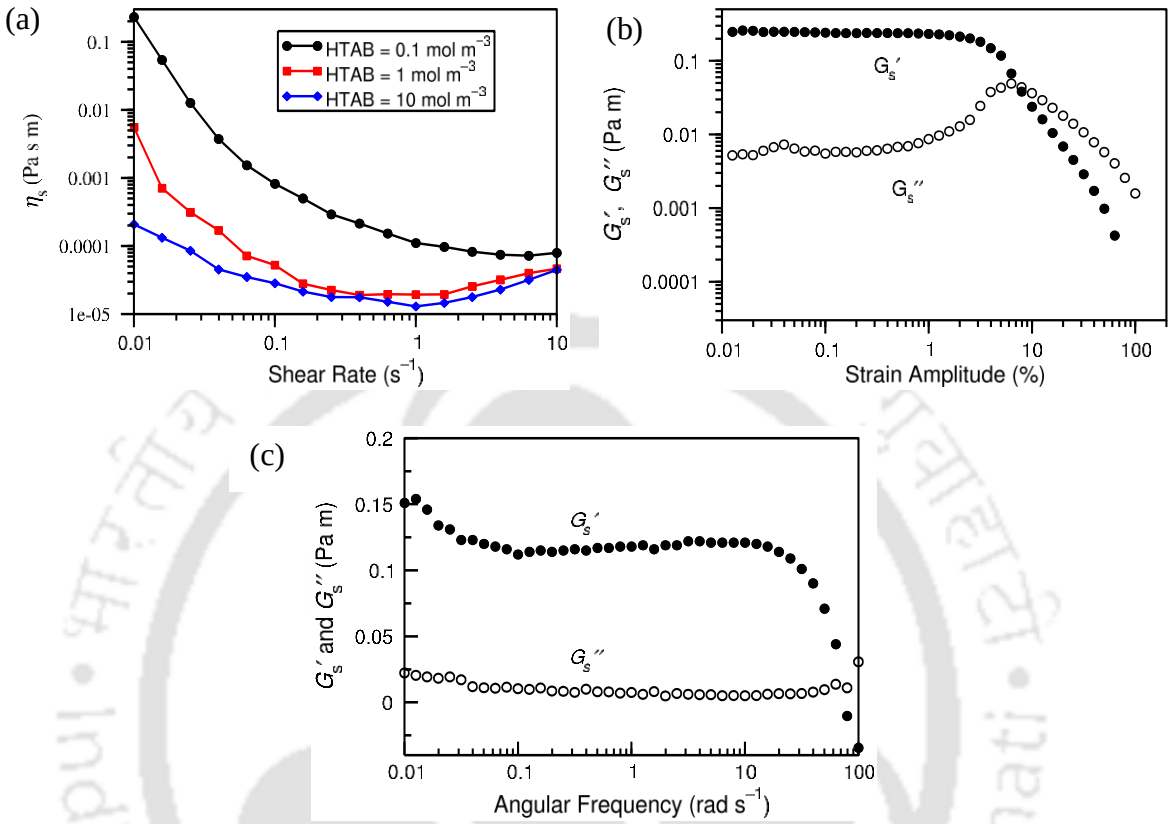

Figure 3.5 (a) Variation of interfacial shear viscosity (η_s) of the adsorbed film at the air–water interface with shear rate. The film was formed by the adsorption of silica nanoparticles in the presence of HTAB; (b) variation of interfacial dynamic moduli (i.e., G_s' and G_s'') of the adsorbed film with increasing strain amplitude. The experiment was done at a constant frequency of 1 rad s^{-1}; (c) variation of G_s' and G_s'' of the adsorbed film at the air–water interface with increasing frequency. The experiment was done at the constant amplitude of 0.5%. The dispersion contained 0.5 wt % silica nanoparticles and 0.1 mol m^{-3} HTAB.

deterioration of the interfacial microstructure. At high shear rate, the sub-phase affects the interfacial shear viscosity. Therefore, a little displacement was observed

for the foam with high surfactant concentrations at high rates. To get more insight into the microstructure at the interface, the linear viscoelastic properties of the adsorbed film were measured using small-amplitude oscillatory shear experiments. A significant amount of interfacial shear viscoelasticity was observed only at low surfactant concentration (i.e., 0.1 mol m^{-3} HTAB). At high HTAB concentration, the interfacial viscoelastic behavior was hardly noticeable. Figure 3.5b shows the results of amplitude sweep experiment at the air–water interface. It is observed that the adsorbed film exhibited a linear viscoelastic behavior at lower strain (i.e., up to 1%), and a nonlinear viscoelastic behavior was observed at higher strain. Linear viscoelastic behavior of the adsorbed film of surfactant-laden particles, obtained from the frequency sweep experiments, is shown in Figure 3.5c. It was observed that G_s' was larger than G_s'' and both the moduli were almost independent of the frequency of oscillation. This observation typically reflects the elastic and gel-like behavior of the film.

Based on the investigations performed on bulk foam rheology and interfacial shear rheology, we can correlate these rheological behaviors with foam stability. It was observed that the bulk viscosity of foam decreased with increasing HTAB concentration. In a similar manner, the interfacial shear viscosity decreased with increasing HTAB concentration. In addition, at low HTAB concentration (i.e., 0.1 mol m^{-3}), foams displayed a high yield stress and a gel-like elastic behavior. Similar behavior was observed in interfacial shear rheological experiments as well. These results indicate that the foam was more stable at low HTAB concentration,

exhibited a high yield stress and possessed a gel-like elastic film. Similar results have been reported by Lexis[41] for foams stabilized by proteins.

3.2.4 Zeta potential and particle size measurements

The surface charge of the silica nanoparticles was determined by measuring the zeta potential. In the absence of surfactant, the zeta potential was approximately –25 mV. The zeta potential became positive with increasing HTAB concentrations, as shown in Figure 3.6a. The change in zeta potential from negative to positive was due to the adsorption of positively-charged surfactant (i.e., HTAB) molecules on the surface of the negatively-charged silica nanoparticles. The hydrodynamic diameter of the particles initially increased, reached a maximum, and thereafter decreased as shown in Figure 3.6b. Based on these observations, it can be concluded that the agglomeration of particles took place when the zeta potential was low. At 1 mol m^{-3} HTAB concentration, the particles had almost the same zeta potential as that at 0.01 mol m^{-3} HTAB, albeit of opposite sign. Particles in the presence of 1 mol m^{-3} HTAB showed a high extent of agglomeration, resulting in larger hydrodynamic diameter. Similar results have been reported by Degan et al. [42] for foams stabilized by magnetic nanoparticles. Particles (having the same size) sedimented at 0.1 mol m^{-3} surfactant concentration, but not at 10 mol m^{-3} (Figure 3.6b). This is because of the high surface potential of the particles at 10 mol m^{-3} HTAB, which made the dispersion relatively more stable. Furthermore, the timescale also affected the sedimentation because more time was required to sediment a stable dispersion.

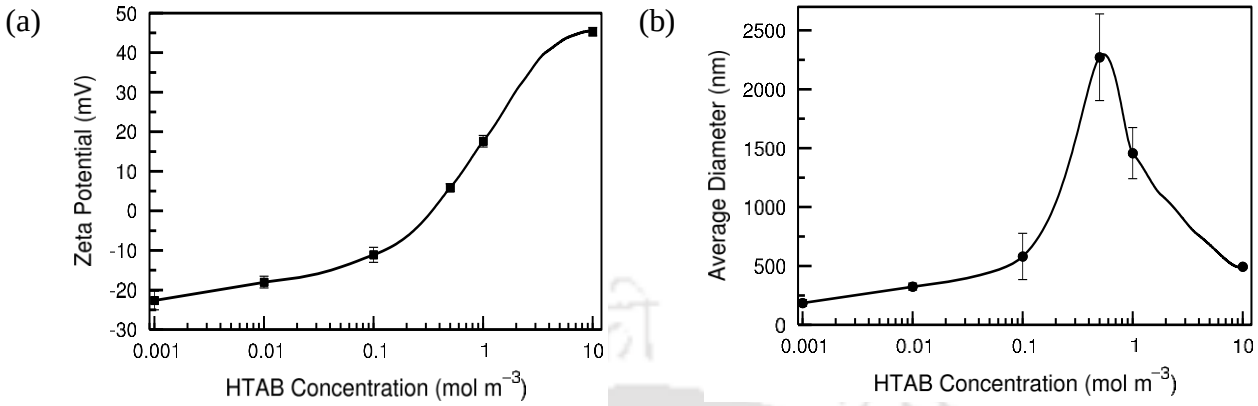

Figure 3.6 Variation of (a) zeta potential at particle surface and (b) average hydrodynamic diameter of silica nanoparticles with HTAB concentration. Concentration of nanoparticles was 0.5 wt %.

3.2.5 Interaction between particle and surfactant at the air–water interface

The silica nanoparticles were hydrophilic in nature. As such, they neither decreased the surface tension of water nor formed a strong film at the air–water interface. However, in the presence of HTAB in the aqueous medium, the hydrophilicity of the particles was changed inasmuch as the surfactant molecules adsorbed at the surface of the particles. The surfactant-laden particles adsorbed at the air–water interface. Consequently, particles in the presence of 0.1 mol m^{-3} HTAB showed a reasonably high viscoelastic film at the air–water interface. In addition, a high surface pressure was observed during the compression of the film in a Langmuir–Blodgett trough, which indicates the agglomeration of the surfactant-laden particles at the air–water interface. The surface pressure isotherm is shown in Figure 3.7. The agglomeration occurred only at low surfactant

concentrations (i.e., below the CMC). However, at high HTAB concentrations (i.e., above the CMC), the particles remained in the sub-phase, and the interface was covered with the surfactant molecules only. Therefore, the presence of the particles was not observed at the air–water interface, and consequently a lower surface pressure was observed. The electrostatic double layer repulsion between the particles increased at high surfactant concentrations, which did not allow the particles to interact with each other. Consequently, a viscoelastic film was not observed at high HTAB concentrations. Therefore, when surfactant was added below the CMC, a Langmuir-type monolayer was formed at the air–water interface due to the adsorption of surfactant-laden particles. On the other hand, at surfactant concentration above the CMC, a Gibbs-type monolayer was formed at the interface due to the adsorption of the surfactant molecules. We have observed that a monolayer having a thickness of a few nanometers was formed from the 0.1 mol m^{-3} HTAB solution, as shown in Figure 3.8a. This is due to the presence of

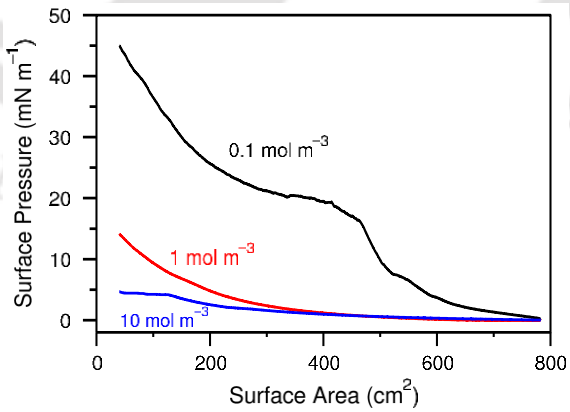

Figure 3.7 Surface pressure–area isotherm at the air–water interface in the presence of HTAB and silica nanoparticles. The experiments were done at three HTAB concentrations at a fixed concentration (i.e., 0.5 wt %) of the silica nanoparticles.

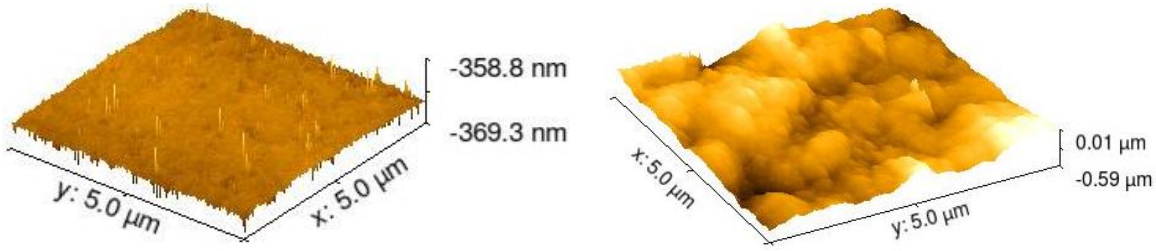

Figure 3.8 Effect of silica nanoparticles on the morphology of the monolayers formed at the air–water interface: (a) 0.1 mol m^{-3} HTAB solution and (b) a mixture of 0.1 mol m^{-3} HTAB and 0.5 wt % silica nanoparticles.

surfactant molecules at the air–water interface. When 0.5 wt % silica nanoparticles were added to this solution, the thickness increased to several micrometers, which was due to the presence of the silica nanoparticles at the interface (Figure 3.8b).

3.3 Conclusions

In this work, a mixture of cationic surfactant (HTAB) and negatively-charged silica nanoparticles was used to stabilize aqueous foams. Our work highlights the mechanism involved in foam stability. At low HTAB concentration (i.e., 0.1 mol m^{-3}), foam was more stable and it was composed of spherical bubbles. It possessed high viscosity, which decreased sharply at low shear rate due to the presence of a high yield stress. In addition, it exhibited a high viscoelastic behavior. However, at high HTAB concentration, both viscosity and viscoelasticity of foams were significantly lower. Similar phenomena were observed at the air–water interface. At the low HTAB concentration, interfacial shear viscosity was relatively high and it decreased with increasing shear rate, which implies the destruction of the

microstructure at the interface. In addition, the interface showed a viscoelastic gel-like behavior. A Langmuir-type film was formed at the air–water interface due to the adsorption of surfactant-laden particles. This was confirmed by the high surface pressure observed during the compression of the monolayer. In contrast, these behaviors were not observed at high HTAB concentrations.

The zeta potential measurements clearly demonstrated that the adsorption of HTAB molecules occurred on the surface of the silica nanoparticles. As a result, the hydrophilicity of the particles decreased and the charge at the surface of the particles became less negative. Eventually, the particles acquired a positive charge with increasing HTAB concentration. Therefore, agglomeration of the particles took place in the bulk phase as well as at the air–water interface when the electric potential on the particles was low. The formation of a Langmuir-type monolayer at the air–water interface took place due to the hydrophobic interaction between the surfactant-laden particles. Therefore, at 0.1 mol m^{-3} HTAB, the interface showed a viscoelastic gel-like behavior, and consequently, the foams were more stable. Nevertheless, at high HTAB concentrations (i.e., above the CMC), the surface was completely occupied by the surfactant molecules and hence, the surfactant laden-particles were accommodated near the sub-phase or in the bulk phase. Therefore, a Gibbs-like monolayer was formed at high HTAB concentrations. This monolayer did not form a viscoelastic film at the air–water interface, and consequently, it was relatively less stable.

References

(1) Blanco, E.; Lam, S.; Smoukov, S. K.; Velikov, K. P.; Khan, S. A.; Velev, O. D. Stability and Viscoelasticity of Magneto-Pickering Foams. *Langmuir* **2013,** *29*, 10019–10027.

(2) Vijayaraghavan, K.; Nikolov, A.; Wasan, D.; Henderson, D. Foamability of Liquid Particle Suspensions: A Modeling Study. *Ind. Eng. Chem. Res.* **2009,** *48*, 8180–8185.

(3) Gonzenbach, U. T.; Studart, A. R.; Tervoort, E.; Gauckler, L. J. Stabilization of Foams with Inorganic Colloidal Particles. *Langmuir* **2006,** *22*, 10983–10988.

(4) Samanta, S.; Ghosh, P. Coalescence of Bubbles and Stability of Foams in Aqueous Solutions of Tween Surfactants. *Chem. Eng. Res. Des.* **2011,** *89*, 2344–2355.

(5) Tcholakova, S.; Mitrinova, Z.; Golemanov, K.; Denkov, N. D.; Vethamuthu, M.; Ananthapadmanabhan, K. P. Control of Ostwald Ripening by using Surfactants with High Surface Modulus. *Langmuir* **2011,** *27*, 14807–14819.

(6) Hunter, T. N.; Pugh, R. J.; Franks, G. V.; Jameson, G. J. The Role of Particles in Stabilising Foams and Emulsions. *Adv. Colloid Interface Sci.* **2008,** *137*, 57–81.

(7) Dickinson, E. Structuring of Colloidal Particles at Interfaces and the Relationship to Food Emulsion and Foam Stability. *J. Colloid Interface Sci.* **2015,** *449*, 38–45.

(8) Binks, B. P. Particles as Surfactants–Similarities and Differences. *Curr. Opin. Colloid Interface Sci.* **2002,** *7*, 21–41.

(9) Carl, A.; Bannuscher, A.; von Klitzing, R. Particle Stabilized Aqueous Foams at Different Length Scales: Synergy between Silica Particles and Alkylamines. *Langmuir* **2015,** *31*, 1615–1622.

(10) Arriaga, L. R.; Drenckhan, W.; Salonen, A.; Rodrigues, J. A.; Iniguez-Palomares, R.; Rio, E.; Langevin, D. On the Long-term Stability of Foams Stabilised by Mixtures of Nano-Particles and Oppositely Charged Short Chain Surfactants. *Soft Matter* **2012,** *8*, 11085–11097.

(11) Binks, B. P.; Johnson, A. J.; Rodrigues, J. A. Inversion of 'Dry Water' to Aqueous Foam on Addition of Surfactant. *Soft Matter* **2010,** *6*, 126–135.

(12) Gonzenbach, U. T.; Studart, A. R.; Tervoort, E.; Gauckler, L. J. Ultrastable Particle-stabilized Foams. *Angew. Chem. Int. Ed.* **2006,** *45,* 3526–3530.

(13) Saint-Jalmes, A.; Langevin, D. Time Evolution of Aqueous Foams: Drainage and Coarsening. *J. Phys.: Condens. Matter* **2002,** *14,* 9397–9412.

(14) Zhang, S. Y.; Lan, Q.; Liu, Q.; Xu, H.; Sun, D. J. Aqueous Foams Stabilized by Laponite and CTAB. *Colloids Surf., A* **2008,** *317,* 406–413.

(15) Marze, S.; Guillermic, R. M.; Saint-Jalmes, A. Oscillatory Rheology of Aqueous Foams: Surfactant, Liquid Fraction, Experimental Protocol and Aging Effects. *Soft Matter* **2009,** *5,* 1937–1946.

(16) Khan, S. A.; Armstrong, R. C. Rheology of Foams: 1. Theory for Dry Foams. *J. Non-Newtonian Fluid Mech.* **1986,** *22,* 1–22.

(17) Cox, S.; Weaire, D.; Glazier, J. A. The Rheology of Two-dimensional Foams. *Rheol. Acta* **2004,** *43,* 442–448.

(18) Santini, E.; Kragel, J.; Ravera, F.; Liggieri, L.; Miller, R. Study of the Monolayer Structure and Wettability Properties of Silica Nanoparticles and CTAB using the Langmuir Trough Technique. *Colloids Surf., A* **2011,** *382,* 186–191.

(19) Maestro, A.; Deshmukh, O. S.; Mugele, F.; Langevin, D. Interfacial Assembly of Surfactant-decorated Nanoparticles: On the Rheological Description of a Colloidal 2D Glass. *Langmuir* **2015,** *31,* 6289–6297.

(20) Maestro, A.; Rio, E.; Drenckhan, W.; Langevin, D.; Salonen, A. Foams Stabilised by Mixtures of Nanoparticles and Oppositely Charged Surfactants: Relationship between Bubble Shrinkage and Foam Coarsening. *Soft Matter* **2014,** *10,* 6975–6983.

(21) Clint, J. H.; Taylor, S. E. Particle Size and Interparticle Forces of Overbased Detergents: A Langmuir Trough Study. *Colloids Surf.* **1992,** *65,* 61–67.

(22) Maestro, A.; Guzman, E.; Santini, E.; Ravera, F.; Liggieri, L.; Ortega, F.; Rubio, R. G. Wettability of Silica Nanoparticle–Surfactant Nanocomposite Interfacial Layers. *Soft Matter* **2012,** *8,* 837–843.

(23) Krägel, J.; Derkatch, S. R. Interfacial Shear Rheology. *Curr. Opin. Colloid Interface Sci.* **2010,** *15,* 246–255.

(24) Miller, R.; Ferri, J. K.; Javadi, A.; Krägel, J.; Mucic, N.; Wüstneck, R. Rheology of Interfacial Layers. *Colloid Polym. Sci.* **2010,** *288,* 937–950.

(25) Madivala, B.; Fransaer, J.; Vermant, J. Self-assembly and Rheology of Ellipsoidal Particles at Interfaces. *Langmuir* **2009,** *25,* 2718–2728.

(26) Erni, P.; Fischer, P.; Windhab, E. J.; Kusnezov, V.; Stettin, H.; Laüger, J. Stress- and Strain-controlled Measurements of Interfacial Shear Viscosity and Viscoelasticity at Liquid/Liquid and Gas/Liquid Interfaces. *Rev. Sci. Instrum.* **2003,** *74,* 4916–4924.

(27) Karbaschi, M.; Lotfi, M.; Krägel, J.; Javadi, A.; Bastani, D.; Miller, R. Rheology of Interfacial Layers. *Curr. Opin. Colloid Interface Sci.* **2014,** *19,* 514–519.

(28) Pradilla, D.; Simon, S.; Sjöblom, J.; Samaniuk, J.; Skrzypiec, M.; Vermant, J. Sorption and Interfacial Rheology Study of Model Asphaltene Compounds. *Langmuir* **2016,** *32,* 2900–2911.

(29) Zang, D.; Langevin, D.; Binks, B. P.; Wei, B. Shearing Particle Monolayers: Strain-rate Frequency Superposition. *Phys. Rev. E.* **2010,** *81,* 011604.

(30) Cicuta, P.; Stancik, E. J.; Fuller, G. G. Shearing or Compressing a Soft Glass in 2D: Time-concentration Superposition. *Phys. Rev. Lett.* **2003,** *90,* 236101.

(31) Edwards, D. A.; Brenner, H.; Wasan, D. T. *Interfacial Transport Processes and Rheology*; Butterworth–Heinemann: Stonheam, MA, 1991.

(32) Saint-Jalmes, A. Physical Chemistry in Foam Drainage and Coarsening. *Soft Matter* **2006,** *2,* 836–849.

(33) Khan, S. A.; Schnepper, C. A.; Armstrong, R. C. Foam Rheology: III. Measurement of Shear Flow Properties. *J. Rheol.* **1988,** *32,* 69–92.

(34) Macosko, C. W. *Rheology: Principles, Measurements, and Applications*; Wiley-VCH: New York, 1994.

(35) Winter, H. H.; Chambon, F. Analysis of Linear Viscoelasticity of a Crosslinking Polymer at the Gel Point. *J. Rheol.* **1986,** *30,* 367–382.

(36) Weaire, D. Kelvin's Foam Structure: A Commentary. *Philos. Mag. Lett.* **2008,** *88,* 91–102.

(37) Höhler, R.; Cohen-Addad, S. Rheology of Liquid Foam. *J. Phys.: Condens. Matter* **2005,** *17,* 1041–1069.

(38) Stamenovic, D. A Model of Foam Elasticity Based upon the Laws of Plateau. *J. Colloid Interface Sci.* **1991,** *145,* 255–259.

(39) Mason, T. G.; Bibette, J.; Weitz, D. A. Yielding and Flow of Monodisperse Emulsions. *J. Colloid Interface Sci.* **1996,** *179,* 439–448.

(40) Reinelt, D. A.; Kraynik, A. M. Simple Shearing Flow of Dry Soap Foams with Tetrahedrally Close-packed Structure. *J. Rheol.* **2000,** *44,* 453–471.

(41) Lexis, M.; Willenbacher, N. Yield Stress and Elasticity of Aqueous Foams from Protein and Surfactant Solutions – The Role of Continuous Phase Viscosity and Interfacial Properties. *Colloids Surf., A* **2014,** *459,* 177–185.

(42) Degan, P.; Wieland, D. C. F.; Leick, S.; Paulus, M.; Rehage, H.; Tolan, M. Effect of Magnetic Nanoparticles on the Surface Rheology of Surfactant Films at the Water Surface. *Soft Matter* **2011,** *7,* 7655–7662.

Chapter 4

The Effect of Silica Nanoparticles on the Stability of Aqueous Foams

4.1 Introduction

Aqueous foams have versatile applications in food products, cosmetics, water treatment, and enhanced oil recovery.[1,2] Foams are composed of thin liquid films, known as *Lamellae*. The foam film consists of two air–water interfaces. Therefore, the stability of foams deeply relies on the stability of the thin liquid films, and consequently on the properties of the air–water interfaces. Nanoparticles, in the presence of a surfactant, create a strong viscoelastic film by adsorbing at the air–water interfaces.[3] Consequently, foams are stable for a longer period.[4,5] The charge on the nanoparticles and the surfactant molecules plays an important role on the particle–surfactant synergy. To illustrate, silica nanoparticles do not show any significant effect in the presence of sodium dodecyl sulfate (SDS) because both have the same charge, and hence they do not attract each other.[6,7] A similar behavior can be observed with non-ionic surfactants.[8] Joshi et al.[9] have found that the non-ionic surfactant acts as an antifoaming agent like non-polar oil and hydrophobic solid particles. However, in the presence of a cationic surfactant, such as hexadecyltrimethylammonium bromide (HTAB), the surfactant molecules adsorb on the surface of the particles and change their properties.[10,11] Surfactant molecules not only modify the surface properties of the particles, but they also help the latter to adsorb at the air–water interface. Liu et al.[12] have studied the effect of alkyl chain length on the interaction between surfactant and particle. Tambe and Sharma[13] have reviewed the effect of particles on the fluid–fluid interfaces. They have reported that particles increase the steric hindrance and reduce the rate of liquid drainage. Recently, Yekeen et al.[14] have comprehensively reviewed the foaming behavior of nanoparticle–surfactant system.

Particles deform the shape of the air–water interface by adsorbing on it. This deformation gives rise to a capillary interaction between the particle and the interface. The capillary interaction determines the position of the particle at the interface. The stability of the particle at the air–water interface can be quantified by the minimum energy (ΔE) required to remove the particle from the interface, which is given by[15-17]

$$\Delta E = \pi R^2 \gamma (1 \pm \cos\theta)^2 \tag{4.1}$$

where R is the radius of the particle, γ is the surface tension, and θ is the contact angle. In other words, the surface energy is reduced by ΔE when a particle adsorbs at the air–water interface. The removal of a hydrophilic particle from the air–water interface to the aqueous and air phases is signified by the negative and positive signs, respectively.

In an air bubble, the pressure difference across the air–water interface is given by the Young–Laplace equation,

$$\Delta P = \frac{2\gamma}{R} \tag{4.2}$$

When two such bubbles approach each other, a thin liquid film forms. The foam is stable as long as the thin liquid film remains stable. The interaction between two bubble surfaces across the thin liquid film has been studied by several workers.[18,19] Gravity and capillary forces are mainly responsible for the film drainage. Based on the studies on the thin liquid films, it has been found that when a film reaches a thickness of ~20 nm, surface forces begin to operate within the film, in addition to the gravity and capillary forces.

Surface forces have a molecular origin, and they are expressed in terms of the disjoining pressure. The net disjoining pressure (Π) between two surfaces is given by the disjoining pressures due to the van der Waals (Π_v) and the electrostatic double layer forces (Π_e).[20-23]

$$\Pi(h) = \Pi_v + \Pi_e \tag{4.3}$$

Equation 4.3 is based on the Derjaguin–Landau–Verwey–Overbeek (DLVO) theory.[24-26] However, in many situations, the classical DLVO theory is insufficient.[27] The non-DLVO forces (e.g. hydration and structural forces) play significant roles when the surfactant head-groups are hydrated and the nanoparticles are present.[28,29] A third term incorporating the disjoining pressure due to these repulsions (Π_s) may be included in Equation 4.3.

As drainage proceeds significantly, the thickness of the thin liquid film reduces and the capillary pressure increases. Ultimately, the thin liquid film is covered with a single layer of particles, and thereafter the plane interface deforms into a meniscus. The maximum capillary pressure $\left(P_c^{\max}\right)$ occurs at the onset of coalescence. It is given by[30,31]

$$P_c^{\max} = p\left(\frac{2\gamma}{R}\right)\cos\theta \tag{4.4}$$

where p is a packing parameter that depends on the concentration and orientation of the particles in the thin liquid film.

Since the foam film consists of two air–water interfaces, its properties depend on the characteristics of these interfaces. There are various ways to characterize the air–water interfaces containing surfactant-laden particles. Interfacial shear rheology is an important tool for understanding the dynamic behavior of these interfaces. Most of the studies on the shear rheology of the air–water interfaces have focused only on the linear viscoelastic regime (i.e. at low deformations).[32-36] However, these interfaces are subjected to large and fast deformations during the foaming process. They often show nonlinear response even at low strains (or strain rates). Therefore, to understand the foaming behavior under deformation, the interfacial rheology should not be limited to small deformations, but should be extended to large deformations. There are several ways to study interfacial shear rheology at large deformations, e.g. by analyzing the storage (G_s') and loss moduli (G_s'') as a function of strain amplitude, which is commonly known as *amplitude sweep experiment*.[37] Recently, Lissajous–Bowditch curves have become very popular for characterizing nonlinear viscoelastic behavior, where the stress responses are plotted against the imposed strain (or strain rate).[38] These are termed as elastic (or viscous) Lissajous–Bowditch curves. This is a geometrical approach, in which the behavior of the air–water interface is characterized by analyzing the shape of these curves. Because of the symmetry of the Lissajous–Bowditch curves, Cho et al.[39] have suggested a method of decomposing the stress response into their elastic and viscous counterparts at large deformation, which was further improved by Yu et al.[40] Due to the involvement of higher harmonic terms, the detailed explanation of the Lissajous–Bowditch curves is not yet fully understood. Only a few works have been carried out on the nonlinear viscoelastic behavior of the air–water interfaces using these curves.[41-44]

However, many works have been conducted on the nonlinear viscoelastic behavior of bulk materials.[45] Such information may be useful for analyzing the air–water interface because interfacial rheology can be considered as the 2D analogue of the classical bulk rheology.

Although the effects of hydrophilicity,[46,47] size,[48,49] shape,[50-52] and concentration of the particles on the stability of thin liquid films have been studied for a long time, the mechanism involved in the stability is still poorly understood. It is well known that the physicochemical properties of the air–water interface play a vital role in the stability of colloidal systems containing bubbles as the dispersed phase.[53] Therefore, in the present work, we have performed an experimental investigation on the effect of silica nanoparticles on the stability of foams in the presence of a cationic surfactant (i.e. HTAB). The foamability and stability of these foams were studied. The stability of foam film depends on its mechanical strength and the properties of the air–water interface (as mentioned earlier), which were studied through foam rheology and interfacial shear rheology, respectively. The nonlinear viscoelastic behavior of the air–water interfaces was analyzed by using the Lissajous–Bowditch curves. Finally, the thickness and the microstructure of the interfaces were measured by ellipsometry and Brewster angle microscopy (BAM).

4.2 Results and discussion

4.2.1 Foam stability and foamability

Foams are usually characterized qualitatively by their stability and foamability.[7] Foam stability refers to the lifetime of a foam in which its volume decreases with time after its

formation, whereas foamability depicts the ability of a surfactant solution to produce foam. Figure 4.1 shows the variation of foam volume with time. The foam volume decreased with time because foams are thermodynamically unstable (or metastable) systems. At an HTAB concentration below the CMC, the stability of foam improved with increasing particle concentration (Figure 4.1a). In the absence of the nanoparticles, foams were stable for a few hours only. However, at sufficiently high particle concentrations, the foams were stable for a few days. Therefore, the enhanced stability is a result of high particle concentration in the foam lamellae and the Plateau borders. The nanoparticles flow along with the liquid and block the nodes (i.e. the intersection of the Plateau borders), which reduces the drainage of liquid from the foam. In addition, high particle concentration can increase the viscosity of the liquid inside the foam. The higher viscosity reduces the foam drainage rate and consequently increases the stability of foam. Therefore, foams were more stable at a higher particle concentration. The silica nanoparticles also showed a significant effect on the foamability when the HTAB concentration was below the CMC. In the absence of the particles, less than 250 cm^3 foam was produced from 200 cm^3 dispersion, whereas in the presence of particles (0.5 wt%), ~290 cm^3 foam was produced.

Contrary to the above observations, we did not find any significant change due to the particles on the foamability as well as foam stability at HTAB concentrations above the CMC. This may be due to the absence of particles at the air–water interface. The interface was completely covered with only the surfactant molecules when the surfactant concentration was above the CMC. Hardly any space was available at the air–water

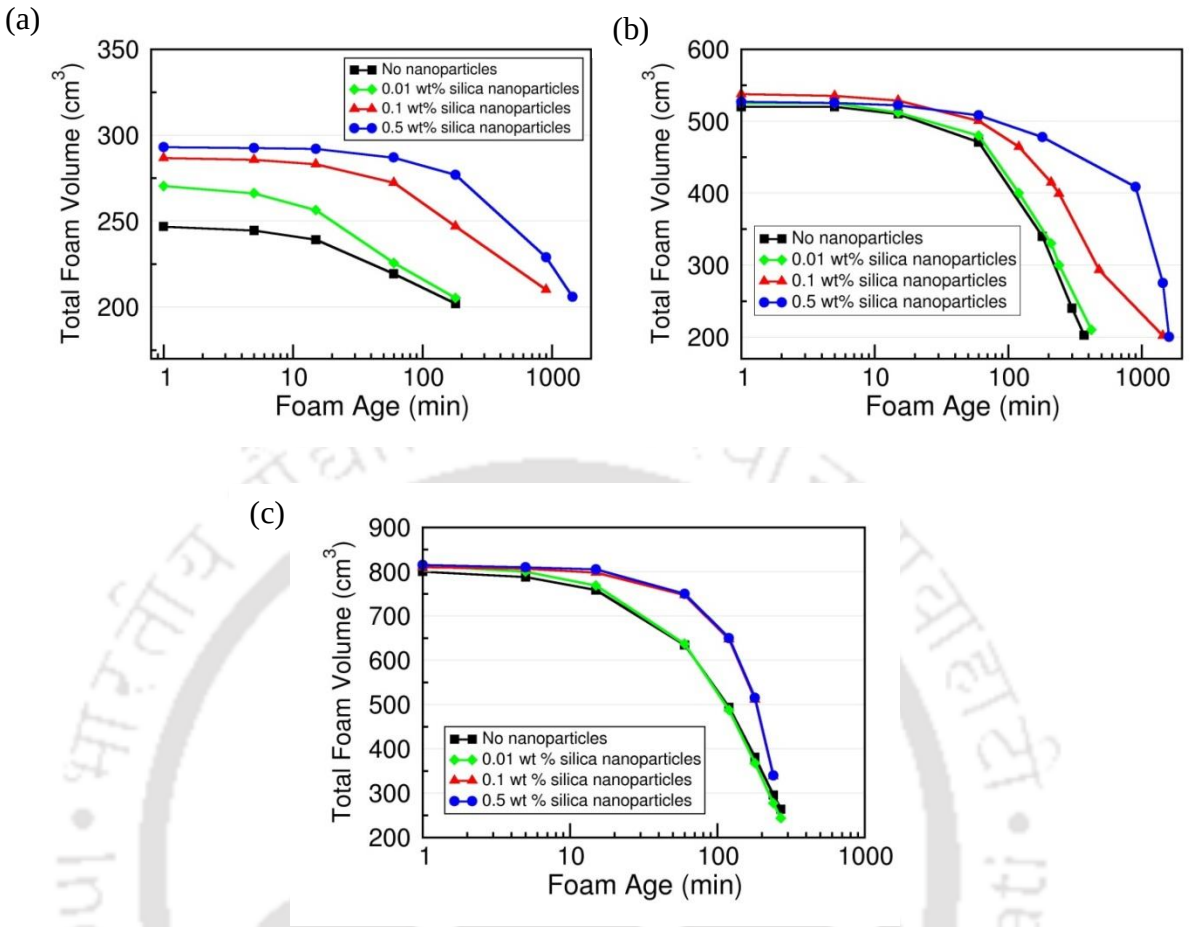

Figure 4.1 The effect of concentration of silica nanoparticles on the foamability and stability of the foams at HTAB concentrations: (a) 0.1 mol m^{-3}, (b) 1 mol m^{-3}, and (c) 10 mol m^{-3}.

interface for the nanoparticles. Therefore, the surfactant-laden nanoparticles remained near the sub-phase or in the bulk phase. However, below the CMC, these nanoparticles were present at the air–water interface because the interface was not fully occupied by the surfactant molecules. The presence of these nanoparticles enhanced the strength of the liquid films, and therefore the foams were more stable. In addition, at a fixed particle concentration, foamability increased with increasing HTAB concentration (see Figure

4.1). In the present work, our primary focus was on the effect of silica nanoparticles in the presence of HTAB.

4.2.2 Foam rheology

The stability of foams depends on the stability of the foam films.[54] In order to study the strength of the foam films, foam rheology was studied in which the foam films were deformed and ruptured by imposing shear stress. Figure 4.2 depicts the effect of silica nanoparticles on the viscosity of foams. These nanoparticles had a significant influence on the viscosity of foams at HTAB concentrations below the CMC (see Figure 4.2a). The viscosity increased with increasing particle concentration. The rise in viscosity with particle concentration indicates that the foam films were stronger and required a higher shear stress to flow. The thin liquid films were stable due to the presence of surfactant-laden particles at the air–water interfaces. Furthermore, the foams showed shear thinning behavior, which is reflected by the decrease in viscosity with increasing shear rate. This behavior shows the realignment of the bubbles and rupture of the foam films.

In the presence of particles, the viscosity was reduced by 10 times when the HTAB concentration was above the CMC. The effect of particles on the viscosity of foams became less pronounced with increasing HTAB concentration. The measured viscosity did not change remarkably when the HTAB concentration was increased from 1 to 10 mol m^{-3}. This is due to the absence of surfactant-laden particles at the air–water interfaces across the foam film.

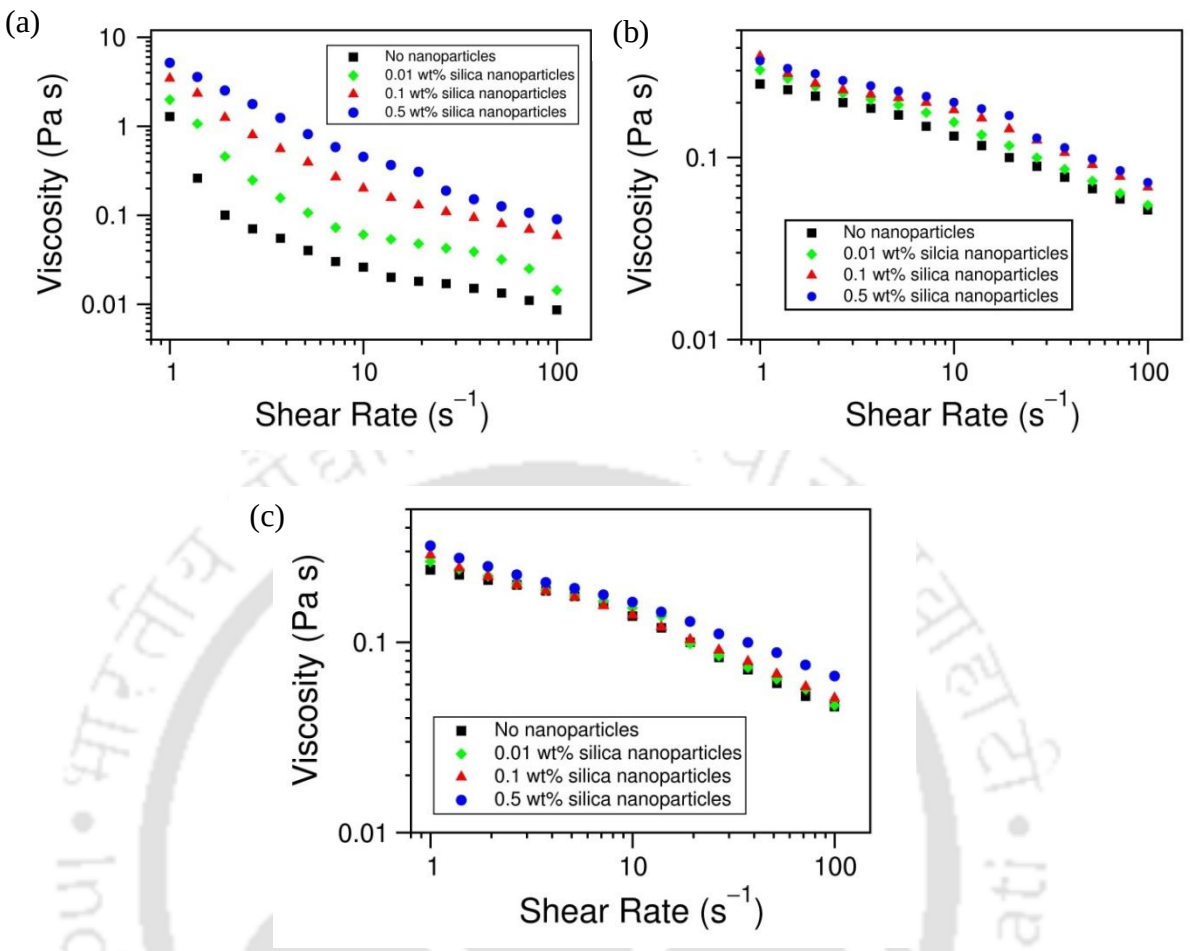

Figure 4.2 The effect of concentration of silica nanoparticles on the viscosity of foams at HTAB concentrations: (a) 0.1 mol m^{-3}, (b) 1 mol m^{-3}, and (c) 10 mol m^{-3}.

4.2.3 Shear rheology at air–water interface

When small surfactant molecules, such as HTAB, adsorb at the air–water interface from the bulk phase, they form a Gibbs monolayer. Surface tension is the most appropriate parameter to characterize such interfaces. On the other hand, macromolecules such as long-chain polymers or proteins, high molecular fatty acids, and nanoparticles form a Langmuir monolayer at the interface. When the silica nanoparticles adsorb at the air–water interface, they interact with the oppositely-charged surfactant molecules and form a

complex microstructure, which is similar to the Langmuir monolayers.[5,55] We have studied the dynamic behavior of the air–water interface covered with such microstructures by using interfacial shear rheology.

Figure 4.3 shows the effect of particles on the shear viscosity (η_s) of the air–water interface. η_s was remarkably high at high particle concentrations when the HTAB concentration was below the CMC (Figure 4.3a), and a shear thinning behavior was observed. The decrease in the viscosity was due to the destruction of the microstructure at the air–water interface. η_s was negligible in the absence of the silica nanoparticles (and therefore, it is not shown in Figure 4.3) because the interface formed a Gibbs monolayer, which had less strength than the Langmuir monolayer formed due to the adsorption of the surfactant-laden nanoparticles. A very low stress was required to shear the Gibbs

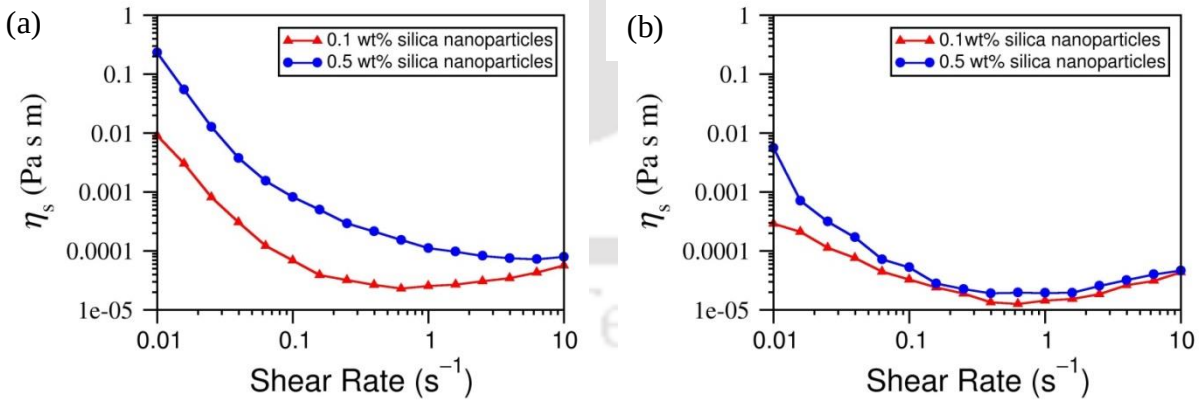

Figure 4.3 Interfacial shear viscosity (η_s) as a function of shear rate at two concentrations of the nanoparticles (i.e. 0.1 and 0.5 wt%) at the HTAB concentrations: (a) 0.1 mol m^{-3} and (b) 1 mol m^{-3}.

monolayer, which was below the lowest value measurable by the rheometer (i.e. ~10^{-5} Pa s m). At the higher shear rate (i.e. above 1 s^{-1}), the viscosity increased, which was due to the influence of the bulk liquid phase on the interface.[56] In contrast to low HTAB concentration, no significant influence of the particles was observed at HTAB concentrations above the CMC. Only a slight change occurred at very low shear rates. At high HTAB concentrations, η_s was much lower.

The nonlinear viscoelastic behavior at the air–water interface is shown in Figure 4.4. The interface was formed by the adsorption of surfactant-laden particles containing 0.1 mol m^{-3} HTAB and 0.5 wt% silica nanoparticles. This composition produced a high surface viscosity, and therefore it was chosen to study the nonlinear viscoelastic properties of the air–water interface. It has been observed[5] that the air–water interface showed nonlinear viscoelastic behavior when the strain amplitude was above 1% of the imposed sinusoidal strain. This also showed a weak strain overshoot because G_s'' initially increased, reached a local maximum, and then started to decrease. Figure 4.4 shows the elastic Lissajous–Bowditch curves, which were obtained by plotting the stress response as a function of strain in a complete cycle of the oscillation. In the linear viscoelastic regime (i.e. 1% of the imposed strain amplitude), the elastic Lissajous–Bowditch curve showed a perfect elliptical shape. This was caused by the perfect sinusoid of stress response. The elastic component of stress response, which was obtained by taking average of the stress responses during the positive and negative strain rates (as shown by the dashed line), was linearly dependent on the imposed strain, which signifies the elastic behavior of foam. Upon further increasing the strain amplitude,

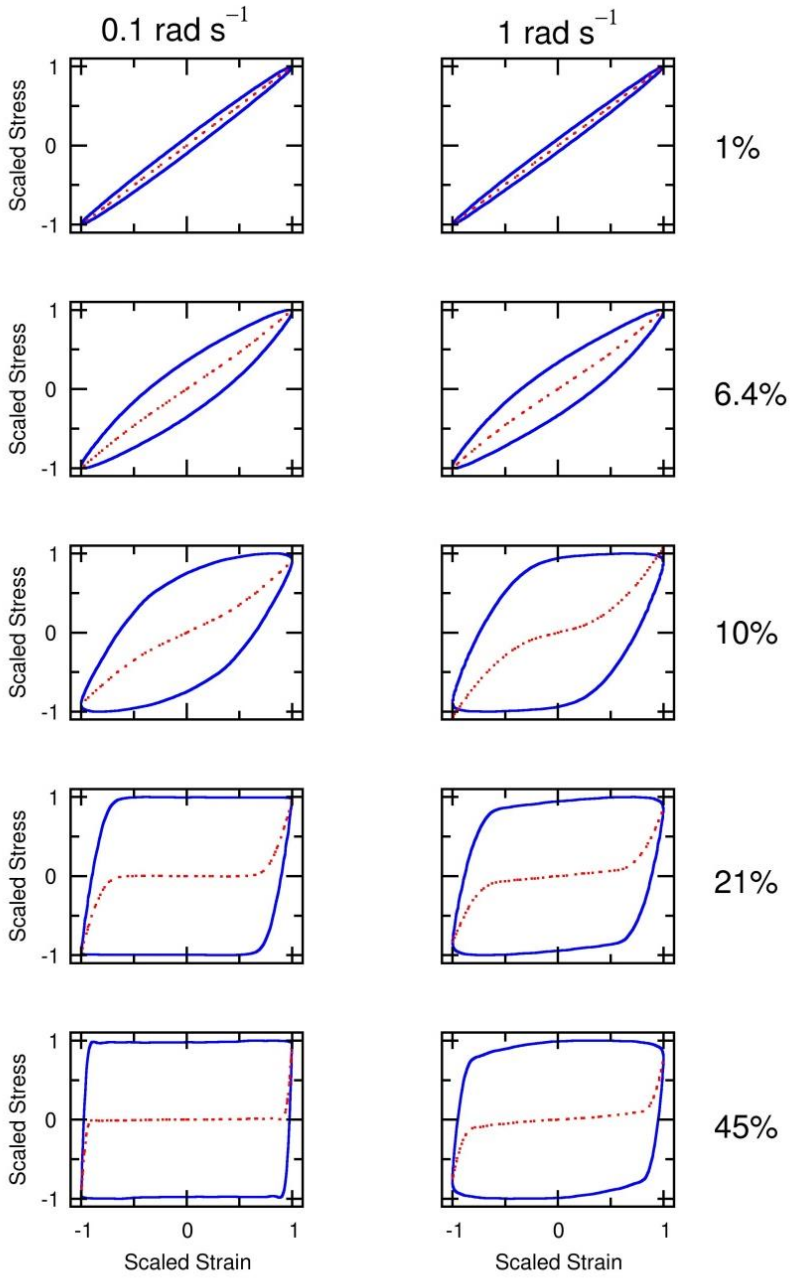

Figure 4.4 Elastic Lissajous–Bowditch curves (stress vs strain) of the air–water interface. The experiments were conducted at two angular frequencies (i.e. 0.1 and 1 rad s^{-1}) and five strain amplitudes (i.e. 1, 6.4, 10, 21, and 45%). The concentrations of HTAB and silica nanoparticles were 0.1 mol m^{-3} and 0.5 wt%, respectively.

the Lissajous–Bowditch curve became leaf-shaped, and thereafter changed to the rhombic shape. Dimitriou et al.[57] have proposed that such a transition is a representation of an elasto-viscoplastic system. At very high amplitude (i.e. 45%), the Lissajous–Bowditch curve took the shape of a parallelogram (i.e. the bottom left curve of Figure 4.4), which indicates the purely plastic flow behavior of the interface.[58] Birbaum et al.[41] have also observed a similar transition of the elastic Lissajous–Bowditch curves, which were elliptical at the low strain amplitude, and became rectangular at large strain amplitudes with plateaus on the top and the bottom of the curves. This plateau shows strain hardening behavior of foam.[59] The distortion of the shape of the Lissajous–Bowditch curves from elliptic to rectangular can be attributed to the influence of higher odd harmonic terms involved in the oscillatory stress response.[60] With increasing strain amplitude, width of the major axis of the Lissajous–Bowditch curve increased, which is attributed to the increase in the phase angle between the input sinusoidal strain and the stress output. The rectangular elastic Lissajous–Bowditch curves imply that the greatest increase in stress occurred when the strain was maximum, and the air–water interface showed strain-stiffening process at large deformation. The corresponding viscous Lissajous–Bowditch curves are shown in Figure 4.5. In the linear viscoelastic regime, the viscous Lissajous–Bowditch curves were spherical. In the nonlinear viscoelastic regime, they had sigmoid shape, which implies intracycle shear thinning behavior of the interface. The instantaneous viscosity is the ratio of the viscous component of the stress response (shown by the dashed line) and the strain rate in the viscous Lissajous–Bowditch curve. From Figure 4.5, it is observed that the instantaneous viscosity increased with increasing strain rate. However, at high strain amplitude (i.e. 45%), instantaneous viscosity became

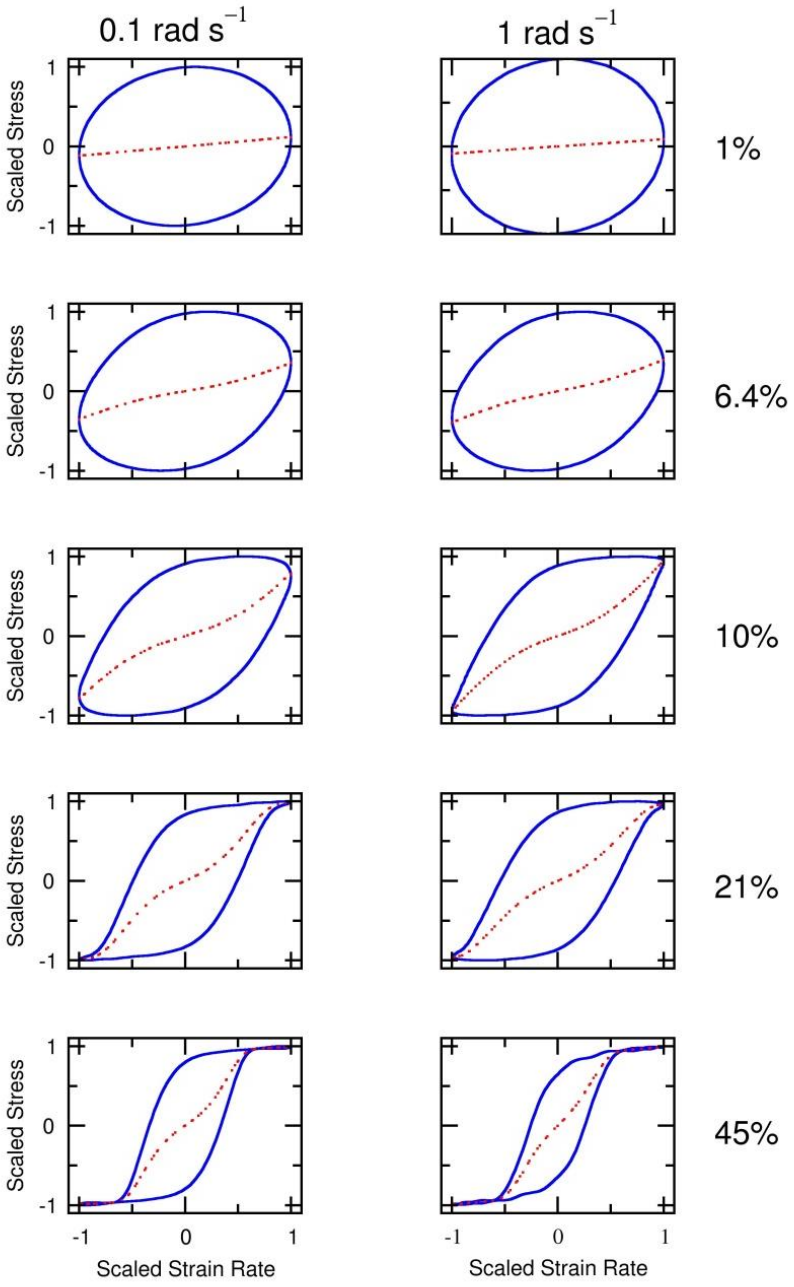

Figure 4.5 Viscous Lissajous–Bowditch curves (stress vs strain rate) of the air–water interface. The experiments were conducted at two angular frequencies (i.e. 0.1 and 1 rad s^{-1}) and five strain amplitudes (i.e. 1, 6.4, 10, 21, and 45%). The concentrations of HTAB and silica nanoparticles were 0.1 mol m^{-3} and 0.5 wt%, respectively.

zero at high strain rate, as the stress response was independent of the strain rate, which confirms the plastic flow behavior of the foam. This may occur due to the complete destruction of the microstructure (see Section 4.2.4) at the air–water interface.

4.2.4 Thickness of air–water interface and microstructure

Figure 4.6 shows the thickness of the air–water interfacial region after the adsorption of surfactant and the nanoparticles. The thickness was measured by varying the particle concentration at a fixed HTAB concentration. The nanoparticles had a significant effect on the thickness of the interface when the concentration of HTAB was below the CMC (i.e. 0.1 mol m^{-3}). Each peak represents the presence of a surfactant-laden nanoparticle. By increasing the concentration of the particles, more particles were found at the interface. The nanoparticles were hydrophilic and they had size in the range of 2.5 to 10 nm. Most part (~75%) of the surface of these particles was oriented towards the aqueous phase, and a lesser portion (~25%) was in the air, which corresponds to the peaks in Figure 4.6. Such peaks were not observed when the HTAB concentration was above the CMC, as shown in Figure 4.6b,c. At the higher surfactant concentrations, the air–water interface was completely covered by the surfactant molecules only, and the surfactant-laden particles remained in the sub-phase or in the bulk phase. Measurement of the film thickness at the air–water interface by ellipsometry has several limitations.[61] To support our results, we have studied the morphology of the monolayer at the air–water interface

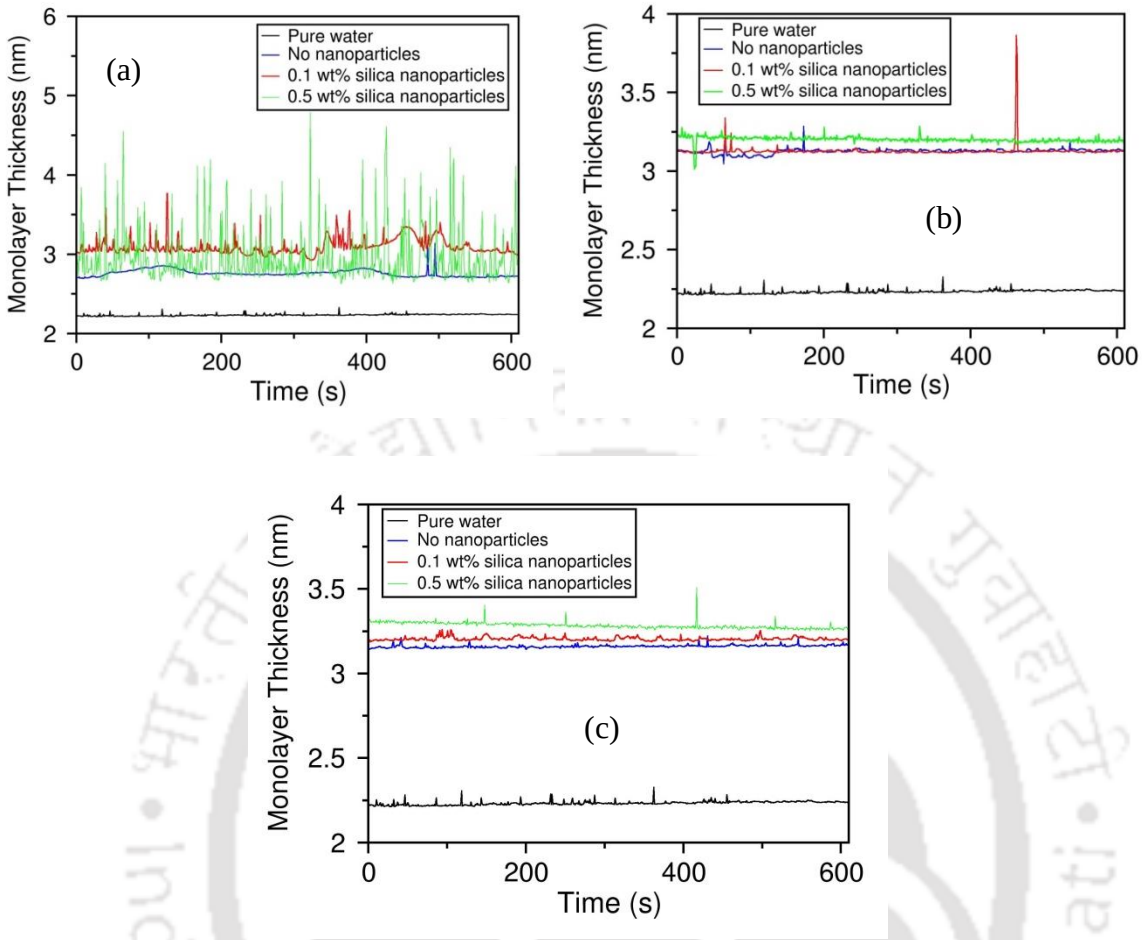

Figure 4.6 Variation of the thickness of the film with time at different particle concentrations. The thickness was measured by ellipsometry. Each peak depicts the presence of nanoparticles at the air–water interface. For each set of experiments, the HTAB concentration was kept constant and the particle concentration was varied from 0 to 0.5 wt%. The HTAB concentrations were: (a) 0.1 mol m^{-3}, (b) 1 mol m^{-3}, and 10 mol m^{-3}.

by using BAM (Figure 4.7). The images were taken at different concentrations of the nanoparticles and HTAB. The variation of particle concentration is shown from the left to right, and the same for HTAB is shown from the top to the bottom. More and more surfactant-laden particles could be seen at the air–water interface with increasing particle concentration, when HTAB concentration was below the CMC (i.e. 0.1 mol m^{-3}). On the other hand, no nanoparticle was observed when the HTAB concentration was above the CMC. To study the aggregation of the nanoparticles in the bulk phase, we have measured particle size distributions in the dispersions containing 0.5 wt% silica nanoparticles at various concentrations of HTAB (see Figure 4.8). The particle size increased with increasing HTAB concentration up to 0.1 mol m^{-3}. This indicates that there was an electrostatic attraction between the HTAB molecules and the silica nanoparticles (due to opposite charge). Consequently, the net surface charge on the particles reduced, which favored aggregation of the particles. With further increase in the HTAB concentration, particle size decreased. This indicates repulsion between the particles, which occurred due to the similar charges on the particles at high HTAB concentrations.

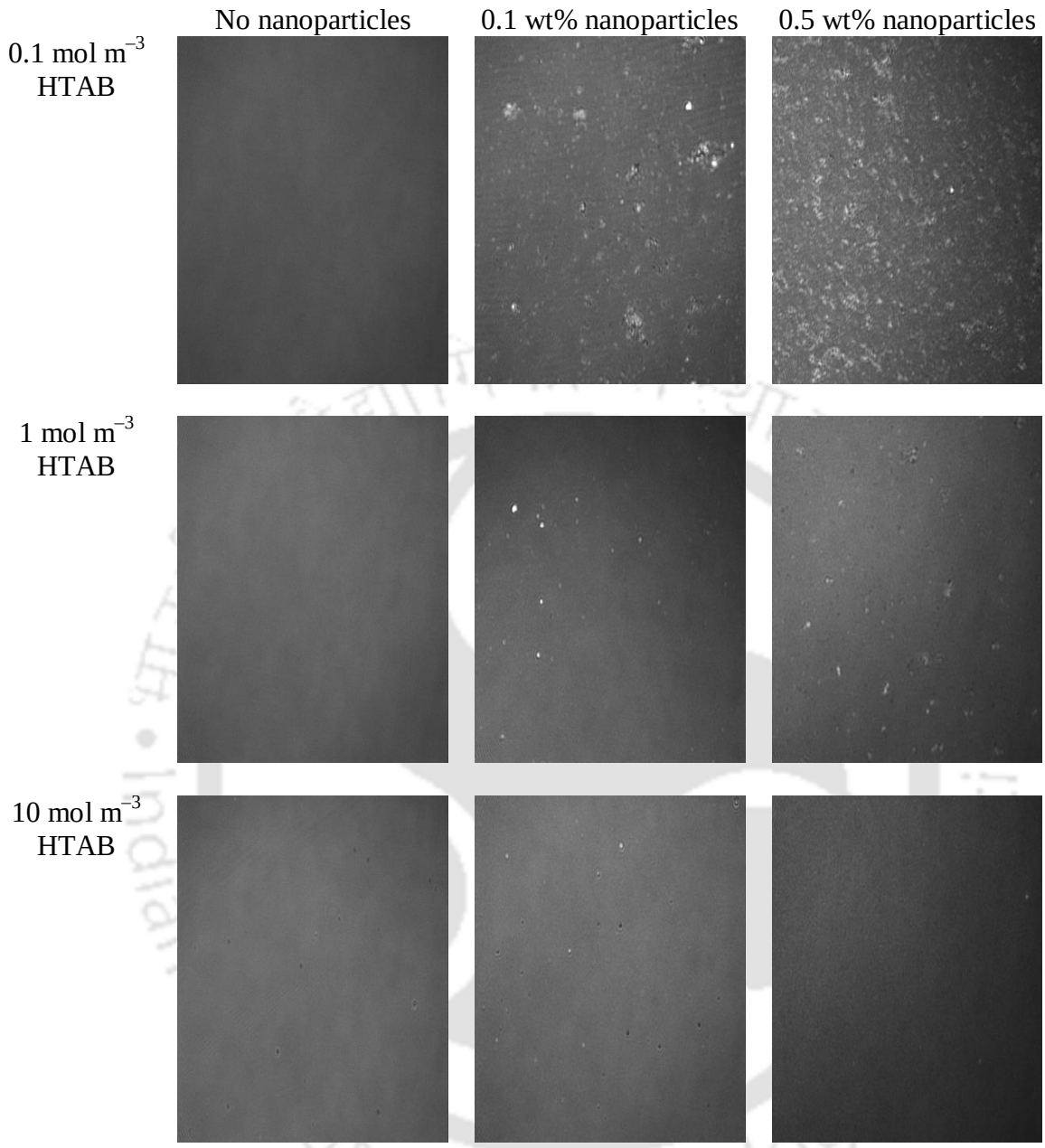

Figure 4.7 BAM images of the films formed at the air–water interface. The age of the air–water interface was 30 min. The dimensions of the images are 352 µm × 452 µm.

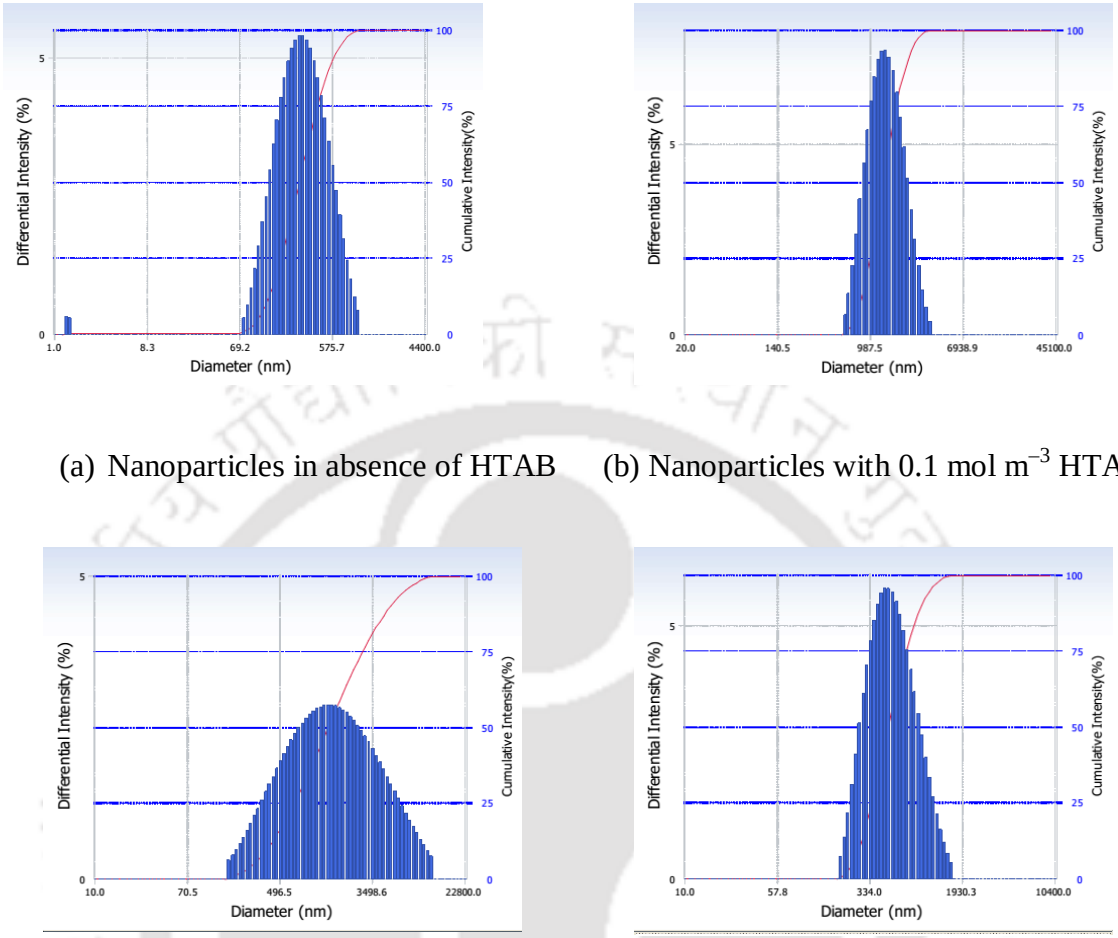

(a) Nanoparticles in absence of HTAB (b) Nanoparticles with 0.1 mol m^{-3} HTAB

(c) Nanoparticles with 1 mol m^{-3} HTAB (d) Nanoparticles with 10 mol m^{-3} HTAB

Figure 4.8 Size distributions of the silica nanoparticles in the dispersions containing a mixture of 0.5 wt% nanoparticles and different concentrations of HTAB: (a) nil, (b) 0.1 mol m^{-3}, (c) 1 mol m^{-3}, and (d) 10 mol m^{-3}.

Microstructure at the air–water interface formed by the adsorption of surfactant-laden nanoparticles was studied by using AFM (see Figure 4.9a). The size of the nanoparticles was found to be ~50 nm (Figure 4.9b). The actual size of the nanoparticles

present at the air–water interface was found from the TEM image (see Figure 4.9c). Agglomeration of the surfactant-laden particles can also be visualized from this figure.

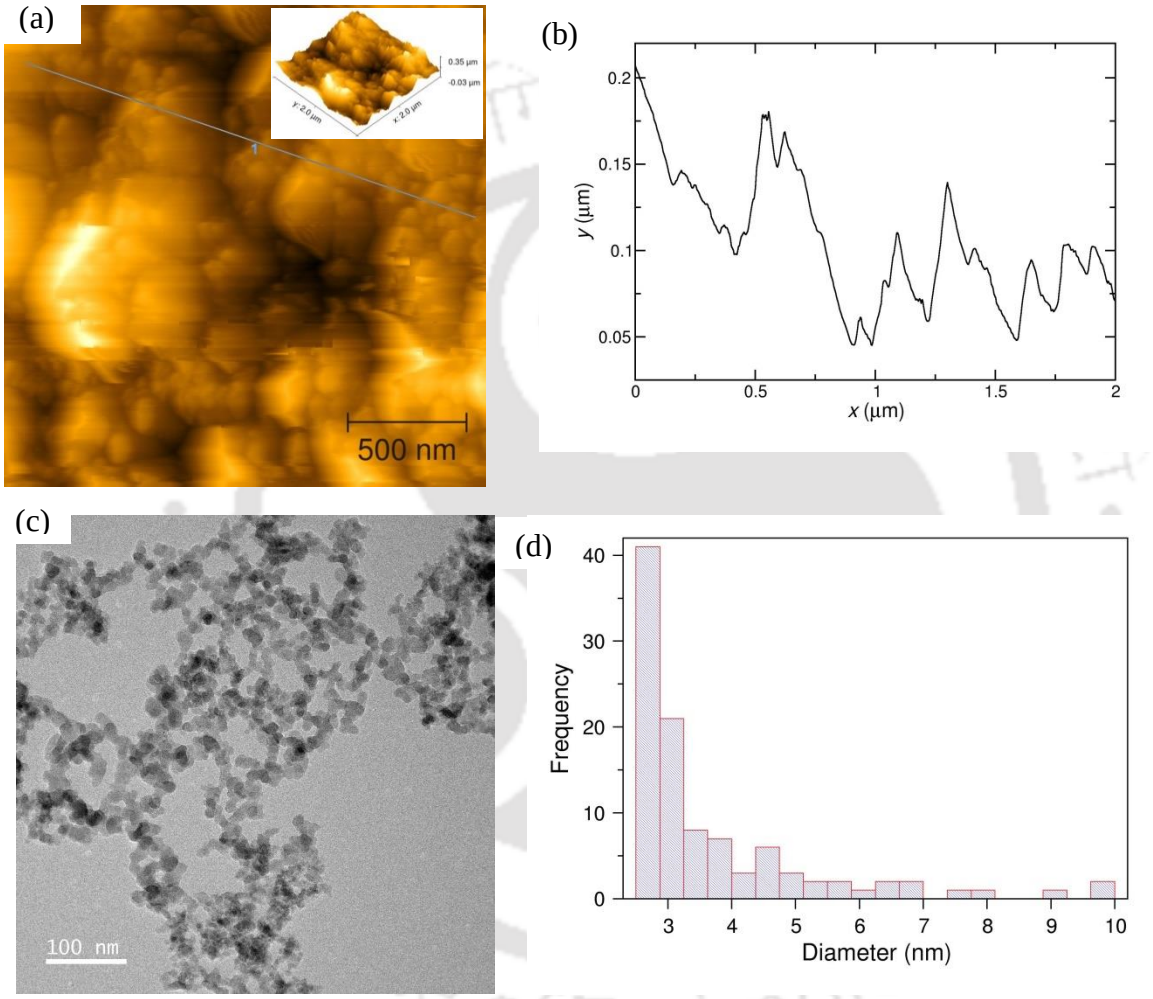

Figure 4.9 (a) AFM image of the monolayer at the air–water interface formed by the adsorption of surfactant-laden nanoparticles, (b) thickness of the monolayer vs the distance along the section (the dashed line) in Figure 4.9a, (c) TEM image of the nanoparticles (0.5 wt%) in the presence of 0.1 mol m^{-3} HTAB, and (d) size distribution of the surfactant-laden particles at the air–water interfaces corresponding to Figure 4.9c.

The size distribution of the nanoparticles at the interface is shown in Figure 4.9d, which was obtained from Figure 4.9c. Only small particles with diameter between 2.5 and 10 nm were adsorbed at the air–water interface. Larger particles remained in the liquid phase inside the foam film, some of which drained out with time.

Based on these experimental observations, it is apparent that at low HTAB concentrations (e.g. 0.1 mol m^{-3}), the smaller particles (i.e. diameter below 10 nm) adsorbed at the air–water interface. The adsorption was favored by the induced motion of the surfactant molecules, which were adsorbed onto the particles. At the air–water interface, adsorption of the particles was thermodynamically favored due to the large gain in Gibbs free energy (Equation 4.1).[3,62] However, the larger particles remained in the bulk liquid phase due to the dominant gravitational force.

Initially, the gravitational and capillary forces are responsible for the drainage of the foam film, which causes the film to thin. The silica nanoparticles present in the film form solid-like ordered structures as shown in Figure 4.10a. The structured zones overlap when the separation between the two surfaces (i.e. *h*) reduces. This gives rise to an oscillatory structural force between the particle layers, as shown in Figure 4.10b.[63] During the drainage, as the film thickness reduces to a few particle diameters (i.e. *d*), the packing of the particles influences the interaction between the surfaces. When the film thickness is reduced to ~20 nm, the DLVO forces start acting between the two surfaces (Equation 4.3). Below ~10 nm thickness, most of the particles present in the film liquid are drained out. The two surfaces may collapse due to the action of the van der Waals force.

(a)

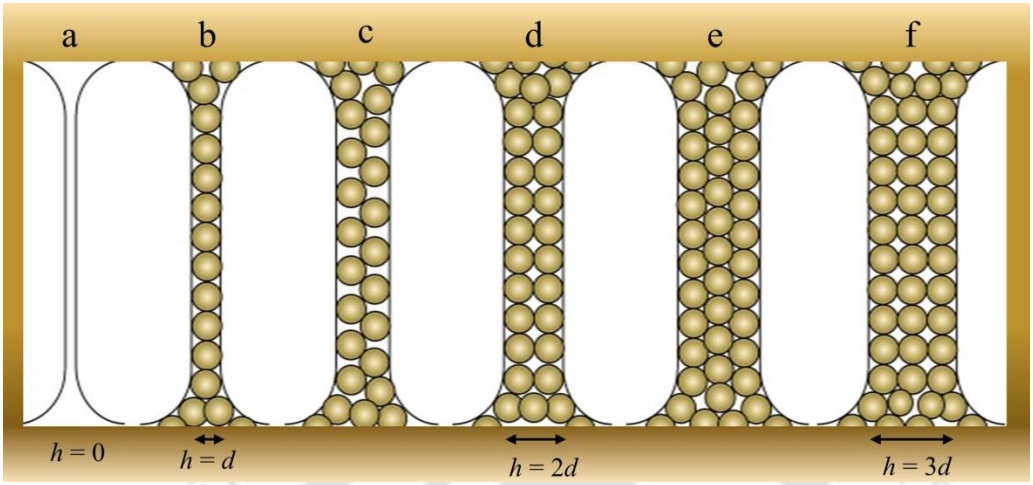

(b)

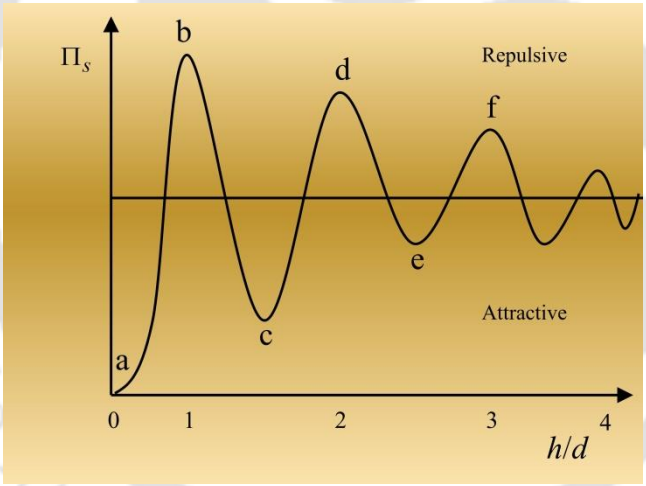

Figure 4.10 (a) Schematic diagram of the mechanism of stability of thin liquid film in the presence of nanoparticles and (b) the respective profile of disjoining pressure due to oscillatory structural force. *h* is the separation between air–water interfaces and *d* is the diameter of the nanoparticles.

Above the CMC, the charged surfactant molecules were present at the interface as well as in the aqueous film phase. For HTAB, a repulsive hydration force[64] may stabilize the thin foam film against the van der Waals force.[29,65] It increases

monotonically as the two surfaces approach each other. However, at very low separation (i.e. below about 1.5 nm), the water molecules start oscillating due to long-term intermolecular forces.[29,66]

Below the CMC, the surfactant-laden particles attached to the air–water interfaces come into close proximity. A strong repulsive hydration force operates between the approaching particles.[67] This force stabilizes the thin liquid film. Furthermore, as drainage continues, the liquid film is covered with a single layer of particles (see Figure 4.10a), and thereafter the plane surfaces deform into a meniscus. As the deformation of the meniscus continues, the thickness between the menisci of the two surfaces decreases, and consequently, the capillary interaction increases. Equation 4.4 describes the case when the two menisci just touch each other (i.e. the film thickness reduces to zero). However, in the presence of particles, the thickness between the two surfaces cannot reduce to zero. Hence, coalescence can be completely inhibited by using particles.[68-70] Therefore, the foam was more stable in the presence of nanoparticles when the HTAB concentration was below the CMC.

4.3 Conclusions

The effect of silica nanoparticles on the interaction between air–water interfaces across foam films in the presence of HTAB was studied. The nanoparticles having diameter less than 10 nm adsorbed at the air–water interface when the HTAB concentration was below the CMC. This adsorption was induced by the surfactant molecules adsorbed on the surface of the particles. Since the silica nanoparticles were hydrophilic, a major portion of these particles was oriented towards the aqueous phase, and hence a lesser portion was in the air. The adsorption of the surfactant-laden particles at the air–water interface

resulted in the formation of a Langmuir-type monolayer, which provided good mechanical strength to the interface. Consequently, the interfacial shear viscosity was high. The DLVO forces and the capillary interaction are the major forces responsible for stabilizing the foam films. Bubble coalescence was almost prevented when the surfactant-laden particles were present at the interfaces. Consequently, foams were stable for a longer period and the particles strongly influenced their stability, which was confirmed by the high viscosity and viscoelasticity of the foams, as well as the air–water interface.

However, when the HTAB concentration was above the CMC, the air–water interfaces were completely covered by the surfactant molecules and the surfactant-laden particles remained in the liquid phase inside the film, which drained-out with time. Therefore, due to their absence at the interfaces, the particles did not have any significant influence on the stability of the foams. The surfactant-laden particles formed aggregates in the bulk phase as well as at the air–water interfaces.

Stability of the foams increased with increasing viscosity whereas, the foamability increased with increasing surfactant concentration. The nanoparticles affected both foam stability and foamability when the HTAB concentration was below the CMC.

The Lissajous–Bowditch curves of the air–water interface exhibited linear viscoelastic behavior at the low strain amplitude and nonlinear viscoelastic behavior at the high strain amplitude, with a plastic flow behavior at 45% strain amplitude.

Nomenclature

d	diameter of nanoparticle, m
G_s'	interfacial storage modulus, Pa m
G_s''	interfacial loss modulus, Pa m
h	separation between air–water interfaces, m
i	imaginary unit
p	packing parameter
P_d	pressure of the dispersed phase, Pa
P_l	pressure of the liquid phase, Pa
$P_c^{\max}$	maximum capillary pressure, Pa
R	radius of nanoparticle, nm

Greek Letters

γ	surface tension, N m^{-1}
Δ	phase difference, rad
ΔE	minimum energy, J
ΔP	pressure difference, Pa
η_s	interfacial shear viscosity, Pa s m
θ	contact angle, rad
Π	disjoining pressure, Pa
Π_e	disjoining pressure due to electrostatic double layer repulsion, Pa

Π_s	disjoining pressure due to short-range repulsion, Pa
Π_v	disjoining pressure due to van der Waals attraction, Pa
ρ	ellipticity
ψ	amplitude ratio

Abbreviations

AFM	atomic force microscopy
BAM	Brewster angle microscopy
CMC	critical micelle concentration
DLS	dynamic light scattering
DLVO	Derjaguin–Landau–Verwey–Overbeek
HTAB	hexadecyltrimethylammonium bromide
TEM	transmission electron microscopy

References

(1) Vijayaraghavan, K.; Nikolov, A.; Wasan, D.; Henderson, D. Foamability of Liquid Particle Suspensions: A Modeling Study. *Ind. Eng. Chem. Res.* **2009,** *48,* 8180–8185.

(2) Dickinson, E. Structuring of Colloidal Particles at Interfaces and the Relationship to Food Emulsion and Foam Stability. *J. Colloid Interface Sci.* **2015,** *449,* 38–45.

(3) Binks, B. P. Particles as Surfactants–Similarities and Differences. *Curr. Opin. Colloid Interface Sci.* **2002,** *7,* 21–41.

(4) Yekeen, N.; Idris, A. K.; Manan, M. A.; Samin, A. M. Experimental Study of the Influence of Silica Nanoparticles on the Bulk Stability of SDS-foam in the Presence of Oil. *J. Dispersion Sci. Technol.* **2017,** *38,* 416–424.

(5) Vishal, B.; Ghosh, P. Foaming in Aqueous Solutions of Hexadecyltrimethylammonium Bromide and Silica Nanoparticles: Measurement

and Analysis of Rheological and Interfacial Properties. *J. Dispersion Sci. Technol.* **2018,** *39,* 62–70.

(6) Zargartalebi, M.; Barati, N.; Kharrat, R. Influences of Hydrophilic and Hydrophobic Silica Nanoparticles on Anionic Surfactant Properties: Interfacial and Adsorption Behaviors. *J. Pet. Sci. Eng.* **2014,** *119*, 36–43.

(7) Vatanparast, H.; Samiee, A.; Bahramian, A.; Javadi, A. Surface Behavior of Hydrophilic Silica Nanoparticle–SDS Surfactant Solutions: I. Effect of Nanoparticle Concentration on Foamability and Foam Stability. *Colloids Surf., A* **2017,** *513,* 430–441.

(8) Knapik, E.; Stopa, J.; Marzec, A. Foams Stabilized with Nanoparticles for Gas Well Deliquification. *Pol. J. Chem. Technol.* **2014,** *16*, 114–117.

(9) Joshi, K. S.; Baumann, A.; Jeelani, S. A. K.; Blickenstorfer, C.; Naegeli, I.; Windhab, E. J. Mechanism of Bubble Coalescence Induced by Surfactant Covered Antifoam Particles. *J. Colloid Interface Sci.* **2009,** *339*, 446–453.

(10) Maestro, A.; Rio, E.; Drenckhan, W.; Langevin, D.; Salonen, A. Foams Stabilised by Mixtures of Nanoparticles and Oppositely Charged Surfactants: Relationship between Bubble Shrinkage and Foam Coarsening. *Soft Matter* **2014,** *10,* 6975–6983.

(11) Arriaga, L. R.; Drenckhan, W.; Salonen, A.; Rodrigues, J. A.; Iniguez-Palomares, R.; Rio, E.; Langevin, D. On the Long-term Stability of Foams Stabilised by Mixtures of Nano-particles and Oppositely Charged Short Chain Surfactants. *Soft Matter* **2012,** *8,* 11085–11097.

(12) Liu, Q.; Zhang, S.; Sun, D.; Xu, J. Foams Stabilized by Laponite Nanoparticles and Alkylammonium Bromides with Different Alkyl Chain Lengths. *Colloids Surf., A* **2010,** *355,* 151–157.

(13) Tambe, D. E.; Sharma, M. M. The Effect of Colloidal Particles on Fluid–Fluid Interfacial Properties and Emulsion Stability. *Adv. Colloid Interface Sci.* **1994,** *52,* 1–63.

(14) Yekeen, N.; Manan, M. A.; Idris, A. K.; Padmanabhan, E.; Junin, R.; Samin, A. M.; Gbadamosi, A. O.; Oguamah, I. A Comprehensive Review of Experimental Studies of Nanoparticles-stabilized Foam for Enhanced Oil Recovery. *J. Pet. Sci. Eng.* **2018,** *164*, 43–74.

(15) Kaptay, G. Interfacial Criteria for Stabilization of Liquid Foams by Solid Particles. *Colloids Surf. A* **2004,** *230,* 67–80.

(16) Abdel-Fattah, A. I.; El-Genk, M. S. On Colloidal Particle Sorption onto a Stagnant Air–Water Interface. *Adv. Colloid Interface Sci.* **1998,** *78,* 237–266.

(17) Bournival, G.; Ata, S.; Wanless, E. J. The Roles of Particles in Multiphase Processes: Particles on Bubble Surfaces. *Adv. Colloid Interface Sci.* **2015,** *225,* 114–133.

(18) Dimova, R.; Danov, K.; Pouligny, B.; Ivanov, I. B. Drag of a Solid Particle Trapped in a Thin Film or at an Interface: Influence of Surface Viscosity and Elasticity. *J. Colloid Interface Sci.* **2000,** *226,* 35–43.

(19) Ivanov, I. B. Effect of Surface Mobility on the Dynamic Behavior of Thin Luquid Films. *Pure Appl. Chem.* **1980,** *52,* 1241–1262.

(20) Stubenrauch, C.; von Klitzing, R. Disjoining Pressure in Thin Liquid Foam and Emulsion Films – New Concepts and Perspectives. *J. Phys.: Condens. Matter* **2003,** *15,* R1197–R1232.

(21) Derjaguin, B. V.; Churaev, N. V. Structure Component of Disjoining Pressure. *J. Colloid Interface Sci.* **1974,** *49,* 249–255.

(22) Bergeron, V.; Radke, C. J. Equilibrium Measurements of Oscillatory Disjoining Pressures in Aqueous Foam Films. *Langmuir* **1992,** *8,* 3020–3026.

(23) Danov, K. D.; Ivanov, I. B.; Ananthapadmanabhan, K. P.; Lips, A. Disjoining Pressure of Thin Films Stabilized by Nonionic Surfactants. *Adv. Colloid Interface Sci.* **2006,** *128,* 185–215.

(24) Verwey, E. J. W.; Overbeek, J. Th. G. *Theory of Stability of Lyophobic Colloids*; Elsevier: Amsterdam, 1948.

(25) Derjaguin, B. V. *Theory of Stability of Colloids and Thin Liquid Films*; Plenum Press: New York, 1989.

(26) Bergeron, V. Forces and Structure in Thin Liquid Soap Films. *J. Phys.: Condens. Matter* **1999,** *11,* R215–R238.

(27) Ninham, B. W.; Pashley, R. M.; Nostro, P. L. Surface Forces: Changing Concepts and Complexity with Dissolved Gas, Bubbles, Salt and Heat. *Curr. Opin. Colloid Interface Sci.* **2017,** *27,* 25–32.

(28) Joye, J.-L.; Miller, C. A.; Hirasaki, G. J. Dimple Formation and Behavior During Axisymmetrical Foam Film Drainage. *Langmuir* **1992,** *8,* 3083–3092.

(29) Clunie, J. S.; Goodman, J. F.; Symons, P. C. Solvation Forces in Soap Films. *Nature* **1967,** *216,* 1203–1204.

(30) Kaptay, G. On the Equation of the Maximum Capillary Pressure Induced by Solid Particles to Stabilize Emulsions and Foams and on the Emulsion Stability Diagrams. *Colloids Surf. A* **2006,** *282,* 387–401.

(31) Ali, S. A.; Gauglitz, P. A.; Rossen, W. R. Stability of Solids-coated Liquid Layers between Bubbles. *Ind. Eng. Chem. Res.* **2000,** *39,* 2742–2745.

(32) Lexis, M.; Willenbacher, N. Yield Stress and Elasticity of Aqueous Foams from Protein and Surfactant Solutions – The Role of Continuous Phase Viscosity and Interfacial Properties. *Colloids Surf., A* **2014,** *459,* 177–185.

(33) Zang, D.; Langevin, D.; Binks, B. P.; Wei, B. Shearing Particle Monolayers: Strain-rate Frequency Superposition. *Phys. Rev. E.* **2010,** *81,* 011604.

(34) Zang, D. Y.; Rio, E.; Langevin, D.; Wei, B.; Binks, B. P. Viscoelastic Properties of Silica Nanoparticle Monolayers at the Air–Water Interface. *Eur. Phys. J. E* **2010,** *31,* 125–134.

(35) Fuller, G. G.; Vermant, J. Complex Fluid–Fluid Interfaces: Rheology and Structure. *Annu. Rev. Chem. Biomol. Eng.* **2012,** *3,* 519–543.

(36) Sharma, V.; Jaishankar, A.; Wang, Y.-C.; McKinley, G. H. Rheology of Globular Proteins: Apparent Yield Stress, High Shear Rate Viscosity and Interfacial Viscoelasticity of Bovine Serum Albumin Solutions. *Soft Matter* **2011,** *7,* 5150–5160.

(37) Hyun, K.; Kim, S. H.; Ahn, K. H.; Lee, S. J. Large Amplitude Oscillatory Shear as a Way to Classify the Complex Fluids. *J. Non-Newtonian Fluid Mech.* **2002,** *107,* 51–65.

(38) Ewoldt, R. H.; Hosoi, A. E.; McKinley, G. H. New Measures for Characterizing Nonlinear Viscoelasticity in Large Amplitude Oscillatory Shear. *J. Rheol.* **2008,** *52,* 1427–1458.

(39) Cho, K. S.; Hyun, K.; Ahn, K. H.; Lee, S. J. A Geometrical Interpretation of Large Amplitude Oscillatory Shear Response. *J. Rheol.* **2005,** *49,* 747–758.

(40) Yu, W.; Wang, P.; Zhou, C. General Stress Decomposition in Nonlinear Oscillatory Shear Flow. *J. Rheol.* **2009,** *53,* 215–238.

(41) Birbaum, F. C.; Haavisto, S.; Koponen, A.; Windhab, E. J.; Fischer, P. Shear Localisation in Interfacial Particle Layers and Its Influence on Lissajous-plots. *Rheol. Acta* **2016,** *55,* 267–278.

(42) Sagis, L. M. C.; Fischer, P. Nonlinear Rheology of Complex Fluid–Fluid Interfaces. *Curr. Opin. Colloid Interface Sci.* **2014,** *19,* 520–529.

(43) Erni, P.; Parker, A. Nonlinear Viscoelasticity and Shear Localization at Complex Fluid Interfaces. *Langmuir* **2012,** *28,* 7757–7767.

(44) Rühs, P. A.; Affolter, C.; Windhab, E. J.; Fischer, P. Shear and Dilatational Linear and Nonlinear Subphase Controlled Interfacial Rheology of Beta-Lactoglobulin Fibrils and their Derivatives. *J. Rheol.* **2013,** *57,* 1003–1022.

(45) Hyun, K.; Wilhelm, M.; Klein, C. O.; Cho, K. S.; Nam, J. G.; Ahn, K. H.; Lee, S. J.; Ewoldt, R. H.; McKinley, G. H. A Review of Nonlinear Oscillatory Shear Tests: Analysis and Application of Large Amplitude Oscillatory Shear (LAOS). *Prog. Polym. Sci.* **2011,** *36,* 1697–1753.

(46) Binks, B. P.; Murakami, R. Phase Inversion of Particle-stabilized Materials from Foams to Dry Water. *Nat. Mater.* **2006,** *5,* 865–869.

(47) Zhang, S. Y.; Lan, Q.; Liu, Q.; Xu, H.; Sun, D. J. Aqueous Foams Stabilized by Laponite and CTAB. *Colloids Surf., A* **2008,** *317,* 406–413.

(48) Trahar, W. J. A Rational Interpretation of the Role of Particle-size in Flotation. *Int. J. Miner. Process.* **1981,** *8,* 289–327.

(49) Dickinson, E.; Ettelaie, R.; Kostakis, T.; Murray, B. S. Factors Controlling the Formation and Stability of Air Bubbles Stabilized by Partially Hydrophobic Silica Nanoparticles. *Langmuir* **2004,** *20,* 8517–8525.

(50) Stamou, D.; Duschl, C.; Johannsmann, D. Long-range Attraction between Colloidal Spheres at the Air–Water Interface: The Consequence of an Irregular Meniscus. *Phys. Rev. E.* **2000,** *62,* 5263–5272.

(51) Anjali, T. G.; Basavaraj, M. G. Shape-induced Deformation, Capillary Bridging, and Self-assembly of Cuboids at the Fluid–Fluid Interface. *Langmuir* **2017,** *33,* 791–801.

(52) Coertjens, S.; De Dier, R.; Moldenaers, P.; Isa, L.; Vermant, J. Adsorption of Ellipsoidal Particles at Liquid–Liquid Interfaces. *Langmuir* **2017,** *33,* 2689–2697.

(53) Schramm, L. L. *Emulsions, Foams, and Suspensions: Fundamentals and Applications*; John Wiley & Sons: Strauss GmbH, Mörlenbach, 2006.

(54) Horozov, T. S. Foams and Foam Films Stabilised by Solid Particles. *Curr. Opin. Colloid Interface Sci.* **2008,** *13,* 134–140.

(55) Edwards, D. A.; Brenner, H.; Wasan, D. T. *Interfacial Transport Processes and Rheology*; Butterworth–Heinemann: Stonheam, MA, 1991.

(56) Erni, P.; Fischer, P.; Windhab, E. J.; Kusnezov, V.; Stettin, H.; Laüger, J. Stress- and Strain-controlled Measurements of Interfacial Shear Viscosity and Viscoelasticity at Liquid/Liquid and Gas/Liquid Interfaces. *Rev. Sci. Instrum.* **2003,** *74,* 4916–4924.

(57) Dimitriou, C. J.; Ewoldt, R. H.; McKinley, G. H. Describing and Prescribing the Constitutive Response of Yield Stress Fluids using Large Amplitude Oscillatory Shear Stress (LAOStress). *J. Rheol.* **2013,** *57,* 27–70.

(58) Ewoldt, R. H.; Winter, P.; Maxey, J.; McKinley, G. H. Large Amplitude Oscillatory Shear of Pseudoplastic and Elastoviscoplastic Materials. *Rheol. Acta* **2010,** *49,* 191–212.

(59) Mermet-Guyennet, M. R. B.; de Castro, J. G.; Habibi, M.; Martzel, N.; Denn, M. M.; Bonn, D. LAOS: The Strain Softening/Strain Hardening Paradox. *J. Rheol.* **2015,** *59,* 21–32.

(60) Wilhelm, M. Fourier-Transform Rheology. *Macromol. Mater. Eng.* **2002,** *287,* 83–105.

(61) Campbell, R. A.; Arteta, M. Y.; Angus-Smyth, A.; Nylander, T.; Noskov, B. A.; Varga, I. Direct Impact of Nonequilibrium Aggregates on the Structure and Orphology of Pdadmac/SDS Layers at the Air/Water Interface. *Langmuir* **2014,** *30,* 8664–8674.

(62) Safouane, M.; Langevin, D.; Binks, B. P. Effect of Particle Hydrophobicity on the Properties of Silica Particle Layers at the Air−Water Interface. *Langmuir* **2007,** *23,* 11546–11553.

(63) Nikolov, A. D.; Wasan, D. T. Dispersion Stability due to Structural Contributions to the Particle Interaction as Probed by Thin Liquid–Film Dynamics. *Langmuir* **1992,** *8,* 2985–2994.

(64) Israelachvili, J. N.; Pashley, R. M. Molecular Layering of Water at Surfaces and Origin of Repulsive Hydration Forces. *Nature* **1983,** *306,* 249–250.

(65) Pashley, R. M. Hydration Forces between Mica Surfaces in Aqueous Elctrolyte Solutions. *J. Colloid Interface Sci.* **1981,** *80,* 153–162.

(66) Israelachvili, J. N. *Intermolecular and Surface Forces*; Academic press: New York, 2011.

(67) Kralchevsky, P. A.; danov, K. D.; Ivanov, I. B. *Thin Liquid Film Physics*. Marcel Dekker, New York, **1995,** 1–98.

(68) Chu, X.; Nikolov, A.; Wasan, D. Effects of Particle Size and Polydispersity on the Depletion and Structural Forces in Colloidal Dispersions. *Langmuir* **1996,** *12,* 5004–5010.

(69) Sethumadhavan, G. N.; Nikolov, A.; Wasan, D. Film Stratification in the Presence of Colloidal Particles. *Langmuir* **2001,** *17,* 2059–2062.

(70) Tcholakova, S.; Denkov, N. D.; Lips, A. Comparison of Solid Particles, Globular Proteins and Surfactants as Emulsifiers. *Phys. Chem. Chem. Phys.* **2008,** *10,* 1608–1627.

Chapter 5

Nonlinear Viscoelastic Behavior of Aqueous Foam under Large Amplitude Oscillatory Shear Flow

5.1 Introduction

Aqueous foams are soft complex materials, which show viscoelastic behavior and possess an apparent yield stress. The rheology of these foams is of great interest in the production of cosmetics and foods, oil recovery, and minerals separation.[1-5] When an oscillatory shear strain is imposed below its yield value, foams exhibit solid-like behavior as the storage modulus (G') is greater than the loss modulus (G'').[6] Upon increasing the strain amplitude (γ_0), a nonlinear viscoelastic response sets in. A detailed study of a linear viscoelastic behavior of foams has been reported elsewhere.[7,8] Princen,[9] and Khan and Armstrong[10] have correlated the stress-response with the morphology of the foams by considering a two-dimensional network model. This can also be studied by simulating the foams based on their geometry using a two- or three-dimensional model.[11] Various methods have been proposed to study nonlinear viscoelastic properties of foams. Steady shear flow has been used to study the nonlinear behavior of foams.[12] When the foam is sheared below its yield value, the angle between the foam films still remains $2\pi/3$ rad, as per the Plateau's law. Therefore, the static force between the foam films is balanced. The balance of force is lost if the stress is above its yield point, and the foam bubbles start sliding along each other in the flow direction. This type of flow is generally characterized by using the three-parameter Herschel–Bulkley model. Another method involves shearing the foam under oscillatory deformation. By analyzing G' and G'' as a function of γ_0 (i.e. amplitude sweep experiment), the large amplitude oscillatory shear (LAOS) behavior is divided into four categories, i.e. shear-thinning, strain-hardening, weak strain overshoot, and strong strain overshoot.[13] It has been found that

two materials displaying the same type of amplitude sweep graph may show different nonlinear stress waveforms.[14,15]

Fourier transform (FT) rheology is a sensitive method to deal with nonlinear viscoelastic behavior because it can detect very small oscillatory signals that arise during LAOS.[16-20] Investigating foams by the FT-rheology is challenging because its constituents (i.e. water and air) are Newtonian fluids and have low viscosity. Therefore, amplitude oscillatory tests alone may not be adequate in describing the response under LAOS by means of FT-rheology. Rouyer et al.[19] studied the LAOS behavior of aqueous foams in the full-stress harmonic spectrum to characterize the transition from linear to nonlinear viscoelastic behavior. Ewoldt et al.[21] and Khandavalli and Rothstein[22] studied the nonlinear viscoelastic properties by analyzing the stress response and the Lissajous–Bowditch curves. These curves are helpful in distinguishing the behavior of foams under deformation. For instance, in a stress vs. strain curve, an ellipsoidal shape characterizes viscous dissipation, while a parallelogram indicates plastic dissipation. Hyun et al.[20] have reviewed the LAOS behavior in detail. Recently, the study of LAOS behavior of food foams stabilized by proteins has been studied.[23] Several authors[24-30] have developed nonlinear models based on the Giesekus constitutive equation[31] and determined nonlinear parameters[32,33] to deal with LAOS. Rogers et al.[34] have proposed an approach, known as a sequence of physical processes, in an intracycle Lissajous–Bowditch curve to a yield stress fluid. The same approach was further used in many more LAOS studies.[35-38] A great deal of research has been conducted on the linear viscoelastic behavior of foams stabilized by nanoparticles and surfactants,[39-41] but its nonlinear behavior (i.e. LAOS) has hardly been reported. Neither the complex shear dynamic

modulus nor the steady flow analysis at the high shear rates have been able to provide physically-meaningful information about the foams.

In this work, we have systematically studied the nonlinear viscoelastic behavior of foam, which was stabilized by a mixture of 0.1 mol m^{-3} hexadecyltrymethylammonium bromide (HTAB) and 0.5% (by weight) silica nanoparticles. The LAOS behavior of foam was described by the stress-response waveforms and Lissajous–Bowditch plots, obtained by shearing the foam at different amplitudes of oscillation. The contributions of higher harmonic oscillatory terms were found by using FT-rheology and the Chebyshev polynomials. Finally, the interpretation of the LAOS behavior of foam was described based on a sequence of physical processes.

5.2 Theoretical background

In dynamic oscillatory shear rheology, a material is allowed to flow by imposing a sinusoidal strain in a strain-controlled rheometer. The strain is given by

$$\gamma(\omega,t) = \gamma_0 \sin(\omega t) \tag{5.1}$$

and the corresponding strain rate is given by

$$\dot{\gamma}(\omega,t) = \omega\gamma_0 \cos(\omega t) \tag{5.2}$$

where γ_0 and ω are strain amplitude and frequency of oscillation, respectively. When the γ_0 is in the linear viscoelastic regime, the stress response is also sinusoidal with the same ω. It is given by

$$\sigma(\omega,t) = \sigma_0 \sin(\omega t + \delta) \tag{5.3}$$

where σ_0 is the stress amplitude and δ is the phase angle between the stress response and the imposed strain. Equation 5.3 can be decomposed into two parts corresponding to the in- and out-of-phase to strain inputs as follows:

$$\sigma(\omega,t) = \sigma_0 \cos(\delta)\sin(\omega t) + \sigma_0 \sin(\delta)\cos(\omega t) \tag{5.4a}$$

$$\sigma(\omega,t) = \sigma' \sin(\omega t) + \sigma'' \cos(\omega t) \tag{5.4b}$$

where σ' and σ'' are the components of the stress response for in- and out-of-phase, respectively.

Two well-defined material functions (i.e. $G' = \sigma'/\gamma_0$ and $G'' = \sigma''/\gamma_0$) are used to characterize the linear viscoelastic behavior of a material. G' describes the elastic behavior and G'' describes the viscous behavior of materials. Equation 5.4b can be written as[42]

$$\sigma(\omega,t) = \gamma_0\left[G'(\omega)\sin(\omega t) + G''(\omega)\cos(\omega t)\right] \tag{5.5}$$

In a typical amplitude sweep measurement, both these moduli remain constant up to a certain limiting value of γ_0. The measurement of viscoelastic behavior below and above this limit are termed *linear* and *nonlinear viscoelastic regime*, respectively. In the linear regime, only the first harmonic oscillation is considered for the viscoelastic properties of the materials. However, when a material is deformed in the nonlinear regime, the contribution of higher harmonic terms also becomes significant. Therefore, higher harmonic terms are incorporated into the total stress. Unlike small amplitude oscillatory shear, decomposition of resulting stress into the elastic and viscous components is not very clear under LAOS. Cho et al.[43] suggested a method of decomposing the stress

response under LAOS. Their method is based on the symmetrical geometry of the Lissajous–Bowditch curves. It was further improved by Yu et al.[44] It can be expressed by a Fourier series,[17] given by

$$\sigma(\gamma_0, \omega, t) = \sum_{n=1,3,\cdots} \left[a_n \cos(\omega_n t) + b_n \sin(\omega_n t) \right] \tag{5.6}$$

where $\omega_n (= 2\pi n)$ is the angular frequency, and a_n and b_n are the Fourier coefficients of the n^{th} harmonic, which relate the applied strain deformation to the stress response as

$$\begin{aligned} a_n &= \frac{2}{T}\int_0^T \sigma(t)\cos(2\pi n t)\,dt \\ b_n &= \frac{2}{T}\int_0^T \sigma(t)\sin(2\pi n t)\,dt \end{aligned} \tag{5.7}$$

Equation 5.6 suggests that only the odd harmonics are included in describing the stress response. Therefore, the nonlinear contributions are captured in the higher-order odd harmonics. This occurs because the resulting stress has odd symmetry with respect to the directionality of shear strain or strain rate.[45] FT-rheology is a powerful tool for studying the nonlinear viscoelastic properties of the materials because it can detect even a small signal of higher harmonics. The main advantage of using FT-rheology is that the stress response in LAOS can be expressed as a linear combination of σ' and σ''. It is a linear algebraic analysis method in which σ' and σ'' can be expressed as the orthogonal set of sines and cosines of different frequencies. For the first harmonic (i.e. n = 1), Equation 5.6 reduces to the linear viscoelastic regime (i.e. Equation 5.5) with $a_1 = \gamma_0 G''$ and $b_1 = \gamma_0 G'$. The intensity of the n^{th} harmonic is defined as

$$I_n = \sqrt{a_n^2 + b_n^2} \tag{5.8}$$

In addition to I_n, the relative intensity with respect to the first harmonic is an important parameter that provides useful information about the contribution of the higher harmonics in the nonlinear regime. It is defined as

$$I_{n/1} = \sqrt{\frac{a_n^2 + b_n^2}{a_1^2 + b_1^2}} \tag{5.9}$$

When foam is deformed at sufficiently high amplitudes, higher harmonic terms are observed. This makes the system complex. To avoid such complexity, the time-domain stress-response is converted into frequency-domain by using the FT method. The discrete FT of stress data can be computed as

$$F_n = \sum_{k=0}^{N-1} \sigma_k \exp\left(-2\pi i n k / N\right) \tag{5.10}$$

where $k = 0, 1, 2, \ldots, (N–1)$, N is the total number of experimental data points in the shear stress response, and i is the imaginary unit. F_n represents a signal of the n^{th} harmonic term in the frequency domain of the stress-response. Since F_n is a complex number, it can be expressed by its amplitude.

FT-rheology is a sensitive approach, which determines the amplitude and phase difference of higher harmonics, and may provide useful insights about the progressive transition from linear to nonlinear viscoelastic responses.[17] However, this approach is not able to elucidate the clear physical interpretation of all the higher harmonic coefficients except the fundamental harmonic.[46] Therefore, to avoid these ambiguities, a cycle-by-cycle measurement of the stress response as a function of shear strain (or strain

rate) is preferred. A graphical representation of a closed-loop plot of the stress response $\sigma(\gamma_0,\omega,t)$ vs. $\gamma(t)$ [or $\dot{\gamma}(t)$] is termed as *elastic (or viscous) Lissajous–Bowditch curve*. This representation is more convenient for the qualitative analysis of the viscoelastic behavior under LAOS. The elastic and viscous Lissajous–Bowditch curves can be used for decomposing the total shear stress into their elastic and viscous counterparts, respectively, as shown below.[43,44]

$$\sigma\left(\gamma,\frac{\dot{\gamma}}{\omega}\right)=\frac{\sigma\left(\gamma,\frac{\dot{\gamma}}{\omega}\right)+\sigma\left(\gamma,-\frac{\dot{\gamma}}{\omega}\right)}{2}+\frac{\sigma\left(\gamma,\frac{\dot{\gamma}}{\omega}\right)+\sigma\left(-\gamma,\frac{\dot{\gamma}}{\omega}\right)}{2} \tag{5.11}$$

σ' at a fixed γ is given by the average of the stress responses obtained during the positive and negative strain rates. Similarly, σ'' at a fixed $\dot{\gamma}$ is obtained by taking the average of the shear stress responses at the same magnitude (but opposite signs) of γ.

Ewoldt et al.[21] used the Chebyshev polynomials of the first kind, T_m, to decompose the total stress response in a cycle into their elastic and viscous components. Chebyshev polynomials are defined as $T_m(x)=\cos m\theta$, where $x=\cos\theta$. The recurrence relation of the Chebyshev polynomials is given by[47]

$$T_m(x)=2xT_{m-1}(x)-T_{m-2}(x),\quad m=2,3,\cdots \tag{5.12}$$

This, together with the initial conditions, $T_0(x)=1$ and $T_1(x)=x$, recursively generates all the polynomials $\{T_m(x)\}$ easily. These polynomials are orthogonal over the interval [–1, 1]. Like the FT-rheology approach, the Chebyshev polynomial approach can be utilized in finding the elastic and viscous components of the stress response, given by

$$\sigma' = \gamma_0 \sum_{m\ \text{odd}} e_m(\omega,\gamma_0) T_m(\gamma)$$
$$\sigma'' = \dot{\gamma}_0 \sum_{m\ \text{odd}} v_m(\omega,\gamma_0) T_m\left(\frac{\dot{\gamma}}{\omega}\right), \qquad m = 2,3,\cdots \tag{5.13}$$

where e_m and v_m are the elastic and viscous Chebyshev coefficients of order *m*. Based on these coefficients, the materials can be characterized as intracycle strain-hardening $(e_3 > 1)$, strain-softening $(e_3 < 1)$, shear-thickening $(v_3 > 1)$, and shear-thinning $(v_3 < 1)$. The Chebyshev coefficients can be utilized to derive the following geometrically-motivated moduli.

$$G'_M \equiv \left.\frac{d\sigma}{d\gamma}\right|_{\gamma=0} = \frac{1}{\gamma_0} \sum_{n\ \text{odd}} n b_n = e_1 - 3e_3 + \cdots \tag{5.14}$$

$$G'_L = \left.\frac{\sigma}{\gamma}\right|_{\gamma=\pm\gamma_0} = \sum_{n\ \text{odd}} b_n (-1)^{(n-1)/2} = e_1 + e_3 + \cdots \tag{5.15}$$

where G'_M is the minimum-strain amplitude at $\gamma = 0$, and G'_L is the large-strain amplitude at $\gamma = \gamma_0$. For the linear viscoelastic regime, both G'_M and G'_L are equivalent to G'. Therefore, this approach of characterizing materials can be considered as more general. However, like FT-rheology, the Chebyshev approach also has limitations when it includes the contribution of the higher harmonic terms above the third. This limitation arises due to the symmetry assumptions for decomposing the total nonlinear stress response into the superposition of an elastic stress and a viscous stress[46,48] (see Equation 5.11). Rogers and Lettinga[26] have shown that the physical interpretation of these approaches may vary from one material to another, although they are valuable approaches mathematically.

To interpret the LAOS behavior of a material by using a Lissajous–Bowditch curve, Rogers et al.[34] have proposed an approach based on a sequence of physical processes. It includes elastic straining, yielding behavior, and flow behavior. The elastic straining during intracycle shearing can be described by the apparent cage modulus $\left(G_{cage}\right)$, which can be defined as the derivative of the stress with respect to strain at zero stress.

$$G_{cage} = \left.\frac{d\sigma}{d\gamma}\right|_{\sigma=0} \tag{5.16}$$

It is the instantaneous slope of the elastic Lissajous–Bowditch curve at zero stress.

5.3 Results and discussion

Before probing the nonlinear viscoelastic behavior of foam, we performed a few other fundamental experiments on foam as shown in Figure 5.1. The results from a typical amplitude sweep experiment on foam are shown in Figure 5.1a. This experiment can be used for determining the linear and nonlinear viscoelastic regimes under oscillatory shear. At low strain up to 1%, both G' and G'' were independent of γ_0. This is known as the *linear viscoelastic regime*. Upon increasing γ_0 further (i.e. above critical strain amplitude), the foam started yielding. G' decreased continuously, indicating *strain-softening*. G'' initially increased, reached a local maximum at a certain value of γ_0, and then started decreasing. This characteristic is known as *weak strain overshoot*. The overshoot (i.e. the local maximum of G'') may be considered as the balance between the formation and destruction of the structure of foams.[13] The yield strain is usually considered at the crossover point of G' and G'' [49]. As the strain amplitude exceeded the

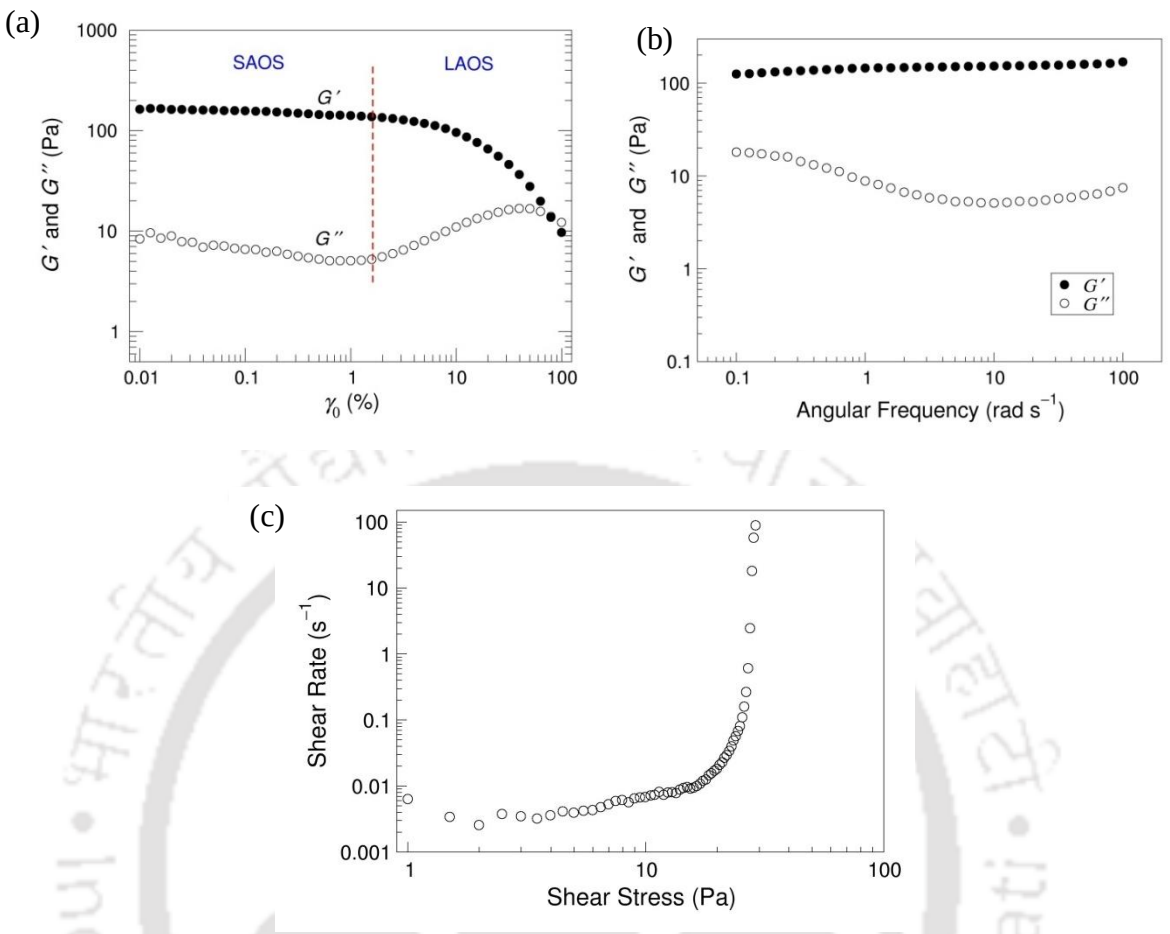

Figure 5.1 (a) Results from a typical amplitude sweep experiment at $\omega = 1$ rad s^{-1}, (b) frequency sweep experiment on foam at the constant strain amplitude of 0.5%, and (c) steady state flow curve of the foam.

yield point, both the moduli decreased (with $G'' > G'$) indicating the liquid-like behavior. Therefore, yielding can be considered as the transition of a material from solid-like to liquid-like behavior. The response of foam after 1% γ_0 is known as the *nonlinear viscoelastic regime*, where the LAOS experiment was performed.

G' and G'' are suitable rheological parameters for explaining the viscoelastic behavior in the linear viscoelastic regime, inasmuch as they contain only the first

harmonic contributions to the stress response. The intensities of other odd higher harmonics in medium amplitude oscillatory shear regions are very small. However, higher harmonic contributions must be added to distinguish and investigate the viscoelastic behavior at large γ_0. The linear viscoelastic moduli of the foam were plotted as a function of frequency in Figure 5.1b. These moduli were obtained at the constant strain amplitude of 0.5% because at this amplitude foam exhibited linear viscoelastic behavior (see Figure 5.1a). Additionally, G' was one order of magnitude higher than G'', and both the moduli were independent of the frequency of oscillation, which is a typical characteristic of gel-like behavior. The steady state flow curve of the foam is shown in Figure 5.1c. The shear rate was measured by varying the shear stress. It was observed that there was no flow below ~15 Pa shear stress because the shear rate was almost zero, which implies that the foam showed yield stress.

Because of the non-sinusoidal shape of the stress waveform, the complex shear modulus alone is not sufficient to characterize the foam behavior. Therefore, to investigate the nonlinear viscoelastic behavior of the foam, analysis of the stress response waveform can be useful. The waveform depends on the structure of foam. When foam was deformed under LAOS, the stress response was still periodic, and the stress curves changed their shape from sinusoidal to non-sinusoidal with increasing strain amplitude as shown in Figure 5.2. The asymmetry of the stress response was significant with increasing γ_0. A shape signifying "backward tilted stress" was observed under LAOS. The third harmonic term is mainly responsible for the non-sinusoidal shape of the

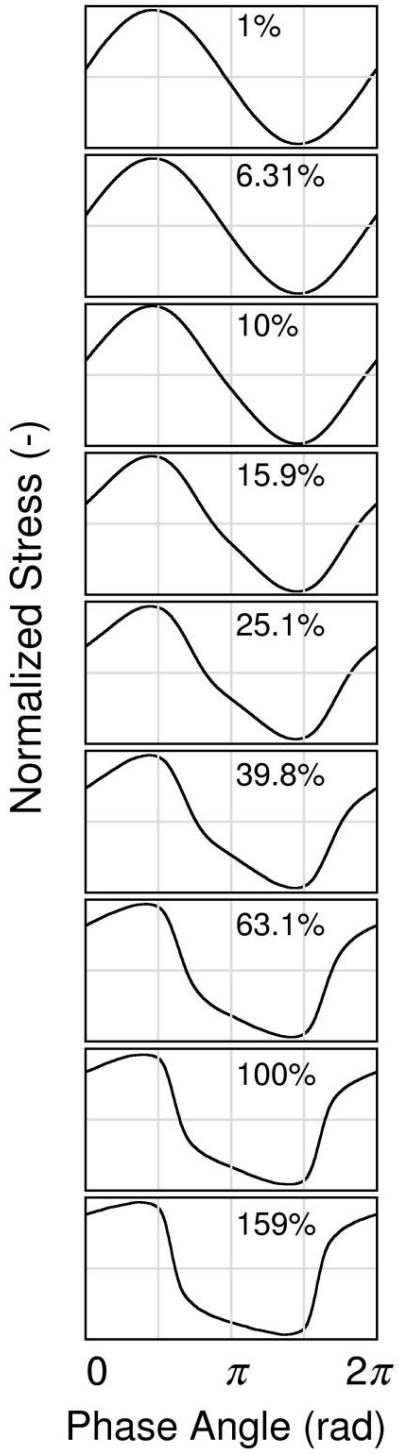

Figure 5.2 The waveform of the shear stress as a function of phase angle in a complete cycle. The shear stress results were obtained by imposing oscillatory shear strain at different amplitudes ranging from 1 to 159%.

waveform. The other higher harmonic terms typically decay rapidly. The effects of higher harmonic terms were also studied by using Fourier series, which are reported later in this section.

The elastic Lissajous–Bowditch curves of foam are shown in Figure 5.3. In the linear viscoelastic regime, the Lissajous–Bowditch curves were elliptic. The slope of the major axis of the ellipse represents the magnitude of the complex shear modulus. With increasing γ_0, the width of the minor axis of the ellipse became wider, which can be attributed to the phase angle between the input strain and the output stress.[50] Additionally, the shape of the Lissajous–Bowditch curves became increasingly rectangular with highly-rounded corners. This can be seen clearly in Figure 5.3 for $\gamma_0 > 39.8\%$. This shape implies that the greatest increase in stress occurred when the strain was maximum in a cycle. These increasingly rectangular elastic Lissajous–Bowditch curves confirm the intracycle strain-hardening process associated with the foam under LAOS. In the nonlinear viscoelastic regime, however, the shape of the Lissajous–Bowditch curves was more complex and non-ellipsoidal. Therefore, the simple viscoelastic moduli may not be appropriate to explain the real shape, and they may mislead the structural and physical information. The area enclosed by the elastic Lissajous–Bowditch curves increased with γ_0, which indicates an increase in the energy dissipated during the LAOS test.

The data suffered from noise at the high values of ω and low values of γ_0 (as shown in the right bottom portions in Figures 5.3 and 5.5). This may be due to the fact that at high ω, the experimental time was less than the time required for the foam to

relax. The stress amplitude increased with increasing ω. However, the shape of the Lissajous–Bowditch curves remained almost unchanged. A progressive transition from linear to nonlinear behavior can be observed from the elastic Lissajous–Bowditch curves. The onset of nonlinearity of the foam can be visually observed for strain above 10%, as the shape of the Lissajous–Bowditch curve (or the stress response waveform) started changing at this point onward. The corresponding viscous Lissajous–Bowditch curves have been shown in Figure 5.4. These curves showed sigmoid shape under LAOS, which confirmed the intracycle shear-thinning behavior.[51]

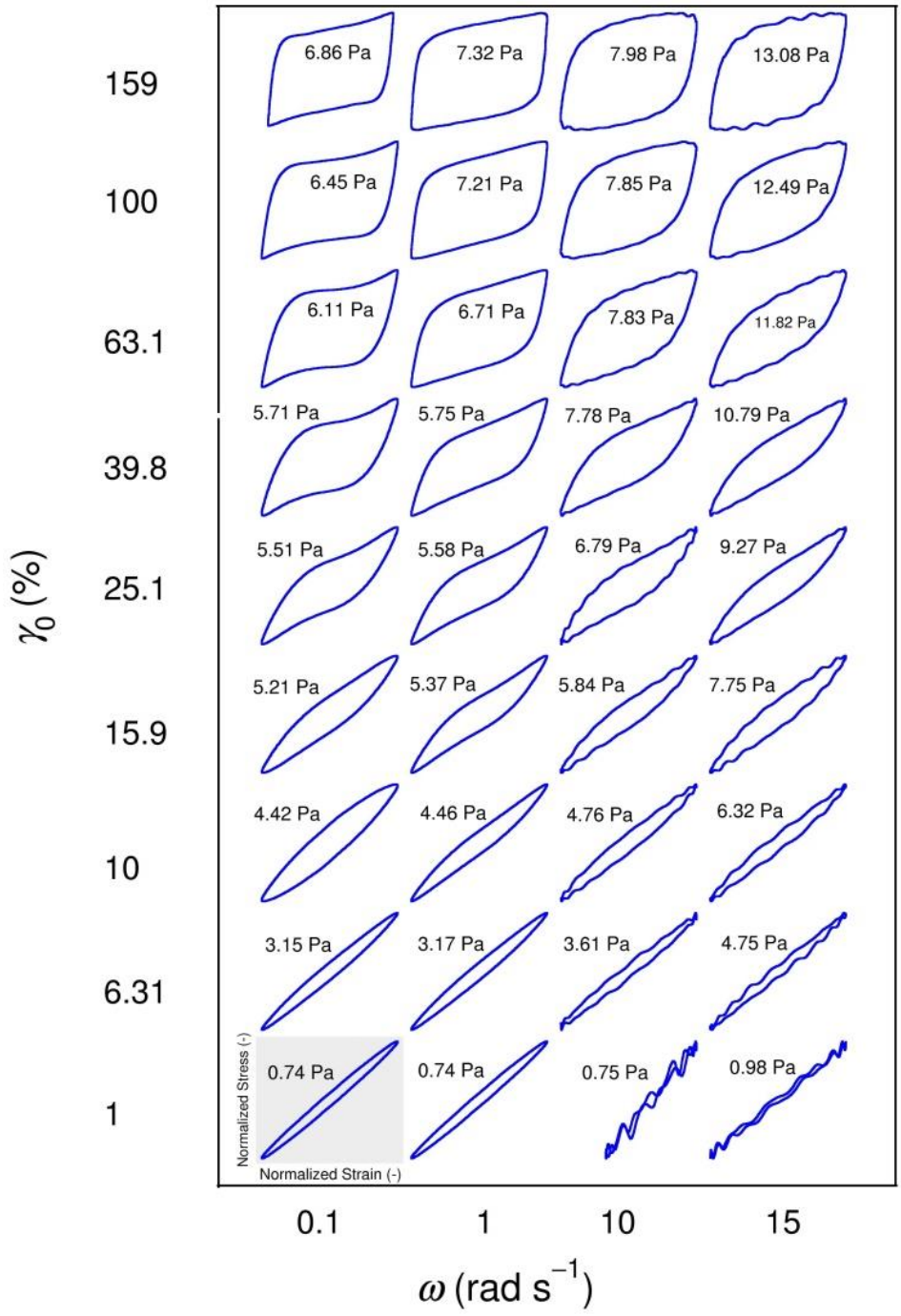

Figure 5.3 Elastic Lissajous–Bowditch curves [normalized stress, $\sigma(t)/\sigma_0$ vs. normalized strain, $\gamma(t)/\gamma_0$]. The amplitude of shear stress (σ_0) is indicated in each curve. All curves are two-dimensional projections of the three-dimensional curves on the stress–strain plane.

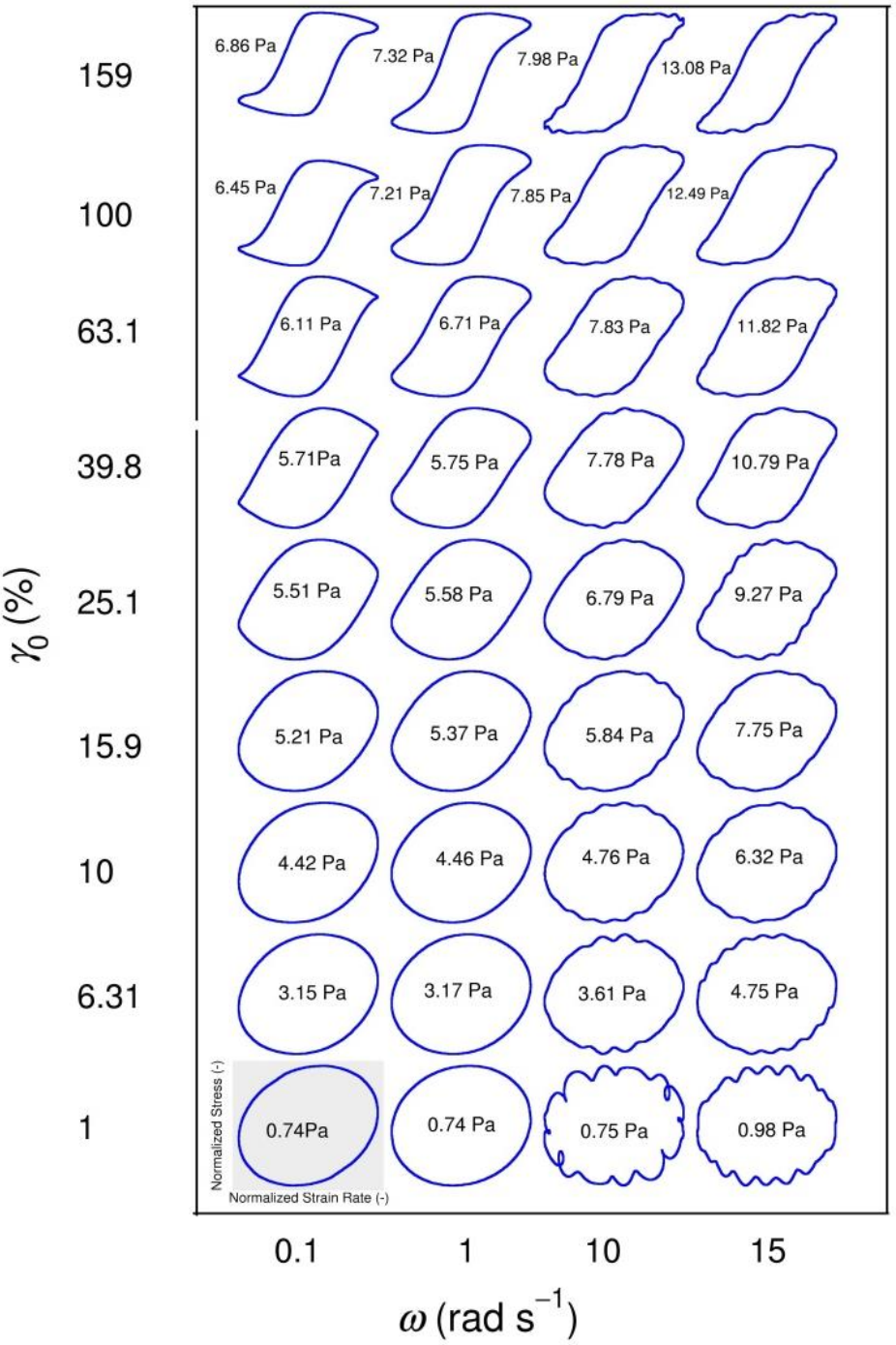

Figure 5.4 Viscous Lissajous–Bowditch curves [normalized stress, $\sigma(t)/\sigma_0$ vs. normalized strain rate, $\dot{\gamma}(t)/\dot{\gamma}_0$]. The amplitude of shear stress (σ_0) is indicated in each curve. All curves are two-dimensional projections of the three-dimensional curves on the stress–strain rate plane.

The instantaneous viscosity of the foam can be found from the slope of the viscous Lissajous–Bowditch curves. The instantaneous viscosity decreased with increasing deformation rate. Therefore, the foam showed intracycle shear-thinning behavior. The 3D curves of the Lissajous–Bowditch plots are shown at different projection angles in Figure 5.5. We have also compared our experimental results with the oscillatory stress response obtained from the cone-and-plate geometry, where homogeneous deformation can be achieved (see Annexure A).

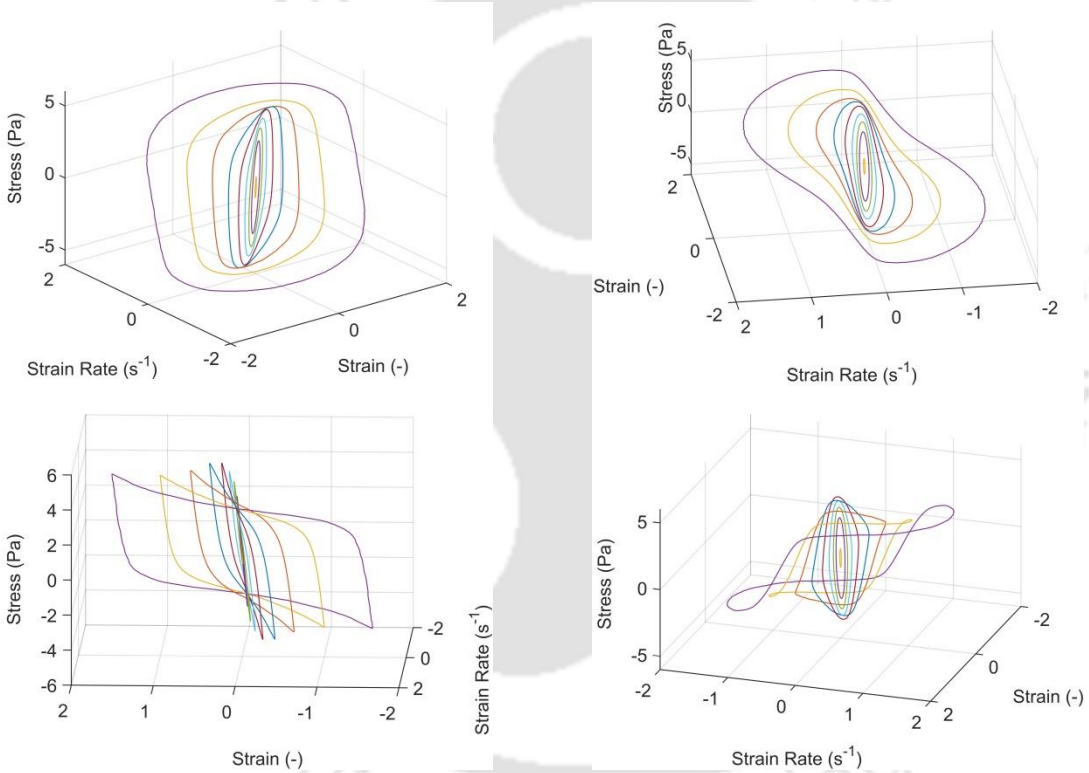

Figure 5.5 Three-dimensional representation of the Lissajous–Bowditch curves where stress, strain, and strain rate are considered as orthogonal coordinate axes. The curves are shown at $\omega = 1$ rad s^{-1} for different strain amplitudes (γ_0) (i.e. 1, 6.31, 10, 15.9, 25.1, 39.8, 63.1, 100, and 159%). The Lissajous–Bowditch curves are shown at different projection angles.

The elastic component of the total stress showed the linear dependency on strain at low γ_0. The stress–strain curve was bent upward at large strains, as shown in Figure 5.6. This shape is often considered as an indication of strain-hardening.[52] In contrary, the amplitude sweep experiment showed strain-softening of the foam (Figure 5.1). This paradox has been reported recently by Mermet-Guyennet et al.[53] They concluded that the strain-hardening was due to the use of G'_M. However, the overall LAOS behavior indicated strain-softening. To investigate further on the nonlinear viscoelastic behavior of foam, we adopted the approach of sequence of physical processes proposed by Rogers et al.[34] This approach provides a framework to analyze the intracycle response of the elastic Lissajous–Bowditch curves by decomposing it into the sequence of physical

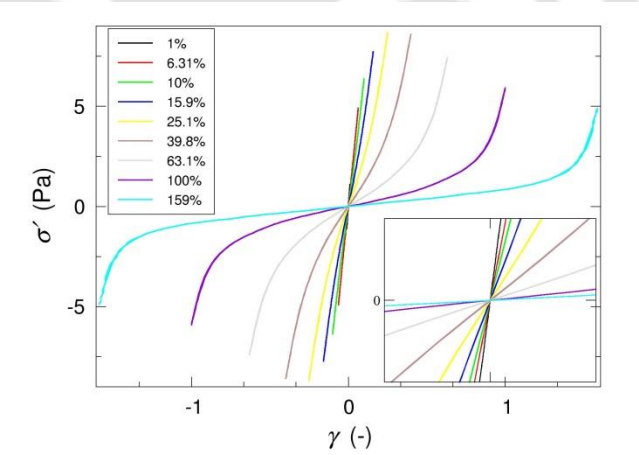

Figure 5.6 The elastic components of the shear stress response (obtained from Figure 5.3) as a function of strain in one period of oscillation. The experiment was performed at $\omega = 1$ rad s^{-1} for different strain amplitudes (γ_0) ranging from 1 to 159%.

processes, i.e. elastic straining, yielding behavior, and flow behavior. Figure 5.7 shows the G_{cage} (determined from Equation 5.16) and G' (see Figure 5.1a) as a function of γ_0. Both the moduli overlap in the linear viscoelastic regime indicating that the foam extended in a linear fashion. The G' decreased with increasing strain amplitude, but G_{cage} did not change significantly and remained significantly above the G', even at the higher amplitudes. This indicates that the foam exhibited an elastic deformation. It also suggests that the foam behavior was explained well by the sequence of physical processes.[54]

In addition, the elastic straining can be illustrated more clearly from the elastic Lissajous–Bowditch curves as shown in Figure 5.7b. At the strain reversal point (i.e. maximum strain or zero strain rate), the stress increased almost linearly with strain up to the critical strain, which implies the elastic behavior of foam. Further increasing the strain above the critical point, the stress continued to increase until a yield stress was achieved, where it showed an overshoot (or a local maxima) (see the top left curves of Figure 5.3). The yielding behavior can be characterized from Figure 5.7b by determining the total strain required from the lower reversal point (unfilled circles) to the point of maximum elastic stress (triangles) and maximum total stress (filled circles). These accumulated strains are shown in Figure 5.7c as a function of γ_0. For an ideal elastic solid, the amount of strain required to achieve the maximum total stress is $2\gamma_0$, whereas it is γ_0 for the ideal viscous liquid. The idealized behavior of elastic solid and viscous liquid are represented by the solid and dashed lines, respectively (see Figure 5.7c).

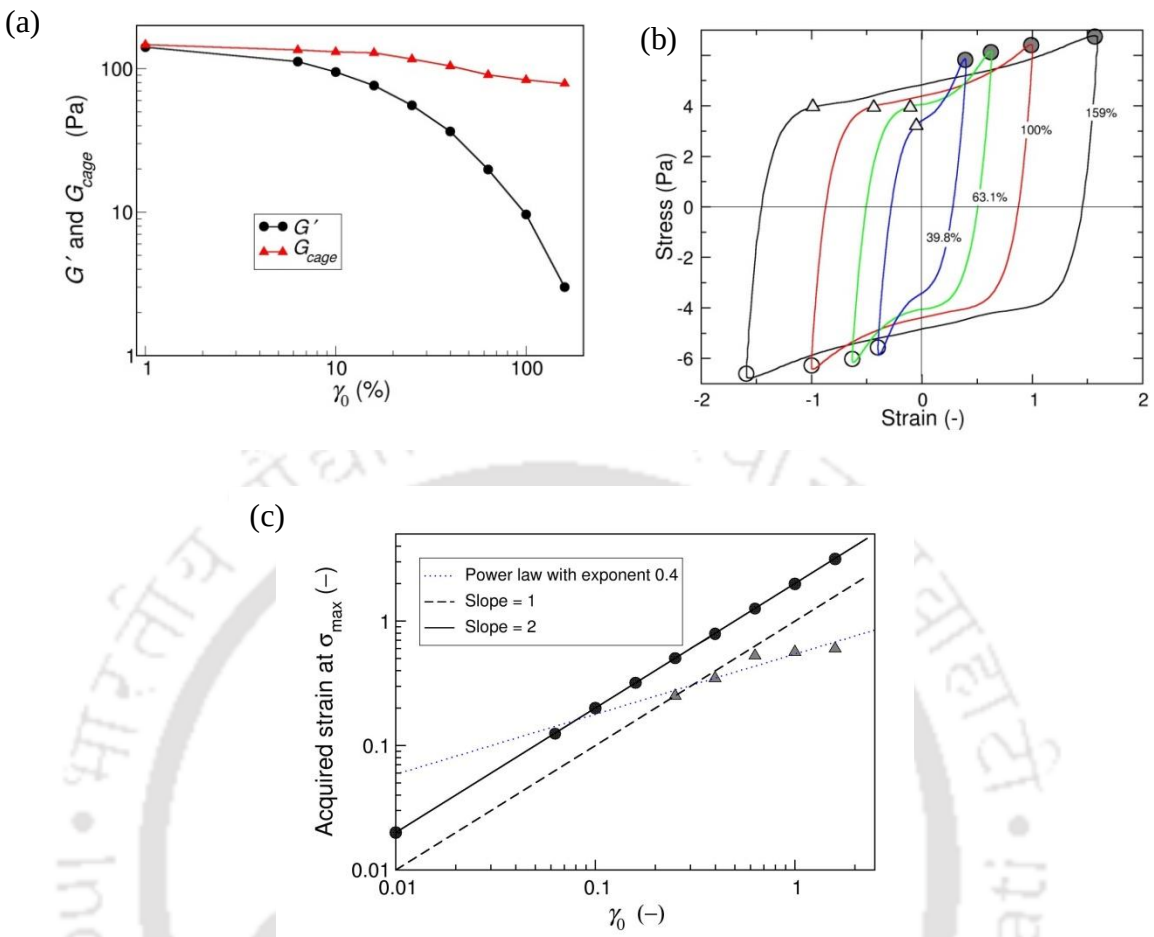

Figure 5.7 (a) Storage modulus (G') and apparent cage modulus (G_{cage}) as a function of strain amplitude (γ_0). (b) The elastic Lissajous–Bowditch curves of the foam at the selected strain amplitudes under LAOS. The empty circles indicate the lower reversal points, triangles represent the maximum elastic points (i.e. stress overshoot), and filled circles indicate the points of maximum total stress. (c) The strain required from the lower reversal point to the point of maximum total stress (circles) and maximum elastic stress (triangles) as a function of strain amplitude. Idealized behavior of elastic solid and viscous liquid are represented by solid and dashed lines, respectively. The strain required to reach the maximum elastic point follows the power law with index 0.4.

The data points corresponding to the maximum total stress followed a straight line with slope 2. This implies that the maximum total stress was the result of an elastic process. Therefore, the foam structure reformed after the strain corresponding to the maximum total stress by releasing the elastic stress. On the other hand, the maximum elastic stress initially followed a straight line with slope 1, indicating that the stress was caused by a viscous process. The data points deviated at large amplitudes, and they followed the power-law behavior with flow index 0.4. This confirms the shear-thinning flow behavior of foam above the yield stress. van der Vaart et al.[55] observed similar type of results for a concentrated soft-sphere suspension. However, for the hard-sphere suspension, the acquired strain to maximum total stress followed perfect solid-like and liquid-like behaviors at low and high γ_0, respectively.[34,55] The flow behavior above the yield strain was initially characterized as viscoplastic because the stress remained almost constant, and then it increased abruptly with strain indicating strain-hardening behavior. This sequence of physical processes was repeated in the remaining half-cycle of the oscillation.

One aspect of studying the yielding behavior is the appearance of significant non-linearity. From the elastic Lissajous–Bowditch curves under LAOS at higher frequency (see the top right curves of Figure 5.3), it appears that the foam exhibited plastic and/or elastoplastic flow beyond the yield strain. To deal with such flow behavior in a cyclic deformation, the concept of kinematic hardening is widely used.[56,57] This concept describes the stress–strain relationship for yielding materials. Dimitriou et al.[58] have developed a method to understand the kinematic hardening from the Lissajous–Bowditch curves. Their method is based on the elastic Herschel–Bulkley model. In this method, the

strain at a point on the elastic Lissajous–Bowditch curve can be decomposed into elastic $\left(\gamma^e\right)$ and plastic $\left(\gamma^p\right)$ components as

$$\gamma = \gamma^e + \gamma^p \tag{5.17}$$

The stress is related to γ^e through the Young's modulus (G) as $\sigma = G\gamma^e$, and the elastic strain retains beyond the yield point. The contribution to the stress due to plastic flow is called *back stress* $\left(\sigma_{back}\right)$. The plastic flow rate $\left(\dot{\gamma}^p\right)$ is related to the effective stress (i.e. $\left|\sigma - \sigma_{back}\right|$), which is the driving force for the plastic flow. It is given by[58]

$$\dot{\gamma}^p = n^p \left[\frac{\left|\sigma - \sigma_{back}\right|}{k}\right]^{1/q} \tag{5.18}$$

where n^p is the direction of plastic flow, and k and q are the *consistency index* and the *flow index*, respectively. Below the yield strain, it is assumed that $\dot{\gamma}^p$ is zero, and the foam undergoes only elastic deformation. However, above the yield strain, the rate-independent plastic flow begins to occur. This is immediately followed by strain-hardening at low frequency and kinematic hardening at high frequency. At the strain reversal point, the elastic strain is recovered and the cycle is repeated by dropping the stress below their yield value.

Equations 5.6 and 5.13 show the relation between the FT-rheology and the Chebyshev polynomial approaches. Both the approaches are based on linear algebraic analysis, where the elastic and viscous components of the total stress response can be expressed as a linear combination of the finite orthogonal basis sets. In the FT-rheology

approach, σ' and σ'' are expressed as the linear combination of the orthogonal sets of sines and cosines, respectively, of different higher odd harmonic frequencies. In the Chebyshev polynomial approach, σ' and σ'' are expressed as the linear combination of the orthogonal sets of Chebyshev polynomials of different higher odd orders. The FT-rheology approach is not able to elucidate the physical interpretation of all the higher harmonic coefficients except the fundamental harmonic. However, the Chebyshev approach can be used to interpret the LAOS results within a cycle by using the first and third Chebyshev coefficients. Like the FT approach, the first Chebyshev coefficient explains the linear viscoelastic behavior. The elastic and viscous components of the total shear stress obtained from the corresponding Lissajous–Bowditch curves are shown in Figure 5.8. These stress components were obtained by taking the average of the shear stresses during the positive and negative $\dot{\gamma}$ (or γ) at a fixed γ (or $\dot{\gamma}$). This method of decomposing the stress response was proposed by Cho et al.,[43] and it is useful for analyzing the viscoelastic properties of foam under LAOS. Furthermore, these stress components were fitted by Chebyshev polynomials. As can be seen from Figure 5.8a, when foam was deformed in the linear viscoelastic regime (i.e. at 1% γ_0), σ' increased linearly with γ, and σ'' was almost independent of $\dot{\gamma}$. This implies that the foam showed a predominantly elastic behavior. Also, due to the linear viscoelastic properties, the first-degree Chebyshev polynomial was alone sufficient to fit the stress components. The linearity can also be confirmed from the Chebyshev coefficients, inasmuch as both e_3 and v_3 were zero. Upon further increasing γ_0 to 25%, it was found that the σ' and σ''

(a)

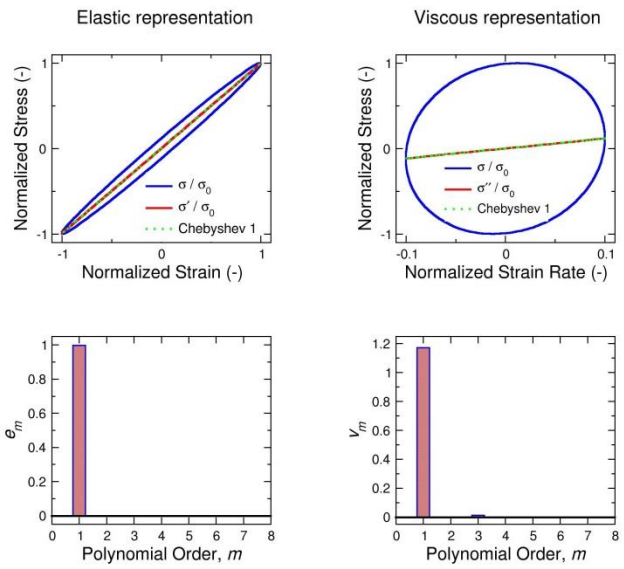

(b)

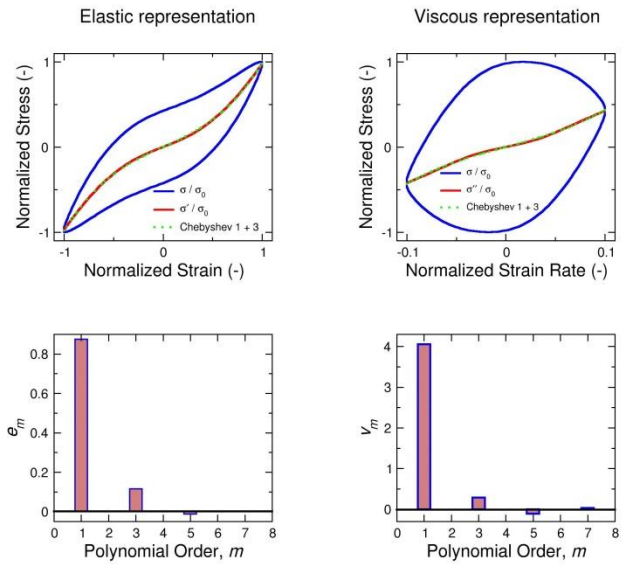

(c)

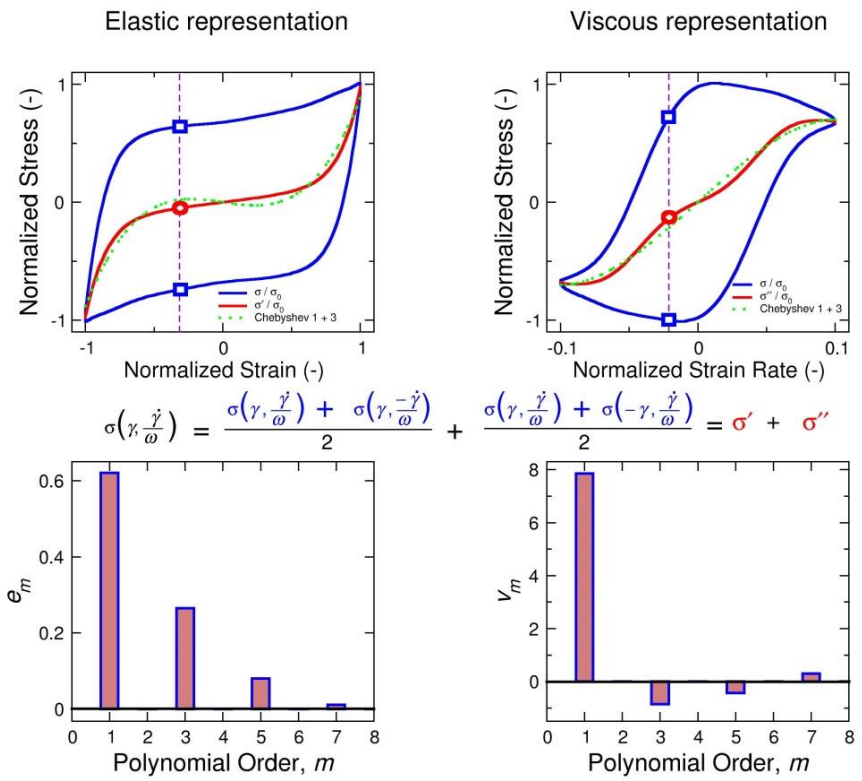

Figure 5.8 Decomposition of the normalized stress response $\left[\sigma(t)/\sigma_0\right]$ into the elastic $\left[\sigma'(t)/\sigma_0\right]$ and viscous $\left[\sigma''(t)/\sigma_0\right]$ components, based on the geometrical method (i.e. Equation 5.11). These components were fitted by the Chebyshev polynomials of odd orders. The elastic (i.e. e_m) and viscous (i.e. v_m) Chebyshev coefficients are shown corresponding to the order of the Chebyshev polynomial: (a) γ_0 = 1%, (b) γ_0 = 25%, and (c) γ_0 = 100%. The geometrical decomposition method is depicted in the figure.

components were not linearly dependent on γ and $\dot{\gamma}$, respectively. Therefore, third-order Chebyshev polynomials were used to fit the stress components. Both e_3 and v_3 were positive, which implies that the foam showed strain-hardening and shear-thickening

behavior. At very high γ_0 (e.g. 100%), a sudden rise in σ' was observed at large γ, which reflects that the foam was stiff. A positive value of e_3 confirms the intracycle strain-hardening behavior. In contrast, the slope of the σ'' vs. $\dot{\gamma}$ curve decreased, and v_3 was negative. Therefore, the foam showed an intracycle shear-thinning behavior.

Figure 5.9 clearly shows the contribution of the higher harmonic terms under the LAOS response. The solid line shows the experimental stress response, and the dashed line depicts the stress obtained from the Fourier series (i.e. Equation 5.6). The Fourier coefficients (i.e. a_n and b_n) were computed from Equation 5.7. These are shown in the corresponding figures. When foam was deformed at low γ_0 (up to ~6.31%), only the first harmonic term was sufficient to fit the stress response waveforms. With increasing γ_0, higher odd harmonic terms were required. Therefore, the third harmonic term, along with the first term, fitted the stress waveform (up to 25.1%). Further increasing γ_0, the fifth-term was required, and it was added to fit the stress response waveforms. It was observed that the even terms did not make any contribution to LAOS. It reconfirmed the absence of the slip condition between the two parallel plates, where the foam was placed. Each peak in Figure 5.9 in the first column represents the magnitude of the corresponding harmonic terms. This is known as the *FT-rheology spectrum*. These peaks were determined by discrete FT of stress data using Equation 5.10. From the figure, it is clearly seen that the number of higher harmonic contributions and the magnitude of the peaks at odd harmonics increased with applied γ_0. The computer program for curve fitting of the stress waveforms by Fourier series is shown in Annexure B. Computation of their discrete Fourier transform is shown in Annexure C.

1%

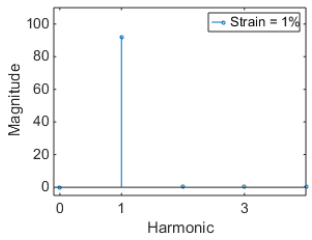

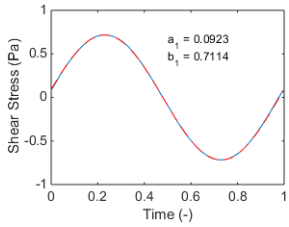

6.31%

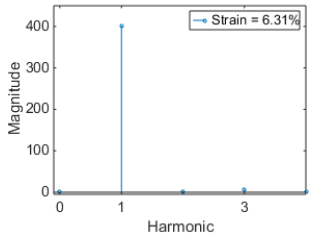

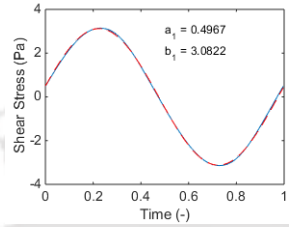

10%

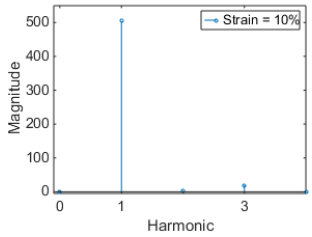

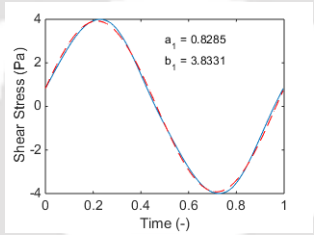

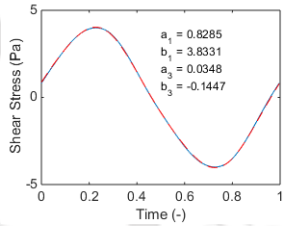

15.9%

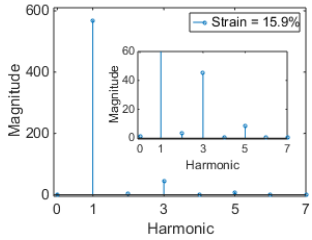

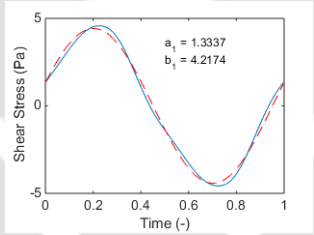

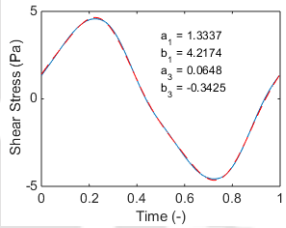

25.1%

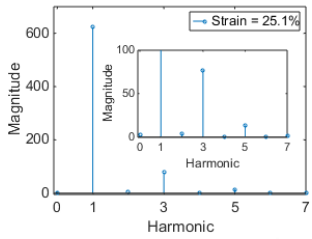

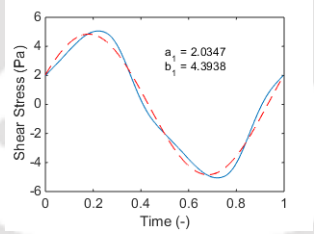

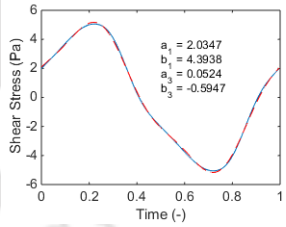

39.8%

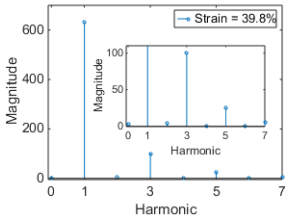

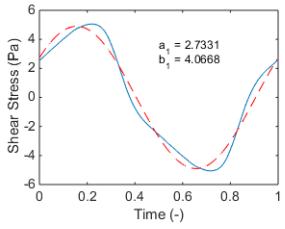

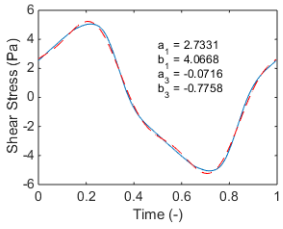

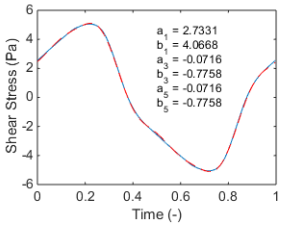

63.1%

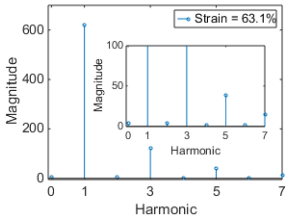

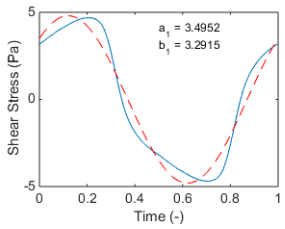

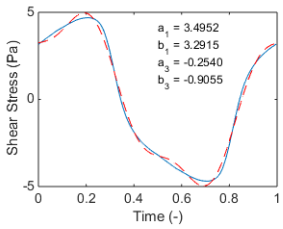

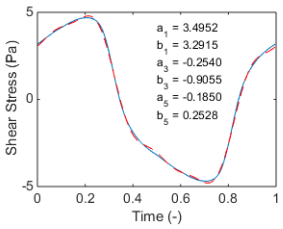

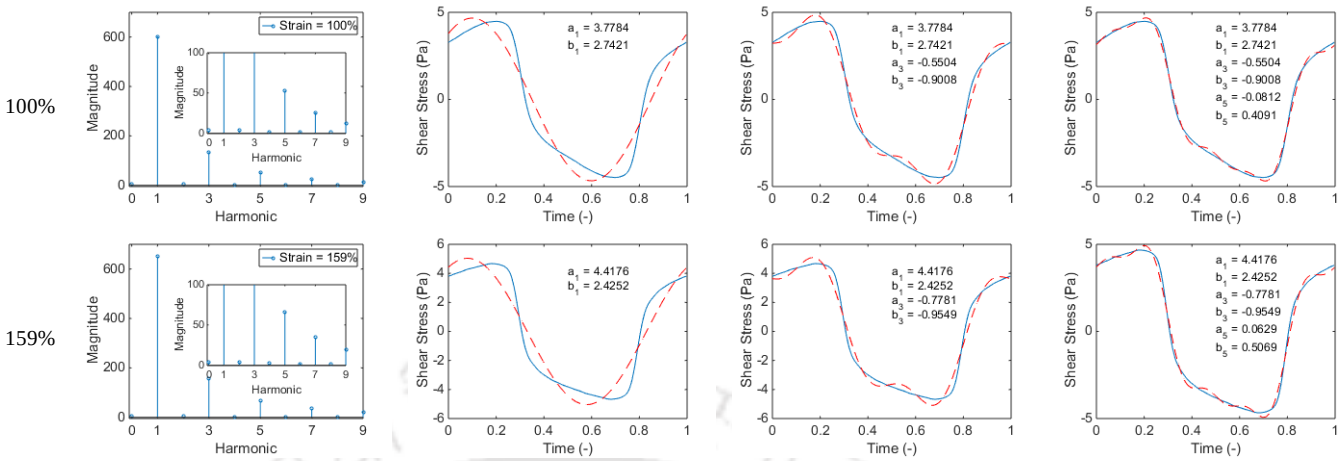

Figure 5.9 Contribution of different oscillatory harmonic terms on the LAOS response. Each signal shows the magnitude of the corresponding harmonic. The inset (above 15.9%) shows the same graph, which was magnified to observe the signals corresponding to the higher harmonic terms. The stress response curves (Figure 5.2) were fitted by Fourier series (the dashed line). The FT parameters (i.e. a_n and b_n) obtained from Equation 5.7 are shown in the figure.

The nonlinearity was quantified by determining the relative intensities of the higher harmonic terms with respect to the first (i.e. fundamental) harmonic (e.g. $I_{3/1}$ and $I_{5/1}$), as shown in Figure 5.10. $I_{3/1}$ increased linearly with increasing γ_0 (up to ~25%). With further increase in γ_0, $I_{3/1}$ increased slowly. This may be due to the presence of the third harmonic term. $I_{5/1}$ increased linearly up to 100% γ_0. The contribution of the higher harmonic terms became significant when the foam was deformed at high γ_0. When $\ln(I_{3/1})$ was plotted against $\ln(\gamma_0)$, a straight line with slope ~2 was obtained in the low-to-medium γ_0 range, as shown in Figure 5.10. This indicates a scaling relationship between $I_{3/1}$ and γ_0.[59,60] At low-to-medium shear deformation, $I_{3/1}$ of the

(a)

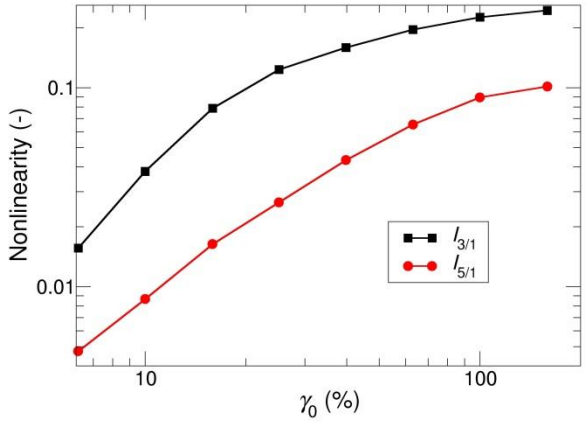

(b)

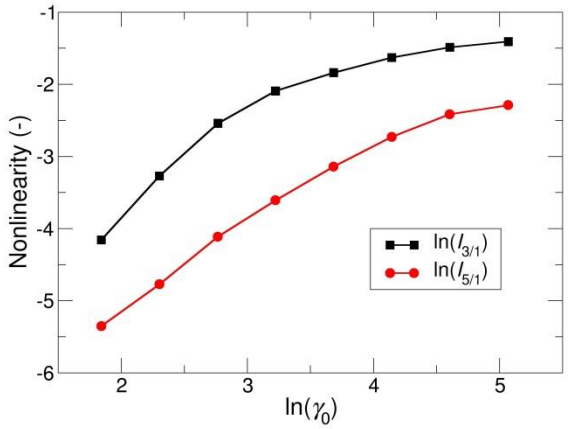

Figure 5.10 (a) Relative intensity of the third harmonic $\left(I_{3/1}\right)$ and fifth harmonic $\left(I_{5/1}\right)$ expressed as a function of the shear strain amplitude $\left(\gamma_0\right)$ (i.e. Equation 5.9). (b) $I_{3/1}$ and $I_{5/1}$ computed by taking logarithm of the data in Figure 5.10a. The experiment was performed by applying an oscillatory shear at $\omega = 1$ rad s^{-1}.

foam varied quadratically with γ_0. A similar result was observed for beer foams.[61] The third harmonic is the best scaling corresponding to the scaling theory at the small

amplitude. An asymptotic behavior to a plateau value was observed at high γ_0. Therefore, the scaling theory is not suitable for the relative intensity higher than the third harmonic. However, an attempt was made to extend the scaling law for $I_{5/1}$. It was found that it varied linearly over a wide range of γ_0, as shown in Figure 5.10.

5.4 Conclusions

Nonlinear viscoelastic behavior of foam stabilized by HTAB and silica nanoparticles was systematically studied under LAOS by using Lissajous–Bowditch curves, FT-rheology analysis, and the Chebyshev polynomial technique. The LAOS results were interpreted based on the sequence of physical processes. With increasing γ_0, the shape of the waveforms and the Lissajous–Bowditch curves changed. Elastic Lissajous–Bowditch curves changed from ellipsoidal to rectangular, which shows the strain-hardening behavior of foam. However, the overall behavior was shear-thinning. Flow under LAOS was periodic, and it involved the contributions of the higher odd harmonic terms to the stress response. The peaks corresponding to the even harmonic oscillatory terms were not observed, which may be due to the "no slip" condition between the parallel plates, where the foam was placed during the LAOS test. The foam showed linear elastic response in the linear viscoelastic regime inasmuch as e_3 was zero. Intracycle strain-hardening behavior was observed in the nonlinear viscoelastic regime inasmuch as e_3 was positive. Furthermore, it showed linear viscous response in the linear viscoelastic regime (inasmuch as v_3 was zero), intracycle shear-thickening at moderate γ_0 (inasmuch as v_3 was positive), and intracycle shear-thinning at high γ_0 (inasmuch as v_3 was negative). It

was also observed that $I_{3/1}$ was quadratically dependent on γ_0 at low-to-intermediate shear deformation. However, $I_{5/1}$ varied linearly over a wide range of γ_0. G'_L was greater than G'_M in the entire range of amplitude and frequency of oscillation under LAOS, which also confirmed the strain-hardening behavior of foam. The sequence of physical processes revealed that the foam exhibited elastic straining at the strain reversion point and showed yielding above the critical strain, which was followed by strain-hardening. It also showed kinematic hardening at high frequency under the LAOS flow.

Nomenclature

a_n	Fourier cosine coefficient of the n^{th} harmonic, Pa
b_n	Fourier sine coefficient of the n^{th} harmonic, Pa
e_m	elastic Chebyshev coefficient of order m
F_n	discrete FT of the n^{th} harmonic, Pa
G	Young's modulus, Pa
G'	storage modulus, Pa
G''	loss modulus, Pa
G_{cage}	cage modulus, Pa
G'_L	large-strain amplitude, Pa
G'_M	minimum-strain amplitude, Pa
i	imaginary unit
I_n	intensity of n^{th} harmonic, Pa

$I_{n/1}$	relative intensity of n^{th} harmonic
k	consistency index
m	order of Chebyshev polynomial of the first kind
n	harmonic
n^p	direction of plastic flow
N	total number of data points
q	flow index
t	time, s
T	time period, s
T_m	Chebyshev polynomial of the first kind
v_m	viscous Chebyshev coefficient of order m

Greek letters

γ	shear strain
$\dot{\gamma}$	strain rate, s^{-1}
$\dot{\gamma}^p$	plastic flow rate, s^{-1}
γ_0	strain amplitude
γ^e	elastic strain
γ^p	plastic strain
δ	phase angle, rad
σ	shear stress, Pa
σ'	in-phase shear stress component, Pa

σ''	out-of-phase shear stress component, Pa
σ_{back}	back stress, Pa
σ_0	stress amplitude, Pa
ω	angular frequency, rad s^{-1}

Abbreviations

CMC	critical micelle concentration
FT	Fourier transform
HTAB	hexadecyltrymethylammonium bromide
LAOS	large amplitude oscillatory shear

References

(1) Denkov, N. D.; Tcholakova, S.; Golemanov, K.; Ananthpadmanabhan, K. P.; Lips, A. The Role of Surfactant Type and Bubble Surface Mobility in Foam Rheology. *Soft Matter* **2009,** *5*, 3389–3408.

(2) Höhler, R.; Cohen-Addad, S. Rheology of Liquid Foam. *J. Phys.: Condens. Matter* **2005,** *17*, 1041–1069.

(3) Dickinson, E. Structuring of Colloidal Particles at Interfaces and the Relationship to Food Emulsion and Foam Stability. *J. Colloid Interface Sci.* **2015,** *449*, 38–45.

(4) Ahmadi, Y.; Eshraghi, S. E.; Bahrami, P.; Hasanbeygi, M.; Kazemzadeh, Y.; Vahedian, A. Comprehensive Water-Alternating-Gas (WAG) Injection Study to Evaluate the Most Effective Method based on Heavy Oil Recovery and Asphaltene Precipitation Tests. *J. Pet. Sci. Eng.* **2015,** *133*, 123–129.

(5) Labiausse, V.; Hohler, R.; Cohen-Addad, S. Shear Induced Normal Stress Differences in Aqueous Foams. *J. Rheol.* **2007,** *51*, 479–492.

(6) Balmforth, N. J.; Frigaard, I. A.; Ovarlez, G. Yielding to Stress: Recent Developments in Viscoplastic Fluid Mechanics. *Annu. Rev. Fluid Mech.* **2014,** *46*, 121–146.

(7) Saint-Jalmes, A.; Durian, D. J. Vanishing Elasticity for Wet Foams: Equivalence with Emulsions and Role of Polydispersity. *J. Rheol.* **1999,** *43,* 1411–1422.

(8) Rouyer, F.; Cohen-Addad, S.; Hohler, R. Is the Yield Stress of Aqueous Foam a Well-defined Quantity? *Colloids Surf., A* **2005,** *263,* 111–116.

(9) Princen, H. M. Rheology of Foams and Highly Concentrated Emulsions. *J. Soc. Cosmet. Chem.* **1982,** *33,* 371–371.

(10) Khan, S. A.; Armstrong, R. C. Rheology of Foams: 1. Theory for Fry Foams. *J. Non-Newtonian Fluid Mech.* **1986,** *22,* 1–22.

(11) Tammaro, D.; D'Avino, G.; Di Maio, E.; Pasquino, R.; Villone, M. M.; Gonzales, D.; Groombridge, M.; Grizzuti, N.; Maffettone, P. L. Validated Modeling of Bubble Growth, Impingement and Retraction to Predict Cell-opening in Thermoplastic Foaming. *Chem. Eng. J.* **2016,** *287,* 492–502.

(12) Denkov, N. D.; Tcholakova, S.; Golemanov, K.; Ananthapadmanabhan, K. P.; Lips, A. Viscous Friction in Foams and Concentrated Emulsions under Steady Shear. *Phys. Rev. Lett.* **2008,** *100,* 138301.

(13) Hyun, K.; Kim, S. H.; Ahn, K. H.; Lee, S. J. Large Amplitude Oscillatory Shear as a Way to Classify the Complex Fluids. *J. Non-Newtonian Fluid Mech.* **2002,** *107,* 51–65.

(14) Sugimoto, M.; Suzuki, Y.; Hyun, K.; Ahn, K. H.; Ushioda, T.; Nishioka, A.; Taniguchi, T.; Koyama, K. Melt Rheology of Long-chain Branched Polypropylenes. *Rheol. Acta* **2006,** *46,* 33–44.

(15) Ewoldt, R. H.; Clasen, C.; Hosoi, A. E.; McKinley, G. H. Rheological Fingerprinting of Gastropod Pedal Mucus and Synthetic Complex Fluids for Biomimicking Adhesive Locomotion. *Soft Matter* **2007,** *3,* 634–643.

(16) Wilhelm, M. Fourier-transform Rheology. *Macromol. Mater. Eng.* **2002,** *287,* 83–105.

(17) Wilhelm, M.; Maring, D.; Spiess, H. W. Fourier-transform Rheology. *Rheol. Acta* **1998,** *37,* 399–405.

(18) Hoyle, D. M.; Auhl, D.; Harlen, O. G.; Barroso, V. C.; Wilhelm, M.; McLeish, T. C. B. Large Amplitude Oscillatory Shear and Fourier Transform Rheology Analysis of Branched Polymer Melts. *J. Rheol.* **2014,** *58,* 969–997.

(19) Rouyer, F.; Cohen-Addad, S.; Hoehler, R.; Sollich, P.; Fielding, S. M. The Large Amplitude Oscillatory Strain Response of Aqueous Foam: Strain Localization and Full Stress Fourier Spectrum. *Eur. Phys. J. E* **2008,** *27,* 309–321.

(20) Hyun, K.; Wilhelm, M.; Klein, C. O.; Cho, K. S.; Nam, J. G.; Ahn, K. H.; Lee, S. J.; Ewoldt, R. H.; McKinley, G. H. A Review of Nonlinear Oscillatory Shear Tests: Analysis and Application of Large Amplitude Oscillatory Shear (LAOS). *Prog. Polym. Sci.* **2011,** *36,* 1697–1753.

(21) Ewoldt, R. H.; Hosoi, A. E.; McKinley, G. H. New Measures for Characterizing Nonlinear Viscoelasticity in Large Amplitude Oscillatory Shear. *J. Rheol.* **2008,** *52,* 1427–1458.

(22) Khandavalli, S.; Rothstein, J. P. Large Amplitude Oscillatory Shear Rheology of Three Different Shear-thickening Particle Dispersions. *Rheol. Acta* **2015,** *54,* 601–618.

(23) Ptaszek, P. A Geometrical Interpretation of Large Amplitude Oscillatory Shear (LAOS) in Application to Fresh Food Foams. *J. Food Eng.* **2015,** *146,* 53–61.

(24) Gurnon, A. K.; Wagner, N. J. Large Amplitude Oscillatory Shear (LAOS) Measurements to Obtain Constitutive Equation Model Parameters: Giesekus Model of Banding and Nonbanding Wormlike Micelles. *J. Rheol.* **2012,** *56,* 333–351.

(25) Khair, A. S. Large Amplitude Oscillatory Shear of the Giesekus Model. *J. Rheol.* **2016,** *60,* 257–266.

(26) Rogers, S. A.; Lettinga, M. P. A Sequence of Physical Processes Determined and Quantified in Large Amplitude Oscillatory Shear (LAOS): Application to Theoretical Nonlinear Models. *J. Rheol.* **2012,** *56,* 1–25.

(27) Jacob, A. R.; Deshpande, A. P.; Bouteiller, L. Large Amplitude Oscillatory Shear of Supramolecular Materials. *J. Non-Newtonian Fluid Mech.* **2014,** *206,* 40–56.

(28) Phan-Thien, N.; Newberry, M.; Tanner, R. I. Non-linear Oscillatory Flow of a Soft Solid-like Viscoelastic Material. *J. Non-Newtonian Fluid Mech.* **2000,** *92,* 67–80.

(29) Wapperom, P.; Leygue, A.; Keunings, R. Numerical Simulation of Large Amplitude Oscillatory Shear of a High-density Polyethylene Melt using the MSF Model. *J. Non-Newtonian Fluid Mech.* **2005,** *130,* 63–76.

(30) D'Avino, G.; Greco, F.; Hulsen, M. A.; Maffettone, P. L. Rheology of Viscoelastic Suspensions of Spheres under Small and Large Amplitude Oscillatory Shear by Numerical Simulations. *J. Rheol.* **2013,** *57,* 813–839.

(31) Giesekus, H. A Simple Contitutive Equation for Polymer Fluids based on the Concept of Deformation-Dependent Tensorial Mobility. *J. Non-Newtonian Fluid Mech.* **1982,** *11,* 69–109.

(32) Calin, A.; Wilhelm, M.; Balan, C. Determination of the Non-linear Parameter (Mobility Factor) of the Giesekus Constitutive Model using LAOS Procedure. *J. Non-Newtonian Fluid Mech.* **2010,** *165,* 1564–1577.

(33) Thompson, R. L.; Alicke, A. A.; de Souza Mendes, P. R. Model-based Material Functions for SAOS and LAOS Analyses. *J. Non-Newtonian Fluid Mech.* **2015,** *215,* 19–30.

(34) Rogers, S. A.; Erwin, B. M.; Vlassopoulos, D.; Cloitre, M. A Sequence of Physical Processes Determined and Quantified in LAOS: Application to a Yield Stress Fluid. *J. Rheol.* **2011a,** *55,* 435–458.

(35) Kim, J.; Merger, D.; Wilhelm, M.; Helgeson, M. Microstructure and Nonlinear Signatures of Yielding in a Heterogenous Colloidal Gel under Large Amplitude Oscillatory Shear. *J. Rheol.* **2014,** *58,* 1359–1390.

(36) Rogers, S. A. In Search of Physical Meaning: Defining Transient Parameters for Nonlinear Viscoelasticity. *Rheol. Acta* **2017,** *56,* 501–525.

(37) Stickel, J. J.; Knutsen, J. S.; Liberatore, M. W. Response of Elastoviscoplastic Materials to Large Amplitude Oscillatory Shear Flow in the Parallel-Plate and Cylindrical-Couette Geometries. *J. Rheol.* **2013,** *57,* 1569–1596.

(38) Radhakrishnan, R.; Fielding, S. M. Shear Banding in Large Amplitude Oscillatory Shear (LAOStrain and LAOStress) of Soft Glassy Materials. *arXiv preprint arXiv:1704.08332* **2017**.

(39) Blanco, E.; Lam, S.; Smoukov, S. K.; Velikov, K. P.; Khan, S. A.; Velev, O. D. Stability and Viscoelasticity of Magneto-pickering Foams. *Langmuir* **2013,** *29,* 10019–10027.

(40) Vishal, B.; Ghosh, P. Foaming in Aqueous Solutions of Hexadecyltrimethylammonium Bromide and Silica Nanoparticles: Measurement and

Analysis of Rheological and Interfacial Properties. *J. Dispersion Sci. Technol.* **2018,** *39*, 62–70.

(41) Marze, S.; Guillermic, R. M.; Saint-Jalmes, A. Oscillatory Rheology of Aqueous Foams: Surfactant, Liquid Fraction, Experimental Protocol and Aging Effects. *Soft Matter* **2009,** *5*, 1937–1946.

(42) Macosko, C. W. *Rheology: Principles, Measurements, and Applications*; Wiley-VCH: New York, 1994.

(43) Cho, K. S.; Hyun, K.; Ahn, K. H.; Lee, S. J. A Geometrical Interpretation of Large Amplitude Oscillatory Shear Response. *J. Rheol.* **2005,** *49*, 747–758.

(44) Yu, W.; Wang, P.; Zhou, C. General Stress Decomposition in Nonlinear Oscillatory Shear Flow. *J. Rheol.* **2009,** *53*, 215–238.

(45) Bird, R. B.; Armstrong, R. C.; Hassager, O. *Dynamics of Polymeric Liquids (Volume 1) Fluid Mechanics*; Wiley: New York, 1987.

(46) Poulos, A. S.; Stellbrink, J.; Petekidis, G. Flow of Concentrated Solutions of Starlike Micelles under Large Amplitude Oscillatory Shear. *Rheol. Acta* **2013,** *52*, 785–800.

(47) Mason, J. C.; Handscomb, D. C. *Chebyshev Polynomials*; Chapman and Hall/CRC: USA, 2002.

(48) Renou, F.; Stellbrink, J.; Petekidis, G. Yielding Processes in a Colloidal Glass of Soft Star-like Micelles under Large Amplitude Oscillatory Shear (LAOS). *J. Rheol.* **2010,** *54*, 1219–1242.

(49) Moller, P.; Fall, A.; Chikkadi, V.; Derks, D.; Bonn, D. An Attempt to Categorize Yield Stress Fluid Behaviour. *Philos. Trans. R. Soc., A* **2009,** *367*, 5139–5155.

(50) Erni, P.; Parker, A. Nonlinear Viscoelasticity and Shear Localization at Complex Fluid Interfaces. *Langmuir* **2012,** *28*, 7757–7767.

(51) Lopez-Barron, C. R.; Wagner, N. J.; Porcar, L. Layering, Melting, and Recrystallization of a Close-packed Micellar Crystal under Steady and Large Amplitude Oscillatory Shear Flows. *J. Rheol.* **2015,** *59*, 793–820.

(52) Papon, A.; Montes, H.; Lequeux, F.; Guy, L. Nonlinear Rheology of Model Filled Elastomers. *J. Polym. Sci., Part B: Polym. Phys.* **2010,** *48*, 2490–2496.

(53) Mermet-Guyennet, M. R. B.; de Castro, J. G.; Habibi, M.; Martzel, N.; Denn, M. M.; Bonn, D. LAOS: The Strain Softening/Strain Hardening Paradox. *J. Rheol.* **2015,** *59,* 21–32.

(54) Rogers, S. A.; Erwin, B. M.; Vlassopoulos, D.; Cloitre, M. Oscillatory Yielding of a Colloidal Star Glass. *J. Rheol.* **2011b,** *55,* 733–752.

(55) van der Vaart, K.; Rahmani, Y.; Zargar, R.; Hu, Z.; Bonn, D.; Schall, P. Rheology of Concentrated Soft and Hard-sphere Suspensions. *J. Rheol.* **2013,** *57,* 1195–1209.

(56) Fraggedakis, D.; Dimakopoulos, Y.; Tsamopoulos, J. Yielding the Yield-stress Analysis: A Study Focused on the Effects of Elasticity on the Settling of a Single Spherical Particle in Simple Yield-stress Fluids. *Soft Matter* **2016,** *12,* 5378–5401.

(57) Dimitriou, C. J.; McKinley, G. H. A Comprehensive Constitutive Law for Waxy Crude Oil: A Thixotropic Yield Stress Fluid. *Soft Matter* **2014,** *10,* 6619–6644.

(58) Dimitriou, C. J.; Ewoldt, R. H.; McKinley, G. H. Describing and Prescribing the Constitutive Response of Yield Stress Fluids using Large Amplitude Oscillatory Shear Stress (LAOStress). *J. Rheol.* **2013,** *57,* 27–70.

(59) Hyun, K.; Wilhelm, M. Establishing a New Mechanical Nonlinear Coefficient Q from FT-rheology: First Investigation of Entangled Linear and Comb Polymer Model Systems. *Macromolecules* **2009,** *42,* 411–422.

(60) Wagner, M. H.; Rolon-Garrido, V. H.; Hyun, K.; Wilhelm, M. Analysis of Medium Amplitude Oscillatory Shear Data of Entangled Linear and Model Comb Polymers. *J. Rheol.* **2011,** *55,* 495–516.

(61) Wilhelm, M.; Reinheimer, K.; Kubel, J. Optimizing the Sensitivity of FT-rheology to Quantify and Differentiate for the First Time the Nonlinear Mechanical Response of Dispersed Beer Foams of Light and Dark Beer. *Z. Phys. Chem.* **2012,** *226,* 547–567.

Chapter 6

Summary and Scope for Future Work

6.1 Summary of the work

An experimental study has been performed on aqueous foams stabilized by a mixture of HTAB and silica nanoparticles. Their concentrations were varied to understand the foaming behavior of these aqueous solutions. The effects of HTAB in the presence of silica nanoparticles were investigated in Chapter 3. The effects of silica nanoparticles in the presence of HTAB were investigated in Chapter 4. In Chapter 5, a systematic study of the LAOS behavior of foam stabilized by 0.1 mol m^{-3} HTAB and 0.5 wt.% silica nanoparticles was studied. The salient accomplishments and the major conclusions are as follows:

- At low HTAB concentration (i.e. below the CMC), foams were more stable, and they were composed of spherical bubbles. They possessed high viscosity and viscoelasticity. The air–water interfaces were covered with a Langmuir-type monolayer. This was due to the presence of the surfactant-laden particles. Therefore, these interfaces showed high surface pressure during the compression of the monolayer.
- In the HTAB solutions containing silica nanoparticles, the adsorption of HTAB molecules occurred on the surface of the latter. This was due to the electrostatic attraction between the HTAB and the silica nanoparticles. As a result, the hydrophilicity of the particles decreased, and the charge at the surface of the particles became less negative. This enabled the silica nanoparticles to adsorb at the air–water interfaces. The particles adsorbed at the interfaces prevented coalescence.
- The nanoparticles having diameter less than 10 nm adsorbed at the air–water interfaces. Since the silica nanoparticles were hydrophilic, a major portion of these particles was oriented towards the aqueous phase, and hence a lesser portion was in the air. The larger

particles could not move to the interface, and hence they remained in the Plateau borders and nodes of the foam films, which reduced the film drainage.

- Foamability and foam stability increased with increasing particle concentration. An increase in particle concentration caused a closer packing of the nanoparticles at the air–water interfaces as well as in the foam films.
- At high HTAB concentration (i.e. above the CMC), the surface was completely occupied by the HTAB molecules and hence, the surfactant-laden particles were accommodated near the sub-phase or in the bulk phase. Due to the absence of particles, the interface was covered with a Gibbs-type monolayer. Therefore, it did not exhibit a significant surface pressure and viscoelasticity. Consequently, the foams formed by these solutions were relatively less stable. The bubbles was usually polyhedral.
- The LAOS study of foam revealed a sequence of physical processes in an intracycle oscillatory shear flow. The foam exhibited elastic straining at the strain reversion point and showed yielding behavior above the critical strain, which was followed by strain-hardening. Shear-thickening was also observed at moderate deformations.

The fundamental understanding reported in this thesis will enable the development of a novel range of products based on particle-stabilized foams for use in foods, detergents, and cosmetic formulations.

6.2 Future scope of research

Based on the work conducted in this thesis, research can be extended in many different ways in the future. Some of the interesting ideas are as follows:

- In this thesis, the foams were formed by mixing the aqueous dispersions containing surfactant and nanoparticles in a blender. This gives polydisperse foams. The polydispersity (or morphology) strongly influences the foaming behavior. A monodisperse foam can be prepared by injecting air slowly into the aqueous phase through an orifice or a sparger. The morphology of the foam can be controlled by controlling the air-flow rate. Therefore, the characteristics of monodisperse foams may be studied and compared with the polydisperse foams. The influence of experimental conditions, such as air-flow rate, temperature, pH, ionic strength, and age on the foamability and foam stability may be studied.
- Therefore, it is suggested to compare the foaming behavior of monodisperse and polydisperse foams. Also, to observe the influence of experimental conditions (i.e. air-flow rate, temperature, pH, ionic strength, age, etc.) on the foamability and foam stability.
- The work reported in Chapter 4 describes the effect of nanoparticles on the foaming behavior of surfactant solutions. Most of the studies on particle-stabilized foams are based on inorganic nanoparticles, such as silica nanoparticles. These nanoparticles may not be used when the end-use of foam is in food and biomedical applications. Therefore, to stabilize such foams, particles of biological origin, i.e. cellulose, lignin, chitin, starch, protein (e.g. soy, zein, and ferritin) may be used. These particles are usually non-spherical. Therefore, the study of the physicochemical properties of the particles (i.e. size, shape, and hydrophilicity) is also relevant.
- The work reported in Chapter 5 explains the LAOS behavior of foam. The LAOS experiments are rheologically more complex than the small amplitude oscillatory shear experiments. The information obtained from the LAOS study does not reveal the physical

interpretation of the foam. Therefore, the theoretical understanding of the nonlinear responses observed under the LAOS flow is sometimes not clearly. To overcome this problem, the use of microstructural investigation, such as rheo-SAXS and rheo-dielectric combination may help to understand the microstructural origin of nonlinear viscoelastic behavior of foam. Furthermore, this approach can be extended to the air–water interface.

- A change in the pH of the aqueous dispersions can alter the surface charge of the silica nanoparticles. Moreover, addition of salt my change the surface properties of these particles. Therefore, it is believed that the modulation of pH and salt concentration can enable the particles to move to the interface and cause a closer packing, which may improve the stability of the foams.

6.3 Publications and conferences

Refereed journals:

1. **Vishal, B.** and Ghosh, P. Foaming in Aqueous Solutions of Hexadecyltrimethylammonium Bromide and Silica Nanoparticles: Measurement and Analysis of Rheological and Interfacial Properties. *J. Dispersion Sci. Technol.* **2018**, *39*, 62–70.
2. **Vishal, B.** and Ghosh, P. Nonlinear Viscoelastic Behavior of Aqueous Foam under Large Amplitude Oscillatory Shear Flow. *Korea-Aust. Rheol. J.* **2018** (*Accepted for publication, April 2018*).
3. **Vishal, B.** and Ghosh, P. The Effect of Silica Nanoparticles on the Stability of Aqueous Foams. *J. Dispersion Sci. Technol.* **2018** (*Accepted for publication, April 2018*).

Conferences:

- **Vishal, B.** and Ghosh, P. Interfacial Rheology of Particle–Surfactant System at Liquid Interfaces. Compflu-2016, Hyderabad (India). 12–14 December, 2016 (*Poster presented*).
- **Vishal, B.** and Ghosh, P. Effect of Particle at Air–Water Interface in the Presence of Surfactant. 7th Conference on Colloid and Interface Science, Kuala Lumpur (Malaysia). 8–11 August, 2017 (*Oral presented*).
- **Vishal, B.** and Ghosh, P. Surface Forces in a Thin Liquid Film. Research Conclave'18, Guwahati (India). 8–11 March, 2018 (*Poster presented*).

Annexure A

In the rheometer, the strain and stress were obtained by a linear mapping of the deformation and torque, respectively. The linear mapping was considerable when the experiment was carried out in the linear viscoelastic regime. However, in the nonlinear viscoelastic regime, a heterogeneous flow field developed between the parallel plates. Stickel et al.[1] showed by numerical simulation that the linear mapping of the deformation and torque resulted into strain and stress signals that deviated significantly from their uniform-shear counterparts.

In the present work, all the experiments on foam rheology were performed by using the parallel-plate geometry (roughened by sand blasting). This geometry was chosen because the gap between the plates could be adjusted easily according to the foam structure. However, the flow field generated during the shear was heterogeneous, which was significant under the LAOS flow. Giacomin et al.[2] derived a mathematical expression of shear stress for the cone-and-plate geometry, where homogeneous flow field could be achieved. The derivation was performed by using a simple continuum model relevant to the LAOS flow,[3,4] given by

$$\sigma = \sigma_1 + \sigma_3 + \sigma_5 + \cdots . \tag{A.1}$$

where the total stress is the sum of the stress components of the odd harmonic terms, which are given by [2]

$$\sigma_1 = \frac{\eta_0}{\lambda}\left[\begin{array}{l} -(\lambda\gamma_0\omega)\dfrac{\cos(\omega t)+\lambda\omega\sin(\omega t)}{1+\lambda^2\omega^2}+\dfrac{(\lambda\gamma_0\omega)^3}{4}\left[\dfrac{3\cos(\omega t)+6\lambda\omega\sin(\omega t)}{(1+\lambda^2\omega^2)(1+4\lambda^2\omega^2)}\right] \\ -\dfrac{(\lambda\gamma_0\omega)^5}{8}\left[\dfrac{5\cos(\omega t)+15\lambda\omega\sin(\omega t)}{(1+\lambda^2\omega^2)(1+4\lambda^2\omega^2)(1+9\lambda^2\omega^2)}\right] \end{array}\right] \quad \text{(A.2)}$$

$$\sigma_3 = \frac{\eta_0}{\lambda}\left[\begin{array}{l} \dfrac{(\lambda\gamma_0\omega)^3}{4}\left[\dfrac{(1-11\lambda^2\omega^2)\cos(3\omega t)+6(1-\lambda^2\omega^2)\lambda\omega\sin(3\omega t)}{(1+\lambda^2\omega^2)(1+4\lambda^2\omega^2)(1+9\lambda^2\omega^2)}\right] \\ -\dfrac{(\lambda\gamma_0\omega)^5}{8}\left[\dfrac{(5-130\lambda^2\omega^2)\cos(3\omega t)+(45-120\lambda^2\omega^2)\lambda\omega\sin(3\omega t)}{2(1+\lambda^2\omega^2)(1+4\lambda^2\omega^2)(1+9\lambda^2\omega^2)(1+16\lambda^2\omega^2)}\right] \end{array}\right] \quad \text{(A.3)}$$

$$\sigma_5 = \frac{\eta_0}{\lambda}\left[-\frac{(\lambda\gamma_0\omega)^5}{8}\left\{\frac{(1-85\lambda^2\omega^2+274\lambda^4\omega^4)\cos(5\omega t)+(15-225\lambda^2\omega^2+120\lambda^4\omega^4)\lambda\omega\sin(5\omega t)}{2(1+\lambda^2\omega^2)(1+4\lambda^2\omega^2)(1+9\lambda^2\omega^2)(1+16\lambda^2\omega^2)(1+25\lambda^2\omega^2)}\right\}\right] \quad \text{(A.4)}$$

The elastic and viscous Lissajous–Bowditch curves were plotted by using Equation A.1, as shown in Figure A.1. These plots are similar to those obtained from the parallel-plate geometry. Therefore, we can conclude that the heterogeneous flow during the LAOS experiments was negligible.

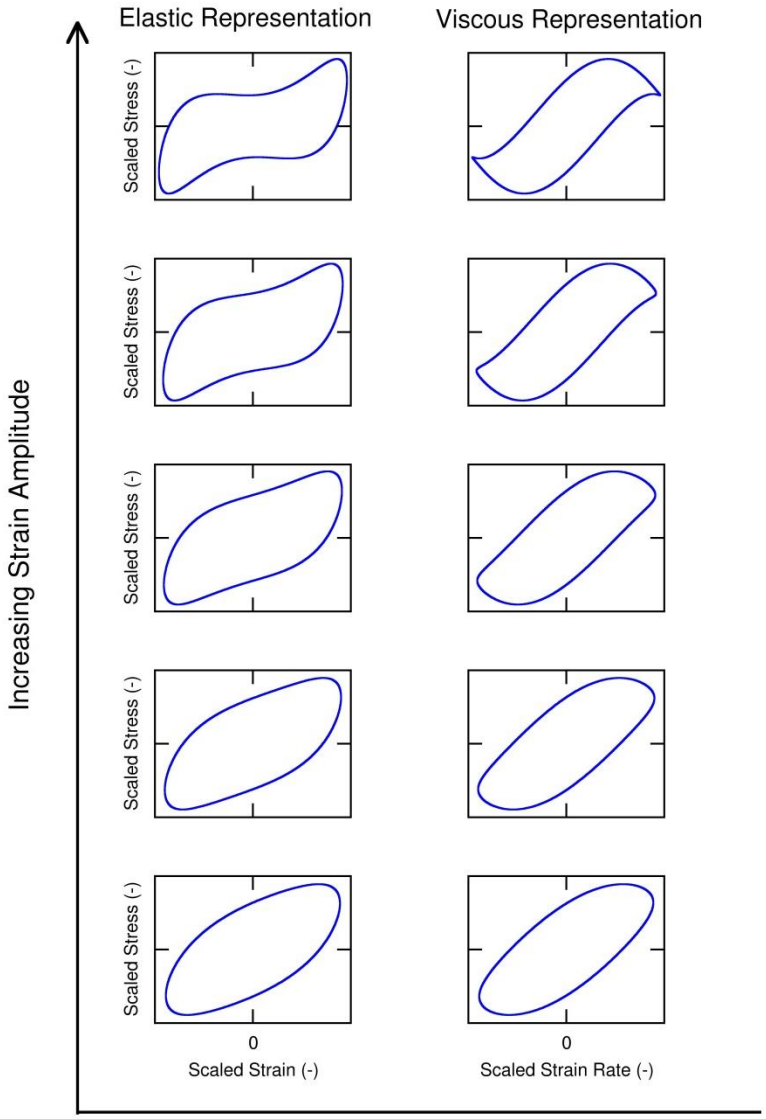

Figure A.1 Lissajous–Bowditch curves obtained from Equation A.1.

Annexure B

Curve fitting of stress waveforms by Fourier series (Equation 5.6) (see Figure 5.9).

```
close all; clc
t = 0:1/257:1-1/257;
y = xlsread('LAOS_data.xlsx', '0.1mM_1rads', 'BB4:BB260')';      % Shear stress at 100%
strain                                                            % and 1 rad/s
angular frequency.
plot(t,y)
hold on
T = 1;
n = 3;                                                % n is Number of harmonic terms
a0 = (1/T)*trapz(t,y);
 for i = 1:n
  a(i) = (2/T)*trapz(t,y.*cos(2*pi*i*t));             % Computation of aₙ from Equation
5.7
  b(i) = (2/T)*trapz(t,y.*sin(2*pi*i*t));             % Computation of bₙ from Equation
5.7
 end
x = 0;
 for p = 1:2:n
  xx = a(p)*cos(2*pi*p*t) + b(p)*sin(2*pi*p*t);
  x = x + xx;
 end
plot(t,x,'--r')
set(gca,'fontsize', 15);
text(0.5,3,'a_1 = 3.7784','FontSize', 10)
text(0.5,2,'b_1 = 2.7421','FontSize', 10)
text(0.5,1,'a_3 = -0.5504','FontSize', 10)
text(0.5,0.1,'b_3 = -0.9008','FontSize', 10)
xlabel('Time (-)')
ylabel('Shear Stress (Pa)')
legend('Strain = 100%')
print('1strain','-dpng','-r80')
```

Code written with MATLAB® R2014b

Annexure C

Computation of discrete Fourier transform of the stress data by using Equation 5.10 (see the first column of Figure 5.9).

```
clear all; clc
x = xlsread('waveform.xlsx', 'Sheet2', 'W2:W258')';      % Shear stress at 100% strain
and                                                                              %
1 rad/s angular frequency.
N = length(x);
 for k = 0:N-1
  for n = 0:N-1
   X(n+1) = x(n+1)*exp(-j*2*pi*k*n/N);                   % Equation 5.10
  end
   Xk(k+1) = sum(X);
 end
Xk;
mag = abs(Xk);
stem(0:N-1,mag);
xlim([-0.1 11]);
ylim([-0.003 700]);
legend('Strain = 100%')
xlabel('Harmonic')
ylabel('Magnitude')
set(gca, 'XTick', [0 1.0 3 5 7 9 11 13 15])
set(gca,'fontsize', 15);
axes('Position',[.4 .4 .45 .35])
box on
stem(0:N-1,mag)
xlim([-0.1 11]);
ylim([-0.5 100]);
xlabel('Harmonic')
ylabel('Magnitude')
set(gca, 'XTick', [0 1.0 3 5 7 9 11 13 15])
set(gca,'fontsize', 10);
print('1strain','-dpng','-r40')
```

Code written with MATLAB® R2014b

References

(1) Stickel, J. J.; Knutsen, J. S.; Liberatore, M. W. Response of Elastoviscoplastic Materials to Large Amplitude Oscillatory Shear Flow in the Parallel-plate and Cylindrical-Couette Geometries. *J. Rheol.* **2013,** *57*, 1569–1596.

(2) Giacomin, A. J.; Gilbert, P. H.; Merger, D.; Wilhelm, M. Large Amplitude Oscillatory Shear: Comparing Parallel-disk with Cone-Plate Flow. *Rheol. Acta* **2015,** *54*, 263–285.

(3) Wagner, M. H.; Rolon-Garrido, V. H.; Hyun, K.; Wilhelm, M. Analysis of Medium Amplitude Oscillatory Shear Data of Entangled Linear and Model Comb Polymers. *J. Rheol.* **2011,** *55*, 495–516.

(4) Giacomin, A. J.; Bird, R. B.; Johnson, L. M.; Mix, A. W. Large Amplitude Oscillatory Shear Flow from the Corotational Maxwell Model. *J. Non-Newtonian Fluid Mech.* **2011,** *166*, 1081–1099.